

ABSTRACT

Title of Document: INVESTIGATIONS OF TWO-DIMENSIONAL MATERIALS FOR NEXT-GENERATION ELECTRONIC DEVICES

Jaron A. Kropp, Doctor of Philosophy, 2020

Directed By: Dr. Theodosia Gougousi
Professor
Department of Physics

Dr. Can Ataca
Assistant Professor
Department of Physics

Semiconducting transition metal dichalcogenides (TMDs) such as MoS_2 exhibit a direct band gap when isolated in monolayer form. They also exhibit high carrier mobility and are therefore attractive for use as channel materials in metal-oxide semiconductor field-effect transistors (MOSFETs) and other devices. MOSFETs rely on the integration of a metal-oxide dielectric layer with the semiconducting channel material. Atomic layer deposition (ALD) is often used for the deposition of dielectrics, but the MoS_2 surface is hydrophobic and lacks dangling bonds. Because of this, ALD films on MoS_2 are often poor quality, containing many gaps or pinholes.

This work studies the effects of MoS_2 surface preparation on ALD film quality. ALD films of TiO_2 and Al_2O_3 are deposited on both mechanically exfoliated and chemical vapor deposition (CVD) grown MoS_2 . It is found that mechanically exfoliated MoS_2 samples exhibit a wide range of film surface coverage as a result of variations in surface defect concentration and contamination from the exfoliation process. CVD-

grown MoS₂ offers more reliable starting surfaces. Therefore, CVD-grown MoS₂ was chosen to study surface engineering and functionalization for ALD.

Reactive sulfur vacancies were formed in the MoS₂ surface via argon ion sputtering, and thiol molecules were introduced to passivate the vacancies and leave the surface amenable to ALD. Films grown on thiol-treated surfaces and vacancy-containing surfaces were continuous and morphologically similar. DFT calculations showed that the thiol molecules attach primarily to sulfur vacancies. The ALD precursor molecule also binds strongly to the sulfur vacancies, thus leading to uniform film growth on vacancy-containing surfaces.

The remainder of this work focuses on the discovery of novel electronic materials using DFT. The electronic and magnetic properties of Janus TMD nanoribbons were studied. Janus TMDs are created by replacing one side of chalcogen atoms (e.g. S) of a TMD monolayer with another (e.g. Se). Nanoribbons of Mo- and W-based Janus TMDs were studied in zigzag and armchair configurations. Zigzag nanoribbons are found to be magnetic metals, while armchair nanoribbons are semiconductors. The magnetic and electronic properties of these nanoribbons can be modulated by controlling the ribbon width and the saturation of edge atoms.

Further studies investigate the surface functionalization of two-dimensional tellurene (Te). DFT is used to investigate the electronic structure of α - and β -Te sheets functionalized with hydrogen, oxygen, or fluorine. When functionalized, α - and β -Te become metallic, except for hydrogenated β -Te which remains semiconducting. Fluorinated Te structures are unstable, but H and O functionalized structures may be suitable for use in nanoscale electronics.

INVESTIGATIONS OF TWO-DIMENSIONAL MATERIALS FOR NEXT-
GENERATION ELECTRONIC DEVICES

By

Jaron A. Kropp

Dissertation submitted to the Faculty of the Graduate School of the
University of Maryland, Baltimore County, in partial fulfillment
of the requirements for the degree of
Doctor of Philosophy
2020

© Copyright by
Jaron A. Kropp
2020

Dedicated to my grandfather

Abel M. Dominguez

Acknowledgements

There are many people to whom I owe thanks for their part in the successful completion of this dissertation. Without their varied and important contributions, I could not have finished this work. First and foremost, I would like to thank my advisor, Dr. Gougousi. She has helped me with all aspects of the scientific research progress and has assisted me in innumerable ways. I am grateful for her guidance both in and out of the lab, but I am most grateful for her ability to always see the best in my work and steer me back to the correct path when I was struggling to make sense of the data. Without her unfailing positivity in this regard, I certainly could not have completed this work. Furthermore, her willingness to allow me to pursue research interests in other areas allowed me to gain the computational skills needed to complete the final chapters of this dissertation.

I am also grateful to my co-advisor, Dr. Ataca, for taking me on board when I was already in my fourth year of graduate school. He allowed me to join his computational group and learn the ropes of density functional theory while also fulfilling commitments to Dr. Gougousi's lab. I am appreciative of his openness and willingness to discuss research at any time, and of his good humor that is ever-present. I would also like to express my gratitude for my committee members, Dr. Hayden, Dr. Pelton, and Dr. Daniel. These relationships have resulted in several helpful discussions and even a few collaborative research efforts. I appreciate the time they have invested in assisting me with my research and in reading my dissertation. I must also extend special thanks to Dr. Takacs, who served on my preliminary PhD committee before his passing. In

addition to serving as a committee member, Dr. Takacs assisted me with operation of the SEM and AFM, and always provided good cheer and a hearty laugh.

Several aspects of this work could not have been completed without the assistance of Erik Crowe. Erik lent his expertise in many areas, including machining parts for the lab and assisting with the operation of the AFM and the clean room deposition tools. Furthermore, I am thankful to Erik for his friendship throughout my time at UMBC and for the many much-needed cups of coffee we've shared. I am grateful as well to my cohort members Brian Carroll, Brent McBride, and Anin Puthukkudy for countless long lunches that provided endless entertainment. Our talks certainly helped keep the spirits up.

I'd like to thank Crista Barnes for her support and love through the last and most difficult year of my PhD. She never fails to lift my spirits and inspires me to face challenges with a clear and focused mind. I am so grateful to her for everything from her unwavering encouragement to our relaxing afternoons rock climbing or playing board games. She constantly inspires me to be a better person.

Finally, I would like to thank my parents for their continued support throughout my life. They have always allowed me the time and space to pursue my dreams and goals. Though we live far apart, my mother is always a phone call away and ready to lend an ear and some good life advice. My father forever served as my inspiration to complete my PhD, and to take better photographs! With their lifelong guidance, all of this has been possible.

Table of Contents

Acknowledgements.....	iii
Table of Contents.....	v
List of Tables.....	vii
List of Figures.....	viii
Chapter 1. Introduction.....	1
1.1. Overview of Dissertation.....	1
Chapter 2. Background Information.....	5
2.1. Metal-Oxide Semiconductor Field-Effect Transistors.....	5
2.2. Transition Metal Dichalcogenides.....	7
2.3. Atomic Layer Deposition.....	9
2.4. Motivation.....	12
Chapter 3. Experimental Methods.....	14
3.1. ALD Reactor.....	14
3.2. Sample Preparation.....	15
3.2.1. Mechanical Exfoliation.....	15
3.3. Characterization Techniques.....	16
3.3.1. Atomic Force Microscopy.....	16
3.3.2. X-ray Photoelectron Spectroscopy.....	18
Chapter 4. Density Functional Theory.....	21
4.1. Hohenberg-Kohn Theorems.....	21
4.2. Kohn-Sham Equations.....	23
4.3. Exchange-Correlation Functionals.....	25
4.4. Computational Details.....	26
4.4.1. K-points.....	26
4.4.2. Energy Cutoff.....	27
4.4.3. Pseudopotentials.....	29
Chapter 5. Atomic Layer Deposition of Al ₂ O ₃ and TiO ₂ on MoS ₂ surfaces.....	32
5.1. Introduction.....	32
5.2. Experimental.....	33
5.3. Results.....	35
5.3.1. Surface Preparation.....	35
5.3.2. Atomic Layer Deposition of Al ₂ O ₃	38
5.3.3. Atomic Layer Deposition of TiO ₂	43
5.4. Discussion.....	45
5.4.1. Starting Surface Variability.....	45
5.4.2. Al ₂ O ₃ and TiO ₂ Films on CVD-grown MoS ₂	47
5.5. Conclusions.....	50
5.6. Supplemental Information.....	51
5.6.1. AFM images of Al ₂ O ₃ on silicon.....	51
5.6.2. Al ₂ O ₃ films on MoS ₂	51
Chapter 6. Surface Defect Engineering of MoS ₂ for Atomic Layer Deposition of TiO ₂ Films.....	53
6.1. Introduction.....	53
6.2. Experimental Methods.....	55
6.3. Computational Methods.....	57

6.4. Results.....	58
6.4.1. Atomic Layer Deposition of TiO ₂ on MoS ₂	58
6.4.2. First-Principles Calculations	62
6.5. Discussion	68
6.5.1. Possible Growth Mechanisms.....	69
6.5.2. Electronic Properties of Defective MoS ₂	72
6.6. Conclusions.....	73
Chapter 7. Spontaneous Curvature of Janus Transition Metal Dichalcogenide Nanoribbons	74
7.1. Introduction.....	74
7.2. Computational Details	76
7.3. Results and Discussion	76
7.3.1. Structural Properties.....	76
7.3.2. Electronic and Magnetic Properties	85
7.3.3. Hydrogen Passivation	90
7.4. Conclusions.....	94
Chapter 8. Electronic Properties of Bare and Functionalized Two-Dimensional Tellurene Structures	96
8.1. Introduction.....	96
8.2. Computational Details	100
8.3. Results and Discussion	101
8.3.1. Bare 2D Te.....	101
8.3.2. Functionalized 2D Te Structures	105
8.3.2.1. Modification of atomic structure upon functionalization	105
8.3.2.2. Stability analysis	109
8.3.2.3. Electronic Properties of Functionalized 2D Te.....	111
8.3.3. Single atom and molecule binding.....	114
8.4. Conclusions.....	118
Chapter 9. Conclusions	119
9.1. Atomic Layer Deposition of Al ₂ O ₃ and TiO ₂ on MoS ₂ surfaces	119
9.2. Surface Defect Engineering of MoS ₂ for Atomic Layer Deposition of TiO ₂ Films	119
9.3. Spontaneous Curvature of Janus Transition Metal Dichalcogenide Nanoribbons: Effects on Optoelectronic, Magnetic and Mechanical Properties ..	120
9.4. Electronic properties of bare and functionalized Two-Dimensional Tellurene structures	120
Appendices.....	122
Appendix A. Properties of Bare and Hydrogenated Janus Nanoribbons.....	122
References.....	126

List of Tables

Table 6.1. Calculated adsorption energies of mercaptoethanol on MoS ₂ in a 4×4×1 supercell for both pristine MoS ₂ and S-vacancy-containing MoS ₂	63
Table 7.1. Lattice properties and band gaps of Mo/W TMDs and Janus TMDs.	78
Table 8.1. The binding or dissociation energies ($E_{binding/diss}$) of single H, O and F atoms and single H ₂ , O ₂ , and F ₂ molecules on α and β -Te. The * indicates dissociation energy. Values of charge transferred to each adatom/molecule calculated from Bader charge analysis are also given.....	115
Table A-1. Properties of bare Janus TMD nanoribbons. Reported are the cohesive energy (E_{coh}), band gap (E_g), band gap character, magnetic moment (μ), magnetic character, curvature radius (r_{curve}), and curvature energy (E_{curve}).	122
Table A-2. Properties of hydrogen-passivated Janus TMD nanoribbons. Reported are the cohesive energy (E_{coh}), band gap (E_g), band gap character, magnetic moment (μ), magnetic character, curvature radius (r_{curve}), and curvature energy (E_{curve}).	124

List of Figures

- Figure 2.1.** A typical n-type MOSFET in operation. The source and drain are formed from n-type silicon in a p-type silicon substrate. When a positive voltage is applied to the gate, positive charges are driven away from the gate. A voltage is then applied across the source and drain, and electrons may flow from the source to the drain. Redrawn from Ref. [16]. 5
- Figure 2.2.** Predicted transistor gate length trend. The gate oxide thickness is directly related to the physical gate length. Reprinted from Ref. [17] – Published by The Royal Society of Chemistry. 6
- Figure 2.3.** Cartoon schematic of one ALD cycle, redrawn from Ref. [36]. 10
- Figure 2.4.** Schematic of the ligand-exchange mechanism for an ALD process using tetrakis (dimethylamino) titanium (TDMAT) and water. The starting surface is –OH terminated. In the first half cycle (a), TDMAT reacts with the –OH terminated surface, releasing methyl ligands. In the second half cycle (b), water reacts with the TDMAT on the surface, releasing the remaining ligands and leaving the surface –OH terminated once more. 11
- Figure 2.5.** Schematic of ALD growth rate as a function of temperature. The growth rate in (a) increases as a result of precursor condensation and decreases in (b) as a result of incomplete reactions. In (c), precursor decomposition drives up the growth rate, and in (d), precursor desorption lowers the growth rate. The ALD window is represented by (e) where the growth per cycle is relatively constant. 12
- Figure 3.1.** Diagram of the ALD reactor to be used for growth of metal oxides on MoS₂. Reprinted with permission from Ref. [47]. 14
- Figure 3.2.** Optical images of exfoliated MoS₂ flakes on 500 nm SiO₂ substrates. A single MoS₂ flake is shown in (a) and (b) at different magnifications. In (c), various thicknesses of MoS₂ flakes are shown (color is thickness-dependent). Scale bars are 50 μm for (a) and (c) and 10 μm for (b). 16
- Figure 3.3.** (a) Optical image of an exfoliated MoS₂ flake on 500 nm SiO₂. The black square marks the region scanned with AFM in (b). The step heights of selected regions are also shown in (b). The scale bars correspond to (a) 50 μm and (b) 5 μm. 16
- Figure 3.4.** Basic operation of an atomic force microscope. The cantilever deflection is measured by the laser's reflection on the photodiode and modulated by a piezoelectric crystal. 17
- Figure 3.5.** Schematic of an x-ray ejecting a core electron from an oxygen atom. The binding energy of an ejected electron is specific to the atom and orbital from which the electron originates. Reprinted with permission from Ref. [47]. 19
- Figure 4.1.** Total energy of MoS₂ as a function of k points. 27

Figure 4.2. Total energy of MoS ₂ as a function of cutoff energy.	29
Figure 4.3. (a) Comparison of the real potential, V , to the pseudopotential, V_{pseudo} , and (b) comparison of the real wave function to the pseudo-wave function. Above the cutoff radius r_c , the potentials and the wave functions match.	30
Figure 5.1. Characterization of CVD-grown MoS ₂ . (a) Optical micrograph of MoS ₂ flakes on 300 nm SiO ₂ substrate (scale bar 50 μm) and (b) Raman spectrum of the E _{2g} and A _{1g} modes of MoS ₂ . AFM images of a typical flake and its surface are shown in (c) (scale bar 2 μm) and (d) (scale bar 600 nm), respectively. The flake height was measured as ~ 0.7 nm in (c), and the RMS roughness from (d) was measured as 0.165 nm.	36
Figure 5.2. Optical micrographs of MoS ₂ exfoliated with scotch tape and annealed for 120 s on a 100°C hotplate (a-c). The as-exfoliated flake is shown in (a) and the images taken after acetone soaks of 4 hours and 8 hours are shown in (b) and (c), respectively. In (d), an AFM image of the flake after an 8 hour acetone soak is shown. Scale bars are 10 μm in (a-c) and 3 μm in (d).	37
Figure 5.3. AFM images of 1 nm Al ₂ O ₃ deposited at 100°C on dicing tape exfoliated MoS ₂ (a-c), Scotch tape exfoliated MoS ₂ (d-f), and CVD-grown MoS ₂ (g-i). The scale bar is 600 nm for all images. For each surface preparation, images are taken from different flakes on the same substrate. RMS roughness values are given in units of nm.	39
Figure 5.4. Calculated surface coverage for 1 and 3 nm Al ₂ O ₃ films grown at 100°C on Scotch tape exfoliated, dicing tape exfoliated, and CVD-grown MoS ₂ surfaces. Error bars are not included for clarity but the uncertainty for the surface coverage is estimated at $\sim 5\%$	41
Figure 5.5. AFM images of 3 nm Al ₂ O ₃ deposited on CVD-grown MoS ₂ at 100°C (a-c) and 200°C (d-f). Scale bars are 3 μm (a,d) and 600 nm (b,c,e,f). RMS roughness values are given in units of nm.	42
Figure 5.6. AFM images of 3 nm Al ₂ O ₃ films grown on CVD MoS ₂ at 100°C showing growth along defects (a) and multilayered step edges (b). Scale bars are 600 nm. RMS roughness values are given in units of nm.	42
Figure 5.7. AFM images of 3 nm TiO ₂ deposited on CVD-grown MoS ₂ at 100°C (a-c) and 200°C (d-f). Scale bars are 2 μm (a,d) and 600 nm (b,c,e,f). RMS roughness values are given in units of nm.	43
Figure 5.8. AFM images of 6 nm TiO ₂ deposited on CVD-grown MoS ₂ at 100°C (a-c) and 200°C (d-f). Scale bars are 2 μm (a,d) and 600 nm (b,c,e,f). RMS roughness values are given in units of nm.	44

Figure 5.9. Calculated surface coverage of 3 nm and 6 nm TiO ₂ deposited on CVD-grown MoS ₂ at 100°C and 200°C. Error bars are not included for clarity but the uncertainty for the surface coverage is estimated at ~5%.....	45
Figure 5.10. (a) 1 nm Al ₂ O ₃ on 300 nm SiO ₂ at 100°C. Also shown are 3 nm Al ₂ O ₃ at (b) 100°C and (c) 200°C on native oxide Si. TiO ₂ at 100°C shown for thicknesses of (d) 3 nm and (e) 6 nm at 100°C on native oxide Si. Scale bars are 600 nm.	51
Figure 5.11. Surface coverage of Al ₂ O ₃ on CVD-grown MoS ₂ at 200°C.	52
Figure 5.12. (a), (b) AFM scans of 1 nm Al ₂ O ₃ deposited on CVD-grown MoS ₂ at 200°C.	52
Figure 6.1. AFM images of ALD of 6 nm TiO ₂ on (a,b) untreated MoS ₂ and (c,d) MoS ₂ treated with mercaptoethanol. Blue bars mark the location of line profiles shown below each image.	59
Figure 6.2. The left axis (red line) plots the sulfur:molybdenum ratio of MoS ₂ as a function of sputter time (ion fluence) as calculated from XPS peak fitting. The right axis (blue line) plots the calculated sulfur vacancy percentage as a function of sputter time (ion fluence).	60
Figure 6.3. X-ray photoelectron spectra of the (a) Mo 3d region (no sputtering) and (b) S 2p region (no sputtering), and the (c) Mo 3d region (390s sputtering) and (d) S 2p region (390s sputtering).	61
Figure 6.4. AFM images of 6 nm TiO ₂ deposited on ME-treated MoS ₂ that was sputtered for (a) 60 s, (b), 240 s, and (c) 390 s. Also shown are AFM images of 6 nm TiO ₂ deposited on MoS ₂ that was sputtered for (d) 60 s, (e) 240 s, and (f) 390 s with no ME treatment. Blue bars mark the location of line profiles shown below each image.	62
Figure 6.5. (a) The adsorption sites studied for mercaptoethanol. (b) The relaxed geometric structure of the ME molecule adsorbed above the S vacancy. (c) The relaxed geometric structure of the ME molecule adsorbed in the S vacancy. The atoms are: Mo (purple), S (yellow), O (red), C (brown), and H (white).	63
Figure 6.6. Adsorption geometry and energy of O ₂ , H ₂ O, and TDMAT on a single S vacancy. The atoms shown in the figure are: Mo (purple), S (yellow), O (red), C (brown), H (white), N (pale blue), and Ti (bright blue).	64
Figure 6.7. Energy barrier calculations of the ME molecule in a sulfur double vacancy. The inset shows the barrier measured at ~0.09 eV. The atoms shown in the figure are: Mo (purple), S (yellow), O (red), C (brown), and H (white).	66
Figure 6.8. Density of states of (a) pristine MoS ₂ , (b) MoS ₂ with a single S vacancy, (c) MoS ₂ with a double S vacancy, and (d) MoS ₂ with a line vacancy. Also shown are	

(e) ME on pristine MoS ₂ , (f) ME in a single S vacancy, (g) ME in a double S vacancy, and (h), ME in a line vacancy.	67
Figure 6.9. Density of states of an O ₂ molecule in a double sulfur vacancy.	68
Figure 7.1. (a) Optimized structures of the 2D Janus TMDs (relaxed with PBE) (b) and the band structures (calculated with HSE+SOC) of Mo-based (c) and W-based Janus TMDs. The dashed red line denotes the Fermi level. The red, green, and purple arrows denote the competing band gap energies: red (direct gap at the K point), purple (K point to low point of valence band), and green (indirect band gap of MoSTe and WSTe structures). The spin-orbit splitting at the K point (Δ SOc) is labeled in black.	77
Figure 7.2. Unrelaxed structures for zigzag (left, Z8) and armchair (right, A14) nanoribbons. The nanoribbon widths are characterized by the number of metal atoms in the unit cell. The unit cells are outlined with gray dashed lines and the zigzag/armchair edges are outlined in red on each structure.	80
Figure 7.3. Curvature energy as a function of nanoribbon width for (a) zigzag Mo-based nanoribbons, (b) zigzag W-based nanoribbons, (c) armchair Mo-based nanoribbons, and (d) armchair W-based nanoribbons.	81
Figure 7.4. Fully relaxed geometries for Z8 (a) MoSSe, (b) MoSTe, (c) MoSeTe, (d) WSSe, (e) WSTe, and (f) WSeTe. Fully relaxed geometries for A14 (g) MoSSe, (h) MoSTe, (i) MoSeTe, (j) WSSe, (k) WSTe, and (l) WSeTe.	83
Figure 7.5. Relaxed flat structures for Z8 (a) WSSe, (b) WSTe, and (c) WSeTe.	84
Figure 7.6. Magnetic moments vs nanoribbon width for (a) Mo-based and (b) W-based zigzag nanoribbons.	86
Figure 7.7. Schematic diagram of magnetic ordering of zigzag nanoribbons.	87
Figure 7.8. Band gaps vs. nanoribbon width for curved and flat armchair nanoribbons.	89
Figure 7.9. Fully relaxed geometries for hydrogen-passivated Z8 (a) MoSSe, (b) MoSTe, (c) MoSeTe, (d) WSSe, (e) WSTe, and (f) WSeTe. Fully relaxed geometries for hydrogen-passivated A14 (g) MoSSe, (h) MoSTe, (i) MoSeTe, (j) WSSe, (k) WSTe, and (l) WSeTe.	91
Figure 7.10. Schematic diagram of the magnetic ordering of hydrogen-passivated zigzag nanoribbons.	92
Figure 7.11. Band gaps of hydrogen-passivated and bare armchair nanoribbons.	94
Figure 8.1. Top and side views of the helical chain structure of bulk γ -Te (middle column), the rectangular structure of monolayer β -Te (left column), and the	

hexagonal structure of monolayer α -Te (right column), respectively. Bond lengths (represented by pink and blue lines), lattice parameters and interchain distances are given in the insets..... 102

Figure 8.2. The electronic band structure of bare a) β -Te and b) α -Te with (green) and without (blue) spin-orbit coupling (SOC) effects. 104

Figure 8.3. The cohesive energy (in eV per atom) as a function of lattice constant (for the a-direction) for 2D β -Te functionalized with H, O, and F. We observe one local and one global cohesive energy minimum for all functionalized structures except O- β -Te, which contains a single global minimum. The optimized geometry of the functionalized Tellurene structures at each minimum are depicted above and below the corresponding energy landscape. Bond breaking for O, H and F- β -Te is indicated by the orange dashed lines. The green dashed lines represent the lattice constant (in the a-direction) for bare monolayer α -Te and β -Te, respectively. 106

Figure 8.4. The phonon band structure and phonon projected density of states (PDOS), in addition to the electronic band structure and orbital projected density of states (PDOS) of (a) H- β -Te at its local energy minimum and (b) O- β -Te at its singular global energy minimum. For H- β -Te, the atomic movements at the negative frequency at the Y high symmetry point are shown (red arrows depict the vibration direction). 109

Figure 8.5. The phonon dispersion curves and phonon projected density of states (PDOS) of the F-functionalized α -Te and β -Te structures at the local and global minima. These dispersion curves and PDOS plots indicate that these structures are unstable in free standing form. Atomic movements for certain negative frequencies at the special high symmetry points are given in the insets..... 110

Figure 8.6. The electronic band structures and orbital projected density of states (PDOS) of functionalized Te structures at their local minimum and global minimum. 112

Figure 8.7. The optimized geometry of 2D α and β -Te when single H₂, O₂ and F₂ molecules are initially placed 2 Å above the surface..... 116

Figure 8.8. Initial and final (after 2 ps) snapshots of MD calculations at 300 K for high coverage of H₂, O₂, and F₂ molecules above the surface of a) α -Te and b) β -Te. 117

Chapter 1. Introduction

Two-dimensional materials are atomically thin crystalline materials that can exist in many structural phases and possess a wide range of properties, from insulating, semiconducting, and conducting to even topological or superconducting properties.¹⁻⁴ Two-dimensional semiconductors such as molybdenum disulfide (MoS_2) have attracted plenty of interest in recent years towards applications in field-effect transistors and other electronic devices.⁵⁻⁸ MoS_2 possesses an indirect band gap in its bulk, layered form, and a direct band gap in its monolayer form.⁹ This material exists in nature, but monolayers of MoS_2 can be readily synthesized with chemical vapor deposition techniques.¹⁰⁻¹⁴ As such, MoS_2 is a promising material for next-generation electronic devices.

1.1. Overview of Dissertation

This dissertation primarily focuses on the integration of high-quality dielectric layers with MoS_2 using atomic layer deposition (ALD). The motivation for this work, including the operation of metal-oxide-semiconductor field-effect transistors (MOSFETs) and the properties of two-dimensional MoS_2 are presented in Chapter 2. This chapter also provides an overview of the ALD process and introduces the difficulties in performing ALD on MoS_2 surfaces.

Chapter 3 describes the ALD reactor used in this work, along with the techniques used for preparing the MoS_2 surfaces. This chapter also describes the characterization techniques used to study the surfaces and interfaces of ALD films grown on MoS_2 . The

characterization of the surface morphology in particular is important to understand and improve ALD film growth on MoS₂.

While experimental techniques provide direct insight into the properties of a material, limitations can arise particularly in the detection of low numbers of interfacial molecules or atoms. Computational modeling can provide some insight into the interactions between molecules and the MoS₂ surface. In this work, density functional theory (DFT) was used to study the energetics of molecule-MoS₂ interactions. Chapter 4 describes the basics of DFT along with some practical details of its implementation.

The surfaces of MoS₂ prepared by different methods are variable and may contain differing concentrations of defects or contaminants. As such, ALD films grown on MoS₂ show varying levels of surface coverage. Chapter 5 studies the effects of surface preparation techniques on ALD film coverage. Surfaces prepared by mechanical exfoliation may exhibit contamination even after solvent cleaning, and thus display a large variation in film coverage. MoS₂ surfaces prepared by chemical vapor deposition (CVD) are more consistent and exhibit reproducible film coverage. Additionally, the growth of ALD films using two types of precursors are investigated. Different mechanisms of film growth between alkyl and alkyl amine precursors are suggested by differences in trends of surface coverage as a function of temperature.

Chapter 6 describes work done to alter the surface of MoS₂ and functionalize it for better ALD film growth. Reactive sulfur vacancies were formed in the MoS₂ surface via argon ion sputtering, and thiol molecules were introduced to passivate the vacancies and leave the surface amenable to ALD. Films grown on thiol-treated surfaces and vacancy-containing surfaces were continuous and morphologically similar. DFT

calculations showed that the thiol molecules attach primarily to sulfur vacancies. These calculations also showed that the ALD precursor molecule binds strongly to the sulfur vacancies, thus leading to uniform film growth on vacancy-containing surfaces. Further calculations determined that the electronic structure of MoS₂ is damaged by the creation of sulfur vacancies, but healing with thiol molecules restores the desirable electronic properties.

The remaining studies in this work aim to identify new electronic materials. Nanoribbons of transition metal dichalcogenides (TMDs) may have unique applications in nanoelectronics, spintronics, and as nanoscale metal-semiconductor junctions. Chapter 7 presents a DFT study of Janus TMD nanoribbons. Janus TMDs are similar to TMDs such as MoS₂, but the chalcogen atoms on one side are replaced with another chalcogen type resulting in an asymmetric material. This work investigates the spontaneous curvature of Janus TMD nanoribbons and the effects of curvature on the magnetic and electronic properties of these materials. The curvature has mild effects on the magnetic properties of zigzag-edged nanoribbons and a stronger effect on modulating the band gap of armchair-edged nanoribbons. These effects are dependent on the composition of the Janus nanoribbon. This study helps to identify new electronic materials and methods for tuning their properties to fit desired applications.

Chapter 8 presents a DFT study of two-dimensional Tellurene (Te) structures. This material exists in two phases known as α - and β -Te. In this study, Te structures are studied in both bare Te and hydrogen, oxygen, or fluorine-functionalized counterparts. The calculations investigate the stability and electronic properties of these materials

and find that while both bare Te phases are semiconducting, functionalized Te sheets are metallic except for H- β -Te. This study proposes that these materials are suitable for electronic devices or for metallic contacts in nanoscale junctions.

Chapter 9 summarizes the results of this work.

Chapter 2. Background Information

2.1. Metal-Oxide Semiconductor Field-Effect Transistors

The metal-oxide-semiconductor field-effect transistor (MOSFET) has been one of the most important devices in electronics since the early 1980s. Compared to other transistor designs, it is cheaper, simpler, and consumes less power in operation.¹⁵ There are two types of MOSFETs (n-channel and p-channel), of which there are several variations. Both operate under similar principles, with the difference being the type of charge carrier. As an example, a typical n-channel MOSFET (n-MOS, n-type charge carriers), is fabricated in bulk p-type silicon; a schematic is shown in Figure 2.1. Two n-type regions are created (the “source” and the “drain”) with a p-type silicon channel between them.

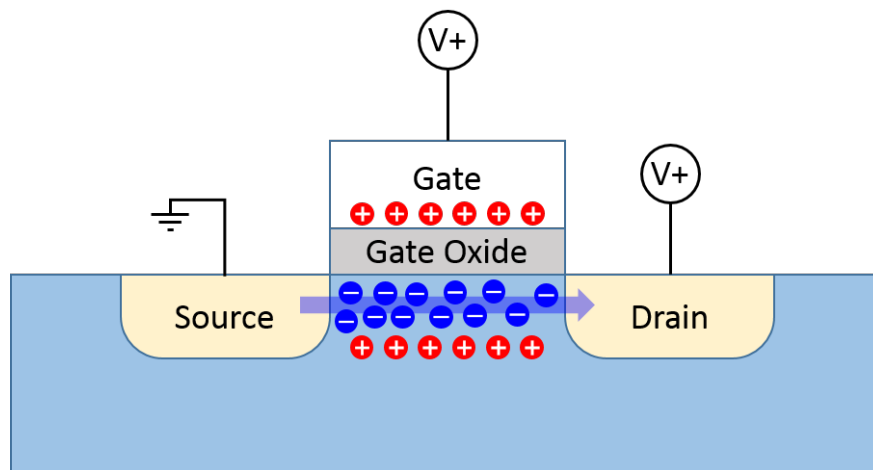


Figure 2.1. A typical n-type MOSFET in operation. The source and drain are formed from n-type silicon in a p-type silicon substrate. When a positive voltage is applied to the gate, positive charges are driven away from the gate. A voltage is then applied across the source and drain, and electrons may flow from the source to the drain. Redrawn from Ref. [16].

The gate is a metal-oxide-semiconductor (MOS) stack positioned between the source and the drain which acts as a capacitor. When a voltage is applied across the gate, an electric field is generated in the channel which draws a layer of electrons

toward the semiconductor surface. The region where electrons collect is known as the accumulation region. If a voltage is then applied to the drain, the electrons are allowed to flow out of the accumulation region and current flows through the transistor. The current thus depends on the electric field in the gate (the so-called field effect), and therefore on the gate capacitance. The capacitance is given by

$$C = \frac{\epsilon_0 k A}{t} \quad (2.1)$$

where ϵ_0 is the permittivity of free space, k is the relative dielectric constant of the oxide, A is the capacitor's area, and t is the oxide thickness. Traditionally, the oxide in MOSFETs has been silicon dioxide (SiO_2). To fit more transistors on a single chip, they must be made smaller (i.e. the transistor's gate length, and therefore the capacitor's area, must be reduced). By Equation (2.1), it is clear that if the capacitor's area is reduced, the gate oxide thickness must also be reduced to retain the same capacitance. In fact, the gate length is predicted to reach ~ 5 nm by 2030 by the International Technology Roadmap for Semiconductors,¹⁷ shown in Figure 2.2.

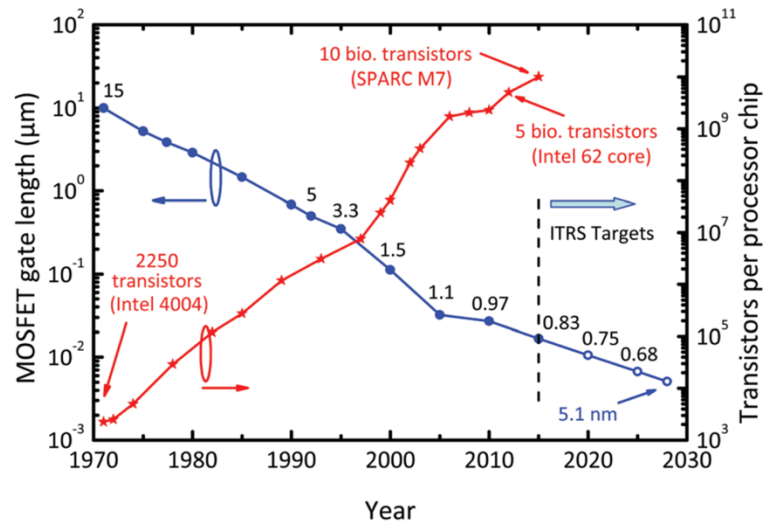


Figure 2.2. Predicted transistor gate length trend. The gate oxide thickness is directly related to the physical gate length. Reprinted from Ref. [17] – Published by The Royal Society of Chemistry.

The drive for increased transistor density and device performance means that the gate oxide layer has become so thin that electrons are able to tunnel through it. This current leakage leads to unacceptably high levels of power dissipation.¹⁸ Replacing the SiO₂ layer with a high-*k* dielectric allows for thicker gate oxides, which reduces leakage current while retaining a high capacitance. The thickness of the high-*k* dielectric is related to its equivalent SiO₂ thickness, or equivalent oxide thickness (EOT), as

$$\text{EOT} = \left(\frac{3.9}{\kappa}\right) t_{\text{high-}k} \quad (2.2)$$

where 3.9 is the relative dielectric constant of SiO₂ and $t_{\text{high-}k}$ is the thickness of the new dielectric material. Equation (2.2) demonstrates how a high-*k* layer may be made physically thicker than the SiO₂ layer it replaces by the ratio of the materials' dielectric constants while retaining the properties of a thin SiO₂ layer. Another important requirement in device fabrication is a high-quality interface between the semiconductor and the gate dielectric. Atomic layer deposition (ALD) provides a controlled method for integrating high-*k* metal oxides with silicon. In fact, in 2007 Intel first used ALD to deposit hafnium dioxide (HfO₂) as part of the fabrication process for its 45nm transistors.^{16,19}

2.2. Transition Metal Dichalcogenides

While the integration of high-*k* dielectrics on silicon has proved beneficial for device scaling, classic semiconductor materials (silicon and germanium) can only go so far toward the scaling of nanoelectronics, and other avenues must be explored. Gallium arsenide and other III-V materials can help with device scaling because of

their high charge carrier mobility.^{20,21} However, these materials suffer from source-drain tunneling as the channel length narrows below 5 nm.^{17,22} A different class of materials known as transition metal dichalcogenides (TMDs) may provide an alternate route to device scaling. TMDs are layered materials of the form MX_2 (M = metal, X = S, Se, or Te) with layers bound by van der Waals forces. Individual TMD layers (i.e. monolayers) possess a direct band gap – they are atomically thin semiconductors. TMDs possess a physical structure similar to graphene, and thin layers may be prepared by mechanical exfoliation from bulk crystals,^{23,24} or by chemical vapor deposition.^{10,11,13,12,14} Monolayer TMDs are also highly transparent and flexible, making them good candidates for flexible or transparent electronics.²⁵ MoS_2 is one of the most promising TMD semiconductors, possessing an indirect band gap of ~ 1.29 eV in bulk form and a direct band gap of ~ 1.8 eV in monolayer form.⁹ MoS_2 has a theoretical charge carrier mobility of ~ 410 $\text{cm}^2 \text{V}^{-1} \text{s}^{-1}$.²⁶ In single-layer MoS_2 transistors, carrier mobility as high as ~ 200 $\text{cm}^2 \text{V}^{-1} \text{s}^{-1}$ has been demonstrated,⁶ which is comparable to the carrier mobility of 2 nm strained silicon films.²⁷ TMDs such as MoS_2 may be more resistant to source-drain tunneling effects because of their heavier charge carrier effective mass, allowing for shorter channel lengths.¹⁷ Recently, this was demonstrated by Desai et al. who fabricated a MoS_2 -based MOSFET with a 1 nm channel length and a source-drain tunneling current two orders of magnitude lower than an equivalent Si-based device.⁸

The integration of high- k dielectrics with single- or few-layer MoS_2 makes it possible to fabricate nanoscale transistors with MoS_2 as the channel material. Not only are individual MoS_2 layers less than 1 nm in thickness, it has been proposed that the

use of high- k dielectrics as gate oxides can assist in scaling down the channel length.²⁸ Additionally, the dielectric may enhance the charge carrier mobility in single layers of MoS₂.^{6,29,30} The fabrication of MOSFETs has been demonstrated using MoS₂ and atomic layer deposited HfO₂ and Al₂O₃.^{6,30–33}

2.3. Atomic Layer Deposition

Atomic layer deposition (ALD) was invented in 1977 by the name of “atomic layer epitaxy” (ALE) by Tuomo Suntola.³⁴ ALD is a thin film growth technique that relies on specific chemical interactions between gas-phase molecules and the surface upon which the film is to be grown. In this respect, it is similar to chemical vapor deposition (CVD). The major difference between ALD and CVD, however, is that ALD does not allow the chemical reactants (known as precursors) to be in the reaction chamber at the same time. Instead, the precursors are introduced sequentially and in a cyclic manner to react with the surface. The chamber is purged with inert gas between reactions. For the growth of metal oxides, the deposition is a two-step process (cartoon schematic shown in Figure 2.3):

- i. Precursor 1 (a metal-organic molecule) is introduced to the desired surface, where it is allowed to react and bond with the surface. The surface chemistry is now altered from its original state. Unreacted molecules are purged with inert gas.
- ii. Precursor 2 (an oxidizer) is introduced to the surface where it may react with Precursor 1. The surface chemistry is returned to its initial state. Unreacted molecules and reaction byproducts are purged with inert gas. In most cases, the

oxidizer is water, though other oxidizers such as oxygen plasma or ozone can be used.³⁵

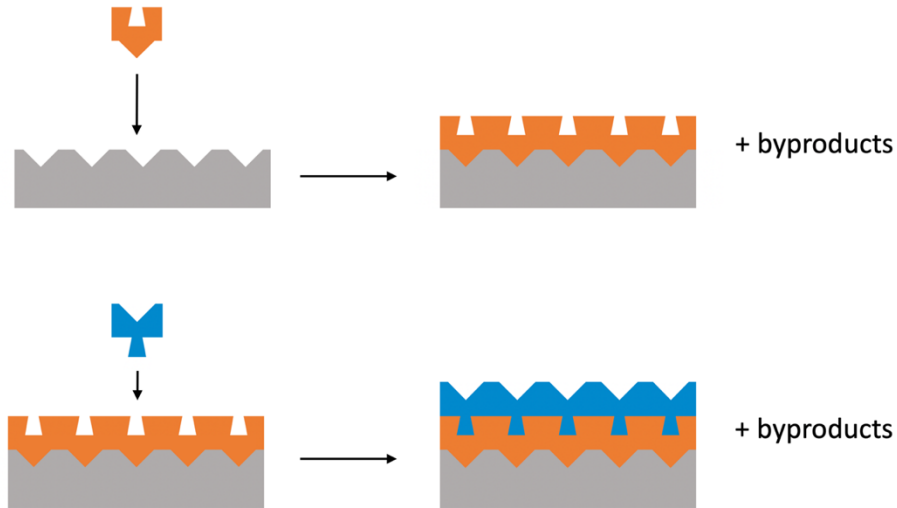


Figure 2.3. Cartoon schematic of one ALD cycle, redrawn from Ref. [36].

These two steps make up one ALD cycle which may be repeated as many times as necessary to grow the desired thickness of film. The ideal process is self-limiting. Once the surface is covered with a monolayer of either precursor, there are no more surface sites for the precursor to occupy and no further reaction occurs. Excess precursor is pumped out of the chamber in the purge step. Because of its self-limiting nature, the ALD process allows for sub-nanometer control of the film's thickness and for conformal, uniform film growth.

The ideal ALD reaction is the ligand-exchange mechanism. An example of the ligand-exchange process is shown in Figure 2.4 for a process using tetrakis (dimethylamino) titanium (TDMAT, $[(\text{CH}_3)_2\text{N}]_4\text{Ti}$) and water to form TiO_2 . The metal oxide is formed when the ligands of Precursor 1 (TDMAT) are exchanged for the oxygen of Precursor 2 (H_2O) during the second half of the ALD cycle. The organic ligands are thus released and pumped out of the chamber.³⁵

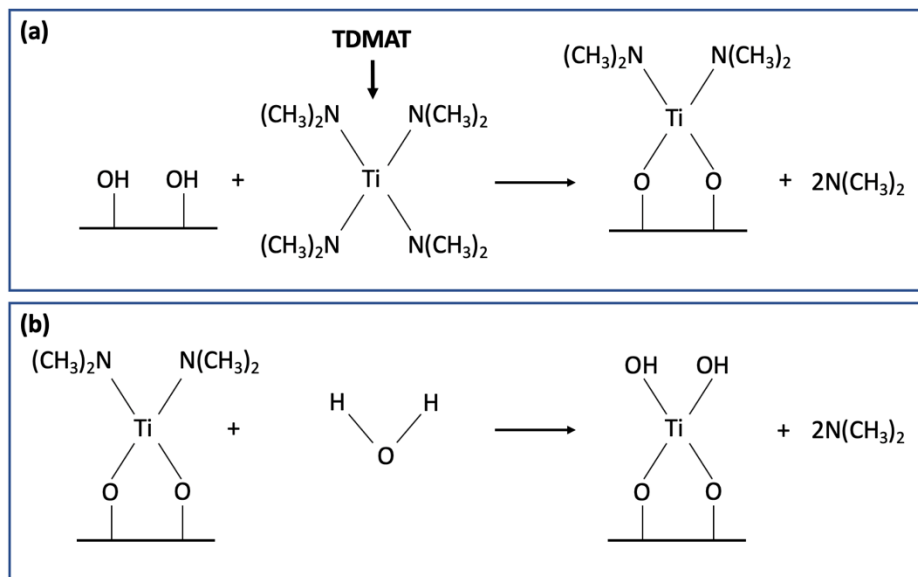


Figure 2.4. Schematic of the ligand-exchange mechanism for an ALD process using tetrakis (dimethylamino) titanium (TDMAT) and water. The starting surface is $-\text{OH}$ terminated. In the first half cycle (a), TDMAT reacts with the $-\text{OH}$ terminated surface, releasing methyl ligands. In the second half cycle (b), water reacts with the TDMAT on the surface, releasing the remaining ligands and leaving the surface $-\text{OH}$ terminated once more.

The ALD process is carried out under vacuum (typically ~ 0.2 Torr) and at temperatures of $100\text{-}400$ $^{\circ}\text{C}$. The behavior is not always ideal; too low of a temperature can result in precursor condensation or incomplete reaction, whereas too high of a temperature can result in precursor decomposition or desorption of surface species. Thus, reactions must take place in the “ALD window” (shown in Figure 2.5). This is the temperature range under which the growth rate, the film thickness increase per ALD cycle, is relatively constant.³⁶ The ALD window depends on the specific precursors used.

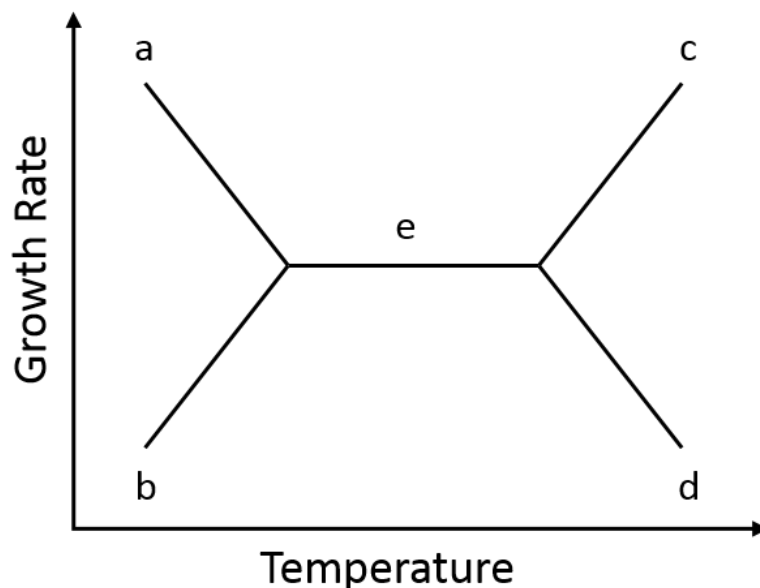


Figure 2.5. Schematic of ALD growth rate as a function of temperature. The growth rate in (a) increases as a result of precursor condensation and decreases in (b) as a result of incomplete reactions. In (c), precursor decomposition drives up the growth rate, and in (d), precursor desorption lowers the growth rate. The ALD window is represented by (e) where the growth per cycle is relatively constant.

2.4. Motivation

The surface chemistry is of great importance in ALD. Hydrophilic surfaces with dangling $-OH$ bonds (such as SiO_2) are amenable to film growth whereas hydrophobic surfaces are not.³⁷ MoS_2 surfaces are extremely hydrophobic and inert, lacking the necessary dangling bonds. ALD on pristine MoS_2 surfaces results in “island growth” as the film nucleates only on surface defect sites.^{38,39} To promote high-quality film growth, surface functionalization must occur before ALD. Several functionalization techniques have been explored elsewhere, including plasma treatment, interfacial seed layers, and organic seed layers.^{33,38,40–44} However, these techniques often require special equipment, and may also be time consuming.

A comprehensive understanding of the interface between MoS₂ and dielectric layers is necessary to enable the development of devices based on these materials. This work aims to provide insight into the mechanisms of film growth on MoS₂ surfaces and thus advance knowledge towards device scaling using these materials.

Chapter 3. Experimental Methods

3.1. ALD Reactor

Depositions were performed in a custom-built stainless-steel hot wall flow tube type ALD reactor (Figure 3.1) that is described in more detail by Henegar and Gougousi.⁴⁵ The precursors are introduced by the fixed volume method⁴⁶ and are carried into the reaction chamber by 17 sccm of ultrahigh purity nitrogen gas. The chamber is actively pumped with a rotary vane oil pump to maintain a processing pressure of ~ 200 mTorr. The reactor is equipped with two metal-organic precursor delivery lines, one of which is heated. The heated line delivers tetrakis (dimethylamino) titanium (TDMAT) or tetrakis (dimethylamino) hafnium (TDMAH) for the deposition of TiO_2 or HfO_2 , respectively. The unheated line delivers trimethyl aluminum (TMA) for the deposition of Al_2O_3 . A third line delivers water into the chamber.

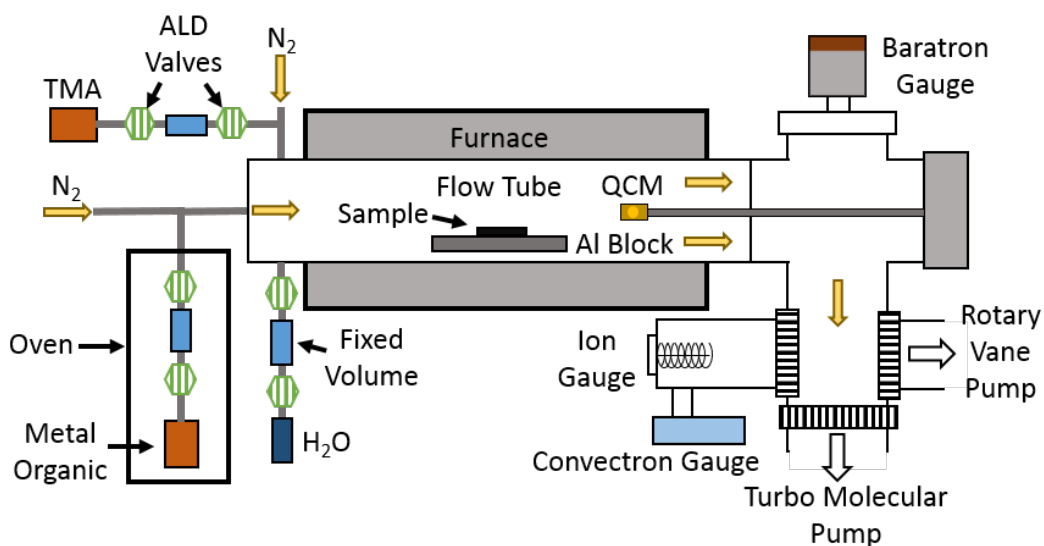


Figure 3.1. Diagram of the ALD reactor to be used for growth of metal oxides on MoS_2 . Reprinted with permission from Ref. [47].

3.2. Sample Preparation

3.2.1. Mechanical Exfoliation

The mechanical exfoliation of two-dimensional materials stems from the original studies of graphene in 2004.²³ Layers of graphite or TMDs may be peeled from bulk samples using Scotch tape, after which they may be transferred to silicon wafers or some other substrate. While mechanical exfoliation of graphene onto silicon benefits from strong adhesion of graphene to SiO₂, exfoliation of MoS₂ and other TMDs does not,⁴⁸ resulting in low yield and small flakes.

Several modifications of the “Scotch tape method” have been employed.⁴⁸⁻⁵⁰ The method used in this work is a modification of the method used by Huang et al.⁵⁰ Semiconductor dicing tape (Semiconductor Equipment Corp.) is used to peel layers of MoS₂ from a bulk crystal (SPI Supplies). The material attached to the tape is thinned with another piece of tape up to 10 times before transfer to a clean silicon wafer topped with 300 nm or 500 nm of SiO₂. The thick oxide layer on the silicon wafer increases the optical contrast to allow for visual identification of mono- and few-layer flakes using an optical microscope.^{51,52} The tape is pressed firmly to the wafer before the wafer is placed on a 100°C hotplate for ~30 s. After annealing on the hotplate, the tape is pressed firmly to the wafer again to remove gases trapped between the MoS₂ layer and the substrate, improving adhesion to the substrate.⁵⁰ The tape is carefully removed, leaving behind few-layer MoS₂ flakes that are up to 10-15 μm in length. The optical contrast between the MoS₂ flakes and the SiO₂ substrate allows for identification of the flakes using optical microscopy, as shown in Figure 3.2.

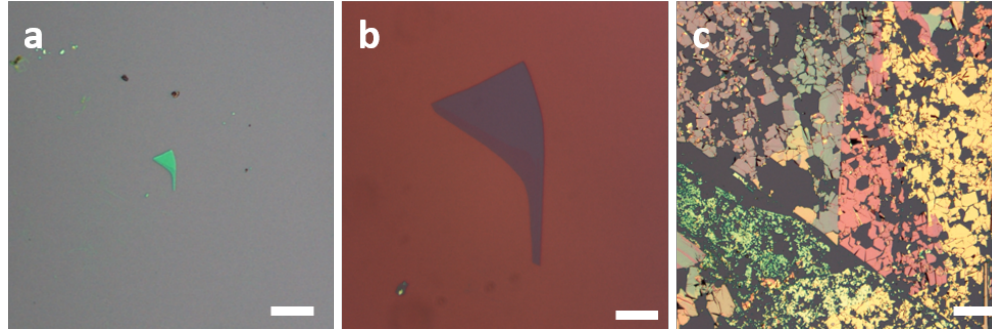


Figure 3.2. Optical images of exfoliated MoS₂ flakes on 500 nm SiO₂ substrates. A single MoS₂ flake is shown in (a) and (b) at different magnifications. In (c), various thicknesses of MoS₂ flakes are shown (color is thickness-dependent). Scale bars are 50 μm for (a) and (c) and 10 μm for (b).

The color of the flake corresponds to its thickness, allowing for easy identification of very thin flakes which appear green at low magnification (Figure 3.2a). An optical image with corresponding atomic force microscopy scan is shown in Figure 3.3.

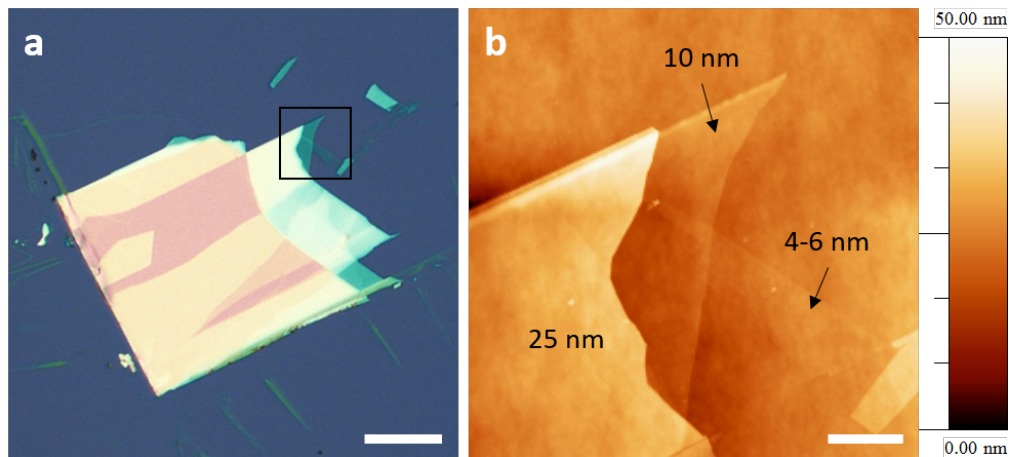


Figure 3.3. (a) Optical image of an exfoliated MoS₂ flake on 500 nm SiO₂. The black square marks the region scanned with AFM in (b). The step heights of selected regions are also shown in (b). The scale bars correspond to (a) 50 μm and (b) 5 μm.

3.3. Characterization Techniques

3.3.1. Atomic Force Microscopy

Atomic force microscopy (AFM) is a scanning probe measurement capable of mapping the topography of a sample with sub-nanometer precision. The instrument

consists of a stylus-type tip on a flexible cantilever, mounted on a piezoelectric crystal. The tip is scanned across and allowed to make contact with the surface of interest. A laser beam reflects off the cantilever as it interacts with the surface's features. The reflected beam impinges on a split photodiode which measures the position of the laser spot (Figure 3.4). The signal measured by the photodetector controls the piezoelectric crystal using a feedback system to offset the tip displacement and maintain a constant force between the tip and sample.^{53,54} The offset displacement provides the desired surface height information.⁵⁵ In the commonly used non-contact (tapping) mode, the cantilever is oscillated near its resonant frequency, typically around 10-100 kHz. This mode allows the tip to experience strong forces in the vertical direction while experiencing very little lateral force.⁵⁴

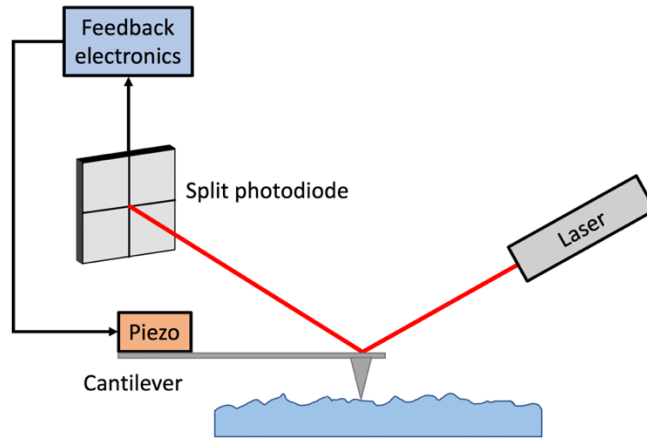


Figure 3.4. Basic operation of an atomic force microscope. The cantilever deflection is measured by the laser's reflection on the photodiode and modulated by a piezoelectric crystal.

One important parameter that can be extracted from the height information is the RMS roughness,

$$\sigma = \sqrt{\frac{1}{N} \sum_i (z_i - z_{avg})^2} \quad (3.1)$$

where z_i is the height of a single point and z_{avg} is the average height of the surface. The RMS roughness measurement provides some insight into the smoothness and uniform nature of a surface, in that a surface with large variations in height will have a higher RMS roughness. For the ALD films considered in this work, the RMS roughness is a proxy for the quality of the film. Poor quality films with many gaps or pinholes exhibit higher RMS roughness, and smoother, more uniform films exhibit RMS roughness closer to that of bare silicon.

3.3.2. X-ray Photoelectron Spectroscopy

X-ray photoelectron spectroscopy (XPS) is a surface-sensitive technique used for analyzing elemental composition and bonding environments of materials. The principle of XPS is the photoelectric effect. A beam of x-ray light impinges on a material, causing core-level electrons to be emitted from the surface of the material (Figure 3.5). The energy of an emitted electron is dependent on both the atom from which the electron came and the atom's bonding environment. The quantity of interest is the electron's binding energy (BE) which is found by measuring the electron's kinetic energy (KE) and by using the following relation,

$$BE = h\nu - KE - \phi \quad (3.2)$$

where $h\nu$ is the x-ray energy and ϕ is the work function of the detector. The binding energy of an electron is specific to the atom and the orbital from which the electron originates. Different chemical bonding environments may shift the binding energy by several eV, and such shifts are easily measured, allowing for chemical analysis.

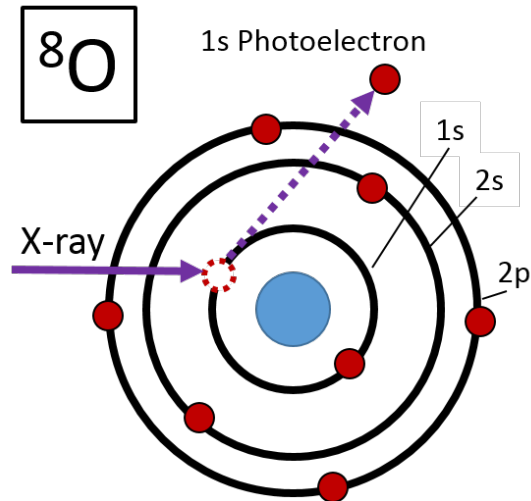


Figure 3.5. Schematic of an x-ray ejecting a core electron from an oxygen atom. The binding energy of an ejected electron is specific to the atom and orbital from which the electron originates. Reprinted with permission from Ref. [47].

XPS is surface sensitive. While the x-rays may penetrate 1000 nm or more into a material, the ejected electrons are susceptible to inelastic scattering. The sampling depth depends on the electron's inelastic mean free path (IMFP), λ . We only detect electrons from within a depth of about 3λ , which is typically about 10 nm.⁵⁴ For a thin film on a substrate, the intensity of emitted photoelectrons can be described by Beer's law,

$$I_{k_o} = I_{0_o} \left[1 - e^{-\frac{d}{\lambda \cos \theta}} \right] \quad (3.3)$$

$$I_{k_s} = I_{0_s} e^{-\frac{d}{\lambda \cos \theta}}$$

where the subscripts o and s specify the thin film overlayer and substrate, respectively. The angle θ is the angle between the emitted beam and the normal direction.

The number of electrons detected at a certain energy is proportional to the number of its source atom, allowing for quantitative study of the material. That is, the material's stoichiometry can be determined by measuring the binding energy peak areas. Thus,

XPS may be used to study the surface chemistry of materials with high sensitivity.

Atomic concentrations can be calculated as

$$n_i = \frac{I_i/S_i}{\sum_j I_j/S_j} \quad (3.4)$$

where n_i is the concentration of element i , I is the peak intensity, and S is the relative sensitivity factor (RSF). The sum over j includes all elements in the sample. The RSF depends on both the element and the transition from which the electron originates and is necessary to scale measured peak areas so that atomic concentrations can be calculated properly. Because of sample charging effects, it is necessary to calibrate the spectra before peak fitting. Typically, this is done by shifting the spectra so that the C 1s peak is at 284.8 eV. This peak is known as adventitious carbon, and is present in nearly every sample.⁵⁶

Depth profiling of materials can be performed by removing surface atomic layers via ion sputtering. This is typically performed by bombarding the surface with argon ions with energies ranging between 0.5-5 keV.⁵⁷ This technique allows for sampling of the material below the maximum sampling depth. Though argon ion sputtering is usually used to remove complete layers of material from the surface, other effects are possible. Particularly, sputtering the MoS₂ surface with low energy (~500 eV) argon ions was found to selectively remove sulfur atoms and create single sulfur vacancies.⁵⁸⁻

⁶⁰ This approach is employed here to create reactive MoS₂ surfaces prior to ALD of metal oxide thin films.

XPS data collection and argon ion sputtering for this work were performed at the University of Maryland, College Park using a Kratos AXIS 165 spectrometer. Sputtering and data collection were performed with the assistance of Dr. Karen Gaskell.

Chapter 4. Density Functional Theory

Density functional theory (DFT) is one of the most widely used computational techniques for studying materials at a quantum mechanical level. It is commonly used to model the properties of molecules, solids, surfaces, and interfaces. The aim of DFT is to solve the many-body Schrodinger equation for N electrons in a material,

$$\left[-\frac{\hbar^2}{2m} \sum_{i=1}^N \nabla_i^2 + \sum_{i=1}^N V(\mathbf{r}_i) + \sum_{i=1}^N \sum_{j<i}^N U(\mathbf{r}_i, \mathbf{r}_j) \right] \psi = E\psi \quad (4.1)$$

The first term in Equation (4.1) is the kinetic energy, the second term is the external potential (from the nuclei), and the third term is the electron-electron interaction potential. On the right side of Equation (4.1), E is the total energy and ψ is the electron wave function.

Solving the Schrodinger equation directly is practically impossible, as the solution has $3N$ dimensions (3 spatial dimensions for each of N electrons). Density functional theory seeks to make this problem tractable by reducing its dimensionality. As the name suggests, DFT relies on knowledge of the electron density,

$$n(\mathbf{r}) = 2 \sum_i \psi_i^*(\mathbf{r})\psi_i(\mathbf{r}) \quad (4.2)$$

where the sum is over all occupied electron wavefunctions.⁶¹ The factor of 2 arises from the fact that an electron may be either spin-up or spin-down.

4.1. Hohenberg-Kohn Theorems

The DFT approach depends on two theorems presented by Hohenberg and Kohn in the 1960s.⁶² The first Hohenberg-Kohn theorem states that the ground state energy from

the Schrodinger equation is a unique functional of the electron density. That is, the ground state energy E can be expressed as $E[n(\mathbf{r})]$. This theorem means that all properties of a system are uniquely determined by the ground-state electron density. The most important consequence of this fact is that the problem is reduced from $3N$ dimensions to simply 3 dimensions, since now the positions of all electrons are not required, but simply the electron density. If the energy functional and electron density are known exactly, then all properties of the system can be determined. Unfortunately, the exact form of the functional is not generally known.

The second Hohenberg-Kohn theorem describes an important property of the functional. It states that the electron density that minimizes the energy of the functional is the true electron density that corresponds to the full solution of the Schrodinger equation. Therefore, if the energy functional can be minimized by varying the electron density, the true electron density can be found. While the exact form of the energy functional is not known, approximate forms can be used to find approximate, yet useful, solutions to the Schrodinger equation. The Kohn-Sham approach is to recast the problem in terms of non-interacting electrons with the same electron density. The energy functional can be written in terms of single-electron wavefunctions, $\psi_i(\mathbf{r})$ (which define the electron density), as

$$E[\{\psi_i\}] = E_{known}[\{\psi_i\}] + E_{XC}[\{\psi_i\}] \quad (4.3)$$

where the functional is split into the known part (E_{known}) and exchange-correlation part (E_{XC}). The known part of the functional includes terms for the electron kinetic energies, Coulomb interactions between electrons and nuclei, electron-electron

Coulomb interactions, and nucleus-nucleus Coulomb interactions. This part of the functional can be written as

$$\begin{aligned}
 E_{known}[\{\psi_i\}] = & -\frac{\hbar^2}{m} \sum_i \int \psi_i^* \nabla^2 \psi_i d^3r + \int V(\mathbf{r})n(\mathbf{r})d^3r \\
 & + \frac{e^2}{2} \iint \frac{n(\mathbf{r})n(\mathbf{r}')}{|\mathbf{r} - \mathbf{r}'|} d^3r d^3r' + E_{ion}
 \end{aligned} \tag{4.4}$$

The remaining term in the full energy functional is the exchange-correlation functional, E_{XC} , which arises from mapping the full interacting system to a non-interacting system. This term contains all effects that are not included in E_{known} , the most important of which are the exchange energy and the correlation energy. The exchange energy arises from the fact that electrons are fermions, and the wave function is antisymmetric under exchange of any two electrons. The exchange energy is the energy associated with interchanging two electrons under this condition. The correlation energy is the energy associated with how a single electron is affected by all other electrons. In essence, this is a result of screening effects. In the Kohn-Sham formalism described below, the exact exchange-correlation functional is typically unknown, and therefore practical applications of DFT rely on approximating this functional.

4.2. Kohn-Sham Equations

Thus far, the Schrodinger equation is still insoluble, as the electron density that minimizes the energy functional is still unknown. Kohn and Sham presented a solution to this problem in 1965.⁶³ The Kohn-Sham approach is to construct a fictitious system

of non-interacting electrons that has the same electron density as the physical system.

The Kohn-Sham equations are single particle equations of the form

$$\left[-\frac{\hbar^2}{2m}\nabla^2 + V(\mathbf{r}) + V_H(\mathbf{r}) + V_{XC}(\mathbf{r}) \right] \psi_i(\mathbf{r}) = \varepsilon_i \psi_i(\mathbf{r}) \quad (4.5)$$

In this equation, the potential V describes the interaction of the electron with the atomic nuclei. The second potential, V_H is the Hartree potential,

$$V_H = e^2 \int \frac{n(\mathbf{r}')}{|\mathbf{r} - \mathbf{r}'|} d^3r' \quad (4.6)$$

which describes the Coulomb interaction between the considered electron and the total electron density formed by all electrons in the system. Finally, the potential V_{XC} is the exchange-correlation potential. This potential can be defined as a functional derivative,

$$V_{XC} = \frac{\delta E_{XC}(\mathbf{r})}{\delta n(\mathbf{r})} \quad (4.7)$$

To solve the Kohn-Sham equations, one must find the Hartree potential. However, the Hartree potential is dependent on the electron density which is as yet unknown. In practice, this can be solved in an iterative way:

1. Define a trial electron density $n(\mathbf{r})$.
2. Solve the Kohn-Sham equations using the trial electron density and find the single electron wavefunctions $\psi_i(\mathbf{r})$.
3. Calculate the electron density from the Kohn-Sham single electron wavefunctions, $n_{KS}(\mathbf{r}) = 2 \sum_i \psi_i^*(\mathbf{r})\psi_i(\mathbf{r})$.
4. Compare the trial density $n(\mathbf{r})$ to the calculated density $n_{KS}(\mathbf{r})$. If the densities differ by more than some threshold, update the trial density and repeat steps 2 and 3 until the densities are sufficiently similar.

Once this process is complete to a satisfactory threshold, the ground-state electron density has been found. The exchange-correlation potential, V_{XC} , is still unknown.

4.3. Exchange-Correlation Functionals

In practice, DFT relies on approximating the exchange-correlation functional. There are many approaches to this problem, but the most common methods are the local density approximation (LDA) and the generalized gradient approximation (GGA). The form of the exchange-correlation functional is typically not known. However, it can be exactly derived for the case of the uniform electron gas ($n(\mathbf{r}) = \text{constant}$), and this forms the basis of both the LDA and GGA methods. For LDA, the exchange-correlation potential at a point is approximated as the exchange-correlation potential of the uniform electron gas at the electron density observed at that point (the local density).^{63,64} If the density is slowly varying, the exchange-correlation potential can be written as

$$E_{XC}[n(\mathbf{r})] = \int n(\mathbf{r})\epsilon_{XC}(n(\mathbf{r}))d\mathbf{r} \quad (4.8)$$

where $\epsilon_{XC}(n)$ is the exchange-correlation energy per electron of a uniform electron gas with density n . The LDA functional has seen widespread use and success in the DFT world, though it is known to underestimate material properties such as lattice parameters.

The GGA method aims to include more physical information in the approximation to the exchange-correlation functional. It includes information about the local gradient of the electron density along with the local density itself, in a form such as

$$E_{xc}[n(\mathbf{r})] = \int f(n(\mathbf{r}), \nabla n(\mathbf{r})) d\mathbf{r} \quad (4.9)$$

where f is some function of the electron density and the gradient of the electron density. There are several implementations of GGA, including that of Perdew et. al (PW91)⁶⁵ and Perdew-Burke-Ernzerhof (PBE).⁶⁶ The PBE functional is widely used as it provides a good tradeoff between accuracy and computation time, although it is known to underestimate electronic band gaps.

Higher-order functionals also exist that use even more physical information such as the kinetic energy density. However, these methods are more computationally demanding and the tradeoff between accuracy and computation time must be considered.

4.4. Computational Details

4.4.1. K-points

Density functional theory seeks to solve the Schrodinger equation for periodic systems. Bloch's theorem states that the eigenstates for an electron in a periodic potential can be expressed as

$$\phi_{\mathbf{k}}(\mathbf{r}) = e^{i\mathbf{k} \cdot \mathbf{r}} u_{\mathbf{k}}(\mathbf{r}) \quad (4.10)$$

where $u_{\mathbf{k}}(\mathbf{r})$ has the same periodicity as the unit cell, i.e. $u_{\mathbf{k}}(\mathbf{r}) = u_{\mathbf{k}}(\mathbf{r} + \mathbf{R})$, and \mathbf{k} is the electron wave vector.⁶⁷ In DFT calculations, integrals over k-space are computed numerically. Thus, k-space can be sampled by specifying a specific number of k-points. The Monkhorst-Pack method requires only that the number of k-points to be used along each reciprocal direction is specified.⁶⁸ As the number of k-points increases, so does the accuracy of the calculation, but also the computational time. The computational

time scales roughly linearly as the number of k-points increases. One can determine the k-point convergence by plotting the total energy of a system as a function of k-points. The k-point convergence of a monolayer of MoS₂ is plotted in Figure 4.1.

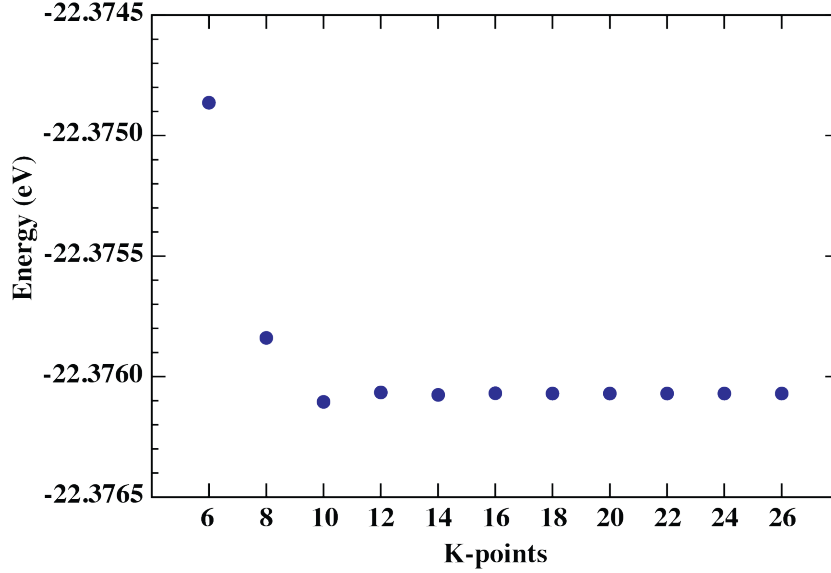


Figure 4.1. Total energy of MoS₂ as a function of k points.

Here, the k-points were specified as $M \times M \times 1$, as only one k-point is required in the vertical direction. The total energy does not change after 12 k-points, and the calculation is said to be converged at this k-point value. Increasing the number of k-points beyond this point does not increase the accuracy of the calculation.

4.4.2. Energy Cutoff

The potential $u_k(\mathbf{r})$ from Bloch's theorem (Equation (4.10)) is periodic and can be expanded as a series of plane waves,

$$u_k(\mathbf{r}) = \sum_{\mathbf{G}} c_{\mathbf{G}} e^{i\mathbf{G} \cdot \mathbf{r}} \quad (4.11)$$

where $\mathbf{G} = m_1 \mathbf{b}_1 + m_2 \mathbf{b}_2 + m_3 \mathbf{b}_3$. Here, \mathbf{b}_i are the reciprocal lattice vectors and m_i are integers. Now, Equation (4.10) becomes

$$\phi_k(\mathbf{r}) = \sum_{\mathbf{G}} c_{\mathbf{k}+\mathbf{G}} e^{i(\mathbf{k}+\mathbf{G}) \cdot \mathbf{r}} \quad (4.12)$$

and these solutions to the Schrodinger equation have energy

$$E = \frac{\hbar^2}{2m} |\mathbf{k} + \mathbf{G}|^2 \quad (4.13)$$

In DFT, it is practical to consider solutions only below some cutoff energy,

$$E_{cut} \leq \frac{\hbar^2}{2m} G_{cut}^2 \quad (4.14)$$

so that Equation (4.10) becomes a finite sum,

$$\phi_k(\mathbf{r}) = \sum_{|\mathbf{k}+\mathbf{G}| < G_{cut}} c_{\mathbf{k}+\mathbf{G}} e^{i(\mathbf{k}+\mathbf{G}) \cdot \mathbf{r}} \quad (4.15)$$

The cutoff energy parameter must be tested for convergence in DFT calculations, similar to the k point convergence testing.⁶¹ The total energy of a MoS₂ monolayer as a function of cutoff energy is shown in Figure 4.2.

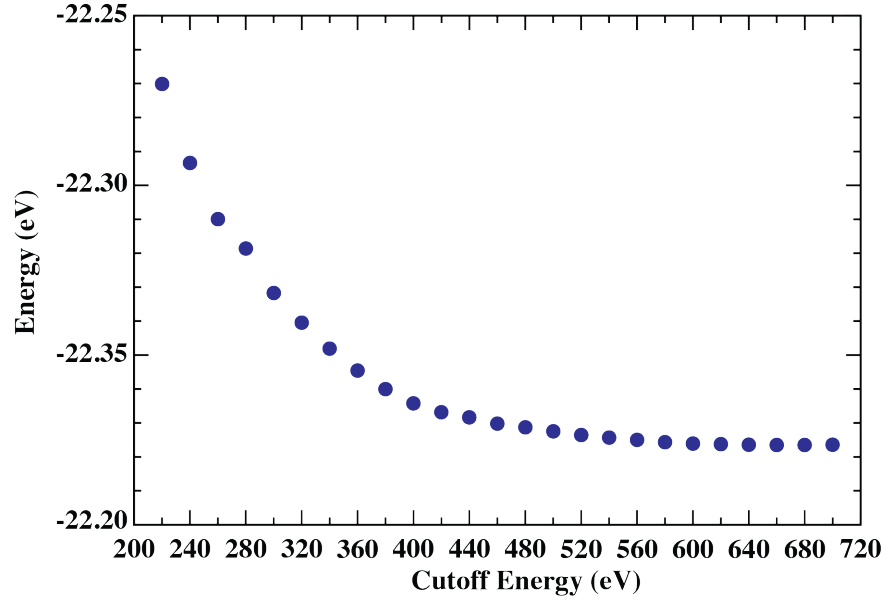


Figure 4.2. Total energy of MoS₂ as a function of cutoff energy.

4.4.3. Pseudopotentials

The previous section outlined how a plane-wave basis set may be used to calculate solutions to the Schrodinger equation. However, including terms for all electrons in a material is computationally demanding. Physically, core electrons are not as important as valence electrons for chemical bonding and other material properties. Since the computational cost of DFT calculations scales like N^3 for systems of N electrons, pseudopotentials are adopted to reduce computational demands. Pseudopotentials use a smoothed electron density for the core electrons that matches the physical properties of the true core. Above a certain cutoff radius r_c , the pseudopotential should match the actual potential (Figure 4.3a). Similarly, the pseudo-wave function should match the real wavefunction above the cutoff radius (Figure 4.3b) This method reduces the number of plane waves that must be included in the calculation and saves

computational time while not sacrificing much accuracy in the calculation of physical properties.⁶¹

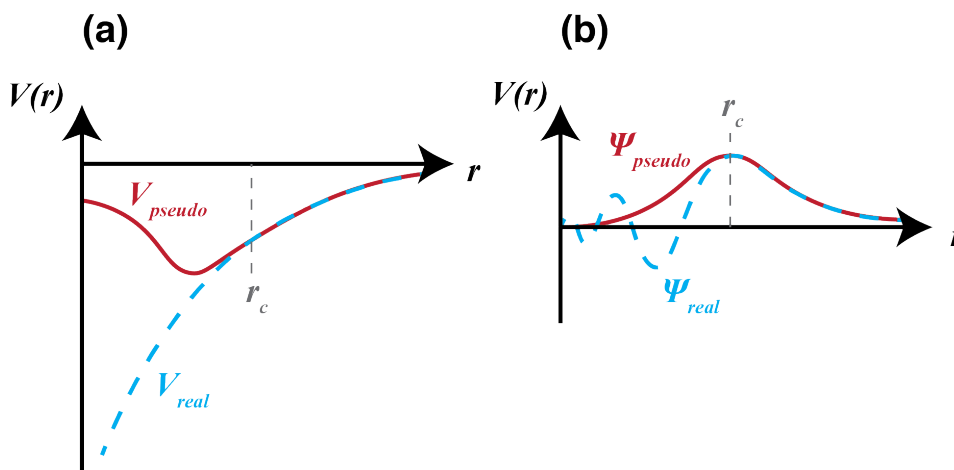


Figure 4.3. (a) Comparison of the real potential, V , to the pseudopotential, V_{pseudo} , and (b) comparison of the real wave function to the pseudo-wave function. Above the cutoff radius r_c , the potentials and the wave functions match.

Two common pseudopotential forms are norm-conserving pseudopotentials⁶⁹ and ultrasoft pseudopotentials.⁷⁰ Both methods aim to reduce computational demands by lowering the required cutoff energy. Norm-conserving pseudopotentials enforce the conditions that inside the cutoff radius, the norm of the pseudo-wave function is identical to that of the all-electron wave function, while outside the cutoff radius the pseudo-wave function and all-electron wave function are identical.⁶⁹ Ultrasoft pseudopotentials relax the norm-conserving constraint by introducing augmentation charges below the cutoff radius to account for the charge density difference between the all-electron wave function and the pseudo-wave function. The augmentation charges can be treated more efficiently than the all-electron charge density.^{70,71}

The projector augmented wave method (PAW) is a related method that uses the full wave function.⁷² This method uses a transformation operator to smooth the wave function in a manner similar to changing from the Schrodinger picture to the

Heisenberg picture. Since the transformation from pseudo-wave function to all-electron wave function is known, physical properties can be extracted from the pseudo-wave function. This method differs from the aforementioned norm-conserving and ultrasoft pseudopotential methods because it does not split the wave function into two parts. PAW potentials are generally more accurate than ultrasoft pseudopotentials because they have smaller cutoff radii. Further, they can reconstruct the exact wave function in the core region. Although derived differently, the PAW method is related to the ultrasoft pseudopotential method and can be implemented in codes based on ultrasoft pseudopotentials.⁷¹ Calculations in this work are performed using the Vienna ab Initio Simulation Package (VASP)⁷³ using the PAW method.

Chapter 5. Atomic Layer Deposition of Al₂O₃ and TiO₂ on MoS₂ surfaces

This chapter is based on the published manuscript Atomic Layer Deposition of Al₂O₃ and TiO₂ on MoS₂ Surfaces. *J. Vac. Sci. Technol. A* **2018**, 36 (6), 06A101. Reprinted with permission from J. Vac. Sci. Technol. A. Copyright 2018, American Vacuum Society.

5.1. Introduction

Two-dimensional semiconductors such as MoS₂ have attracted considerable interest in recent years due to their novel electronic properties. Comparable in structure to graphene²⁴ but with an indirect bandgap of ~1.29 eV in bulk form and a direct bandgap of ~1.8 eV in monolayer form,⁹ MoS₂ is a natural candidate for a channel material in thin-film field effect transistors (FETs). In fact, the fabrication and performance of devices derived from MoS₂, including but not limited to FETs, have been the subject of much study of late.^{6,7,31,33,40,74–80} One of the most important elements of many of these devices is a high-quality dielectric film on top of the semiconducting MoS₂ layer. Atomic layer deposition (ALD) is often used to deposit high-k dielectric films on MoS₂ for this purpose.^{31–33,39–41,43,44,74,76,78,79,81,82} However, the lack of dangling bonds on the MoS₂ surface results in poor reaction between the surface and the ALD precursors. This typically leads to incomplete surface coverage for dielectric films up to ~15 nm thick unless the surface is treated in some way before deposition,^{32,33,38–44,74,79,81,82} This presents a substantial problem for nanoelectronic devices, i.e. FETs where dielectric gate thicknesses below 10 nm are desired. To enable reliable production of MoS₂-based devices, a complete understanding of the ALD

process chemistry on the MoS₂ surface is required. However, due to the large variety of surface preparation techniques, it can be difficult to discern the exact reaction mechanisms.

Few-layer or monolayer MoS₂ may be prepared by mechanical exfoliation (the “Scotch tape” method) which itself has several variations,^{23,48,50} or synthesized by chemical vapor deposition (CVD).^{10–14} Both preparation methods create surfaces with a variety of defects.^{83–86} The presence of both defects and contamination from either the exfoliation process or the vapor deposition process can affect greatly the quality and reactivity of the starting MoS₂ surface. In ALD, the film nucleation step relies on the presence of suitable functional groups on the starting surface. As a result, the presence of contaminants on the surface that may either promote or inhibit film nucleation and growth may lead to erroneous conclusions about the effectiveness of any surface preparation approaches employed. Here, we investigate the high degree of variation found in both exfoliated and CVD-grown MoS₂ surfaces through characterization of ALD-grown dielectric films. We also compare ALD processes using alkyl and alkyl amine precursors.

5.2. Experimental

Molybdenum disulfide multilayers were exfoliated from a bulk crystal (SPI Supplies) using Scotch tape or semiconductor dicing tape (Semiconductor Equipment Corp.) and transferred to 300 nm SiO₂/Si substrates. Samples were annealed for 30 seconds on a 100°C hotplate prior to removal of the tape to improve the adhesion of MoS₂ to the substrate. This method was modified from the technique outlined by Huang et al.⁵⁰

Monolayer MoS₂ was grown on 280-300 nm SiO₂/Si substrates by Dr. Wenjuan Zhu, Yuhang Cai, and Zihan Yao at the University of Illinois Urbana Champaign (UIUC). The monolayers were grown using a CVD method. Molybdenum trioxide (MoO₃) powder (0.060g) and sulfur (S) powder (0.400g) were used as the precursors. The substrates were placed face down above the MoO₃ powder at the center of a tube furnace and heated to ~730°C while the S powder was placed upstream and heated to 200°C. The growth duration was ~5 minutes. Argon carrier gas was flowed at 490 sccm during the entire process. MoS₂ samples were imaged optically using a Nikon Digital Sight camera connected to a Nikon Optiphot-100 microscope. The Raman spectra were measured using an Horiba Raman Confocal Imaging Microscope by Dr. Zhu at UIUC.

Al₂O₃ and TiO₂ films were deposited on multilayer (exfoliated) and monolayer (CVD-grown) MoS₂ samples using trimethyl aluminum (TMA) and tetrakis dimethylamino titanium (TDMAT), respectively, as precursors with water as the oxidizer. Films were grown at 100-200°C in a custom-built ALD reactor described previously by Henegar and Gougousi.⁴⁵ Samples were heated for 30 minutes in the reactor to reach thermal equilibrium before the depositions began. The precursor (TMA or TDMAT) and water were introduced under 17 sccm nitrogen flow by short pulses, separated by a 30 second nitrogen purge. Film thickness and growth rates were measured using spectroscopic ellipsometry (JA Woollam α -SE) on companion native oxide Si(100) wafer pieces.

After the film deposition, MoS₂ samples were characterized via atomic force microscopy (AFM) using a Veeco Dimension 3100 AFM. AFM images were processed using the WSxM software package.⁸⁷ Film surface coverage was calculated from the

AFM images using the ImageJ software package⁸⁸ by first converting the images to 8-bit grayscale and then to binary images using the built-in Sauvola local thresholding algorithm that defines the threshold $T(x,y)$ as

$$T(x,y) = m(x,y) \times \left[1 + k \left(\frac{s(x,y)}{R} - 1 \right) \right] \quad (5.1)$$

where $m(x,y)$ is the local mean and $s(x,y)$ is the local standard deviation of the image.⁸⁹ The parameter R is the dynamic range of the standard deviation and was left at the default value of $R=128$. Images with low surface coverage were used to set the value for parameter k . A value of $k=0.3$ was found to produce the best match between the primary and binary image. Surface coverage was measured from the binary images. These values ($R=128$ and $k=0.3$) were used for all image quantification. Varying the k parameter by $\pm 33\%$ (from 0.2 to 0.4) results in changes of no greater than $\pm 5\%$ in measured surface coverage.

5.3. Results

5.3.1. Surface Preparation

CVD-grown MoS₂ flakes were characterized using optical microscopy (Figure 5.1a), Raman spectroscopy (Figure 5.1b), and AFM (Figure 5.1c,d). The optical image in Figure 5.1a shows the edge of a continuous MoS₂ region (left) and the presence of several isolated, triangular flakes with linear dimensions of $\sim 50 \mu\text{m}$. Typical flake sizes range from 10-50 μm . The spacing between the A_{1g} and E_{2g} Raman modes shown in Figure 5.1c is $\sim 18 \text{ cm}^{-1}$ which is indicative of monolayer MoS₂.^{90,91} Using AFM, the flake height (Figure 5.1c) is measured to be $\sim 0.7 \text{ nm}$ which is very near to the expected

thickness for a monolayer of MoS₂.^{5,83} The root mean square (RMS) roughness of the flake in Figure 5.1d is measured as 0.165 nm.

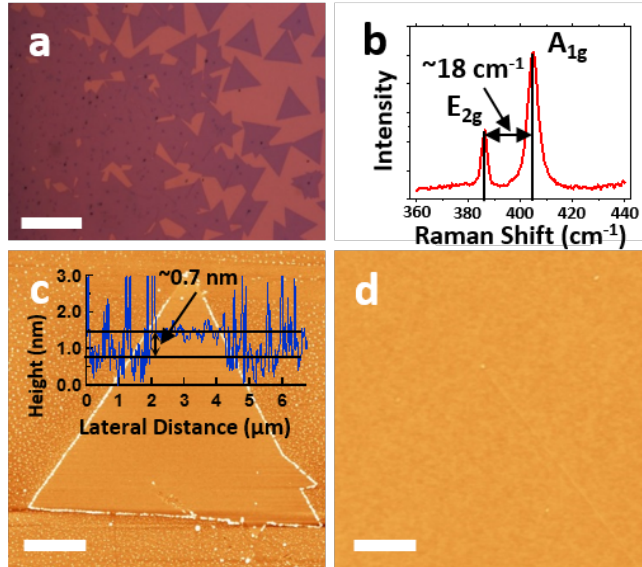


Figure 5.1. Characterization of CVD-grown MoS₂. (a) Optical micrograph of MoS₂ flakes on 300 nm SiO₂ substrate (scale bar 50 μm) and (b) Raman spectrum of the E_{2g} and A_{1g} modes of MoS₂. AFM images of a typical flake and its surface are shown in (c) (scale bar 2 μm) and (d) (scale bar 600 nm), respectively. The flake height was measured as ~0.7 nm in (c), and the RMS roughness from (d) was measured as 0.165 nm.

Mechanical exfoliation using adhesive tape is a relatively straightforward way to achieve large area (~25 μm²) few-layer MoS₂ flakes.^{48,50} The method entails removing layers of material from a bulk MoS₂ crystal with a piece of tape. Before transfer to a substrate, the tape-mounted MoS₂ may be thinned ~5-20 times with a clean piece of tape. The tape-mounted MoS₂ is then pressed to the substrate (usually SiO₂/Si) and rubbed with tweezers or another object to encourage van der Waals interactions between the MoS₂ and the SiO₂. The tape is carefully removed, leaving behind MoS₂ layers of varying size and thickness. While this method has been shown to produce large area, thin MoS₂ flakes, the tape can leave behind significant adhesive residue. Additionally, the exfoliated MoS₂ surfaces have been shown to contain a large number of defects, which are primarily sulfur vacancies.^{83,86} Typically, adhesive residues are

cleaned by soaking the samples in acetone for up to 8 hours.^{41,42,44,81} However, we found that long soaks in acetone can cause increased contamination of the MoS₂ surface. In Figure 5.2, an exfoliated sample has been imaged just after exfoliation with Scotch tape and again after several hours of soaking in acetone (Fisher Scientific, ACS grade). Each acetone soak was followed by a 1 minute rinse in acetone, methanol (Fisher Scientific, lab grade), and deionized water (Neu Ion).

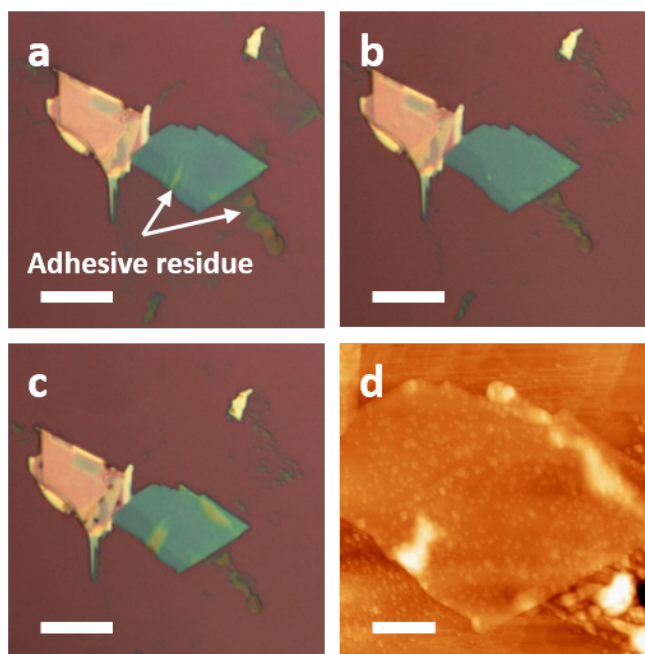


Figure 5.2. Optical micrographs of MoS₂ exfoliated with scotch tape and annealed for 120 s on a 100°C hotplate (a-c). The as-exfoliated flake is shown in (a) and the images taken after acetone soaks of 4 hours and 8 hours are shown in (b) and (c), respectively. In (d), an AFM image of the flake after an 8 hour acetone soak is shown. Scale bars are 10 μm in (a-c) and 3 μm in (d).

The adhesive leaves behind residue that appears bright yellow-green on the MoS₂ flake (blue-green) and on the Si substrate. After 4 hours in acetone, the amount of visible adhesive residue on the flake has decreased, but after a total of 8 hours, the contamination covers more of the MoS₂ surface than it initially had. AFM (Figure 5.2d) reveals that in addition to the bands of adhesive visible with optical imaging, there is the possibility of further surface contamination by adhesive

fragmentation/decomposition byproducts that may go undetected in the optical image. This series of data shows that the outcome of the acetone cleaning procedure is random; it may produce high quality surfaces, but it may also result in widespread contamination. As such, unless each flake is examined after the cleaning and prior to the deposition by AFM there is no certainty for the condition of the starting surface.

5.3.2. Atomic Layer Deposition of Al₂O₃

To investigate the variability in exfoliated MoS₂ surfaces obtained by different preparation methods, we performed 12 ALD cycles of Al₂O₃ at 100°C on dicing tape exfoliated and Scotch tape exfoliated MoS₂. The growth per cycle (GPC) for this process was measured to be 0.87 Å/cycle on Si/SiO₂ substrates and the expected film thickness was 1 nm. To study the effects of residual contamination caused by the exfoliation, the samples were not cleaned with acetone prior to ALD. To provide a control group, the same deposition was carried out on CVD-grown MoS₂, which is expected to provide more uniform starting surfaces. This low temperature was chosen to ensure that some surface coverage will be obtained. Films of this thickness were not expected to fully cover the surface and should provide insight into the effects of surface preparation on the nucleation mechanisms. The sample morphology after the depositions was investigated by AFM and a small selection of the data obtained is shown in Figure 5.3. AFM scans for each surface preparation were taken from different flakes on the same substrate.

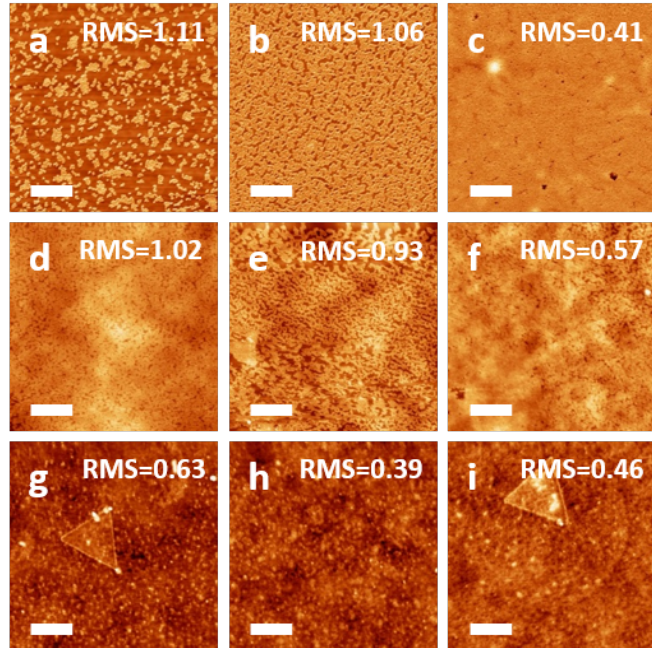


Figure 5.3. AFM images of 1 nm Al_2O_3 deposited at 100°C on dicing tape exfoliated MoS_2 (a-c), Scotch tape exfoliated MoS_2 (d-f), and CVD-grown MoS_2 (g-i). The scale bar is 600 nm for all images. For each surface preparation, images are taken from different flakes on the same substrate. RMS roughness values are given in units of nm.

Semiconductor dicing tape was used as an alternative to the standard Scotch tape since the lower tack of the adhesive is expected to provide cleaner transfers. For the samples prepared using the dicing tape (Figure 5.3a-c), a large variation in Al_2O_3 surface coverage is detected ranging from very low coverage (Figure 5.3a) to almost complete coverage (Figure 5.3c). The data shown in this figure were selected to illustrate the large variation in the deposition outcome. For the samples prepared using Scotch tape (Figure 5.3d-f) higher coverage was achieved, but the films are still not continuous. Many pinholes are visible in these films. For the depositions performed on the CVD flakes, the AFM data show that the film is just beginning to nucleate, with no coalescence of the islands formed. By contrast, the Al_2O_3 film deposited on the 300 nm SiO_2/Si substrate is completely coalesced and relatively smooth (Figure 5.10a) with an RMS roughness of 0.32 nm.

A quantitative estimate of the surface coverage for these samples is shown in Figure 5.4. The results for each exfoliation approach were taken from several flakes on the same SiO₂ substrate to ensure that each flake underwent identical preparation and processing. The control group of CVD MoS₂ flakes shows some scattering (16-37%) but the surface coverage is low as expected for a 1 nm film. The surfaces prepared using dicing tape yield samples with very large scattering in the surface coverage (25-98%) with more than half of the data points clustering above 80%. The data set obtained from the Scotch tape samples is smaller but also tends to cluster at the high (>70%) surface coverage region.

Subsequently the morphology of thicker films (35 cycles, ~ 3 nm) was examined, as such films are expected to be continuous and provide uniform surface coverage when grown on hydrophilic surfaces such as SiO₂ (Figure 5.10b). AFM images of 3 nm Al₂O₃ films deposited on CVD MoS₂ at 100°C are shown in Figure 5.5a-c, and while regions of dense film coalescence can be found in any single flake, the films are in general not continuous, with surface coverage ranging from 61-79% (Figure 5.4). We find that denser coverage is obtained at the center of the triangular flake and the coverage drops substantially closer to the flake edges. The CVD flakes were prepared on SiO₂ and Figure 5.5a shows the contrast in the behavior of the MoS₂ and the SiO₂ surface. The area surrounding the MoS₂ flake is covered with a fairly smooth layer of Al₂O₃. For a set of samples prepared on exfoliated flakes, higher surface coverage (90-99%, Figure 5.4) was measured, as expected from the results with the 1 nm films.

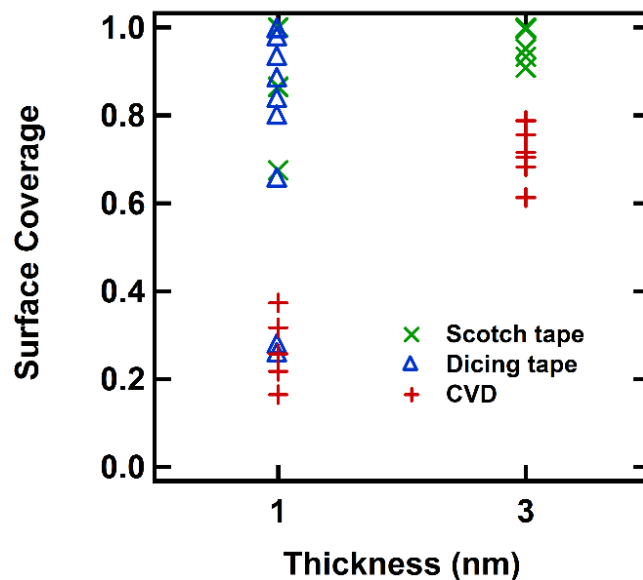


Figure 5.4. Calculated surface coverage for 1 and 3 nm Al₂O₃ films grown at 100°C on Scotch tape exfoliated, dicing tape exfoliated, and CVD-grown MoS₂ surfaces. Error bars are not included for clarity but the uncertainty for the surface coverage is estimated at ~5%.

To investigate the effect of temperature on the film nucleation, another set of 3 nm Al₂O₃ films (30 cycles, GPC 1.0 Å/cycle) was deposited on CVD MoS₂ flakes at 200°C and AFM data for a few of the samples are included in Figure 5.5d-f. AFM scans at each temperature were taken from different flakes on the same substrate. Comparing the data at the two temperatures, some variation in the surface coverage is observed. For both process temperatures the Al₂O₃ film preferentially grows in the center of the flake, avoiding the edge regions. The film coverage at 100°C ranges from 61-79%, while at 200°C the coverage ranges from 54-75% (Figure 5.11).

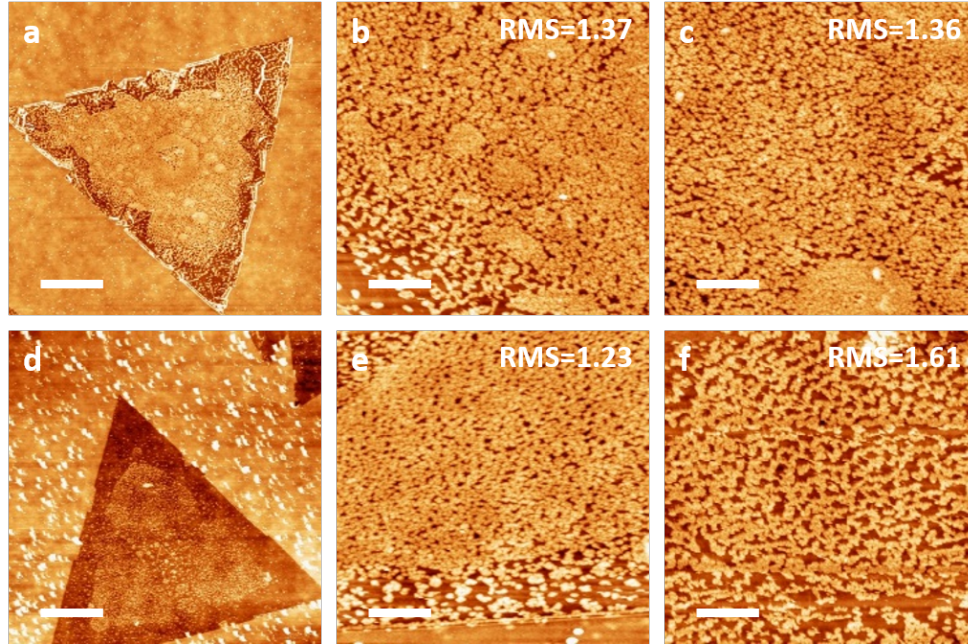


Figure 5.5. AFM images of 3 nm Al_2O_3 deposited on CVD-grown MoS_2 at 100°C (a-c) and 200°C (d-f). Scale bars are 3 μm (a,d) and 600 nm (b,c,e,f). RMS roughness values are given in units of nm.

While CVD-grown MoS_2 flakes offer a more controlled environment to study the nucleation of dielectrics during ALD process, they are not completely free of defects.^{12,84,86} Figure 5.6 includes some sample AFM data taken after the deposition of 3 nm of Al_2O_3 at 100°C. The film grows along grain boundaries (Figure 5.6a,b) and along the edges of a multilayered triangular region often found in the center of CVD-grown MoS_2 flakes (Figure 5.6b).

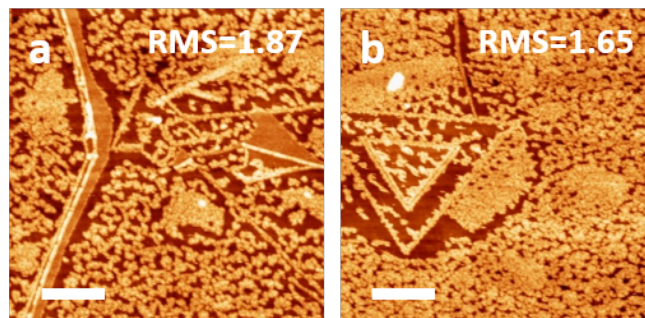


Figure 5.6. AFM images of 3 nm Al_2O_3 films grown on CVD MoS_2 at 100°C showing growth along defects (a) and multilayered step edges (b). Scale bars are 600 nm. RMS roughness values are given in units of nm.

5.3.3. Atomic Layer Deposition of TiO₂

TMA is a very aggressive alkyl precursor that reacts with a variety of surfaces even at temperatures below 100°C. Alkyl amine precursors are also used for a variety of ALD dielectric processes, so we chose to compare the reactivity and surface chemistry of the two precursor classes using the CVD-grown MoS₂ monolayer surfaces. For that purpose, we deposited TiO₂ films on CVD MoS₂ at 100-200°C using TDMAT and water. The ideal temperature for the TDMAT/H₂O ALD process in our reactor is 200°C with a nominal growth rate of 0.4 Å/cycle.⁹² At 100°C, the growth rate is 0.6 Å/cycle. The films were grown at thicknesses of 3 nm (50 or 75 cycles at 100°C or 200°C, respectively) and 6 nm (100 or 150 cycles at 100°C or 200°C, respectively). The surface coverage was calculated as before. Some sample AFM images of 3 and 6 nm TiO₂ films grown at both temperatures are shown in Figure 5.7 and Figure 5.8, respectively.

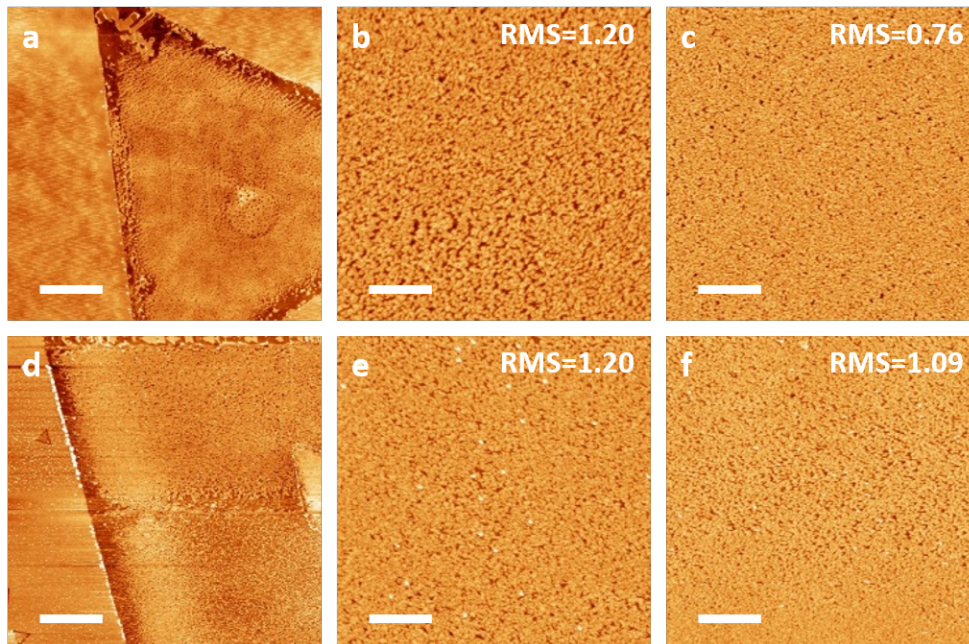


Figure 5.7. AFM images of 3 nm TiO₂ deposited on CVD-grown MoS₂ at 100°C (a-c) and 200°C (d-f). Scale bars are 2 μm (a,d) and 600 nm (b,c,e,f). RMS roughness values are given in units of nm.

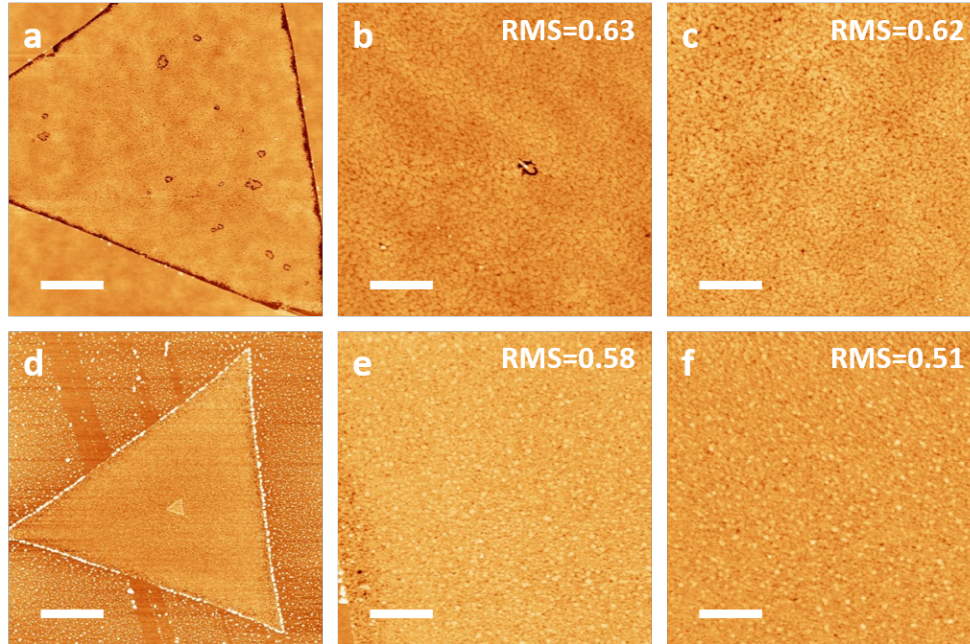


Figure 5.8. AFM images of 6 nm TiO₂ deposited on CVD-grown MoS₂ at 100°C (a-c) and 200°C (d-f). Scale bars are 2 μm (a,d) and 600 nm (b,c,e,f). RMS roughness values are given in units of nm.

AFM scans at a given temperature and thickness were taken from different flakes on the same substrate. Similar to the Al₂O₃ films, the TiO₂ films grow primarily in the center region, avoiding the flake edges. The films deposited at 100°C appear to have a connected network of voids while the films deposited at 200°C show more granular structure, with the RMS roughness decreasing marginally as the deposition temperature increases. However, even at 6 nm the film is not continuous, and many pinholes are visible at both deposition temperatures. The surface coverage calculations (Figure 5.9) show both an overall increase in coverage with film thickness, and, for 6 nm films, a slight overall increase in coverage with temperature.

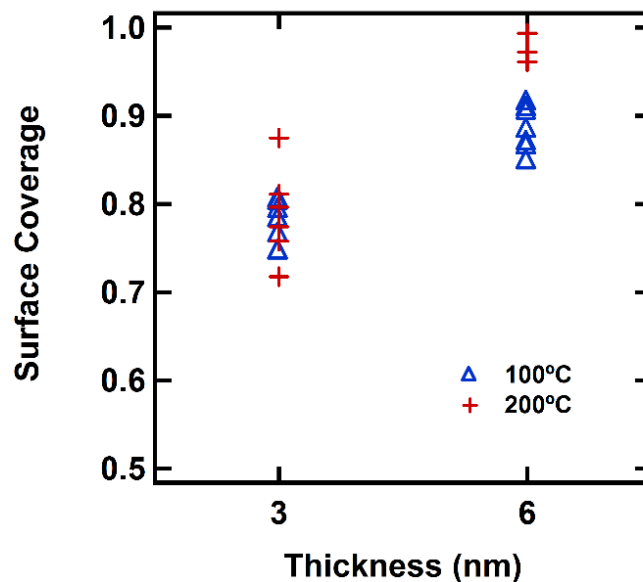


Figure 5.9. Calculated surface coverage of 3 nm and 6 nm TiO₂ deposited on CVD-grown MoS₂ at 100°C and 200°C. Error bars are not included for clarity but the uncertainty for the surface coverage is estimated at ~5%.

5.4. Discussion

5.4.1. Starting Surface Variability

Exfoliated MoS₂ flakes with and without further cleaning to remove residual adhesive have been used extensively in the literature. One of the most common cleaning approaches is an hours-long soak of the surfaces in acetone. When similar cleaning approaches were tested in this work, we found that long acetone soaks may redistribute the adhesive residue, resulting in surfaces covered with nanoscale debris (Figure 5.2d) that may not be visible optically. To study the effect of variations in residual contamination on the surface coverage from exfoliation alone, exfoliated samples were prepared and tested without any cleaning steps. For the deposition of 1 nm nominal thickness of Al₂O₃ on these surfaces, measured coverage ranged from as

little as ~25% to nearly complete surface coverage. As the samples were used without attempts to remove the residual adhesive from the exfoliation, this result can be attributed to the significant differences in the level of contamination from sample to sample. Previously, ~10 nm Al₂O₃ films were shown to grow uniformly on MoS₂.⁴¹ It has been suggested that this may be a result of the solvent-based cleaning steps performed after mechanical exfoliation.^{38,39} That, along with the data presented here, suggests that increased surface contamination may also contribute to the continuous growth of ALD films by serving as nucleation sites. Additionally, we observe some differences in the amount of scattering in the measured surface coverage between samples prepared by exfoliation using semiconductor dicing tape and those prepared using Scotch tape. The Scotch tape exfoliated samples exhibit greater surface coverage of 1 nm Al₂O₃ overall, suggesting that the average level of contamination is higher than that on dicing tape prepared samples where very low film coverage (25%) has been observed. The scattering in the surface coverage on the dicing tape exfoliated surfaces is large (25-98%) indicating that, while relatively clean surfaces may be obtained through this method, its reliability is poor.

In addition to the possible presence of residual adhesive, mechanically exfoliated MoS₂ exhibits surface defects (mainly sulfur vacancies) at concentrations between 0.1-10%.^{83,86} Density functional theory calculations have shown that dissociation of molecular oxygen can occur at sulfur vacancies, allowing atomic oxygen to adsorb on the vacancy site.⁹³ TMA is a known oxygen scavenger and we expect that the oxygen-filled vacancies may react more readily with TMA and seed the film growth. The combination of the presence of surface contamination and a large concentration

of sulfur vacancies may explain the very high surface coverage obtained for the deposition of 1 nm of Al₂O₃ on the exfoliated samples (Figure 5.4). By comparison, when 1 nm of Al₂O₃ was deposited at 100°C on CVD-grown MoS₂, the surface coverage was significantly lower with less scattering. While these CVD-grown samples are not free of defects, the initial surface condition is more reproducible and these surfaces present the opportunity to study the ALD process surface chemistry in a more controlled setting.

5.4.2. Al₂O₃ and TiO₂ Films on CVD-grown MoS₂

ALD of Al₂O₃ films on MoS₂ has been shown previously to be dominated by precursor physisorption and therefore surface coverage is expected to decrease with deposition temperature.^{38,41,81} This temperature dependence was previously explained by Park et al. using the Langmuir adsorption model,⁸¹ where the desorption of precursor molecules from the surface depends on the substrate temperature (T) and the desorption energy (E_{des}). Park et al. state that the uncovered fraction of the surface is proportional to $\exp(-E_{des}/k_B T)$. Assuming no chemisorption, the adsorption energy of precursor molecules (E_{ads}) is approximately equal to E_{des}, so the initial surface coverage in the limit of pure physisorption depends only on E_{ads} of the precursor and the substrate temperature. In this work, 3 nm Al₂O₃ films deposited on CVD-grown MoS₂ at 100°C have surface coverage from 61-79% with an average coverage of 71% (Figure 5.4) while analogous films deposited at 200°C have surface coverage from 54-75% (average 66%, Figure 5.11). Elevated deposition temperature leads to marginally reduced surface coverage as expected by the simple Langmuir model. However, the scattering in the data is such that no conclusion about the degree of contribution of this mechanism

can be made. CVD-grown MoS₂ surfaces are free from organic adhesive but they may have some residual surface variation from the presence of the species used in the growth. These surfaces also contain defect sites as well as grain boundaries.^{12,84,86} The scatter in the data is presumed to originate from such non-ideal starting surfaces as shown in Figure 5.6. These factors are not accounted for in the simple Langmuir adsorption model described above. The high variability in surface coverage indicates that temperature-dependent physisorption is not as important as the quality of the starting surface. Since common defects such as sulfur vacancies are easily passivated with oxygen,⁹³ these sites react readily with the ALD precursors and seed the film growth.

To study the effects of precursor choice on film growth, we deposited TiO₂ films on CVD MoS₂ using TDMAT and water. TDMAT is an alkyl amine precursor and thus this process is representative of ALD processes using similar alkyl amine precursors. Several dielectric materials of interest in nanoelectronics can be grown with such precursors, including HfO₂ and ZrO₂.⁴⁶ TiO₂ films were grown at a nominal thickness of 3 nm at both 100°C and 200°C. Film growth was expected to be dominated by precursor physisorption and thus the surface coverage should decrease as temperature increases. However, at both temperatures the average TiO₂ surface coverage is ~78%. The lack of any clear temperature dependence suggests that there are competing mechanisms during the growth of TiO₂ on MoS₂. The average surface coverage of TiO₂ films is slightly higher than that of Al₂O₃ by ~8-12%, though the range of coverage does overlap. It is therefore difficult to discern any precursor-dependent effects from surface coverage measurements alone. It is possible that there are some differences in

the initial reaction of TMA/TDMAT with the MoS₂ surface. The AFM images in Figure 5.5e-f, for example, show Al₂O₃ films with large gaps, while the TiO₂ films in Figure 5.7e-f are visibly different, with smaller gaps between coalesced islands.

Deeper insight into the growth mechanics of TiO₂ on MoS₂ can be gained from the deposition of the thicker 6 nm TiO₂ films grown at 100°C and 200°C. The surface coverage for these films increases as a function of temperature (Figure 5.9), defying the Langmuir adsorption model. The increased surface coverage at elevated temperature suggests that at 200°C the reaction between TDMAT and MoS₂ is thermally activated. Diffusion is also thermally activated, and an increase in the surface temperature may result in enhanced diffusion of the TDMAT molecules on the surface before finding a favorable bonding site (i.e. a defect or -OH terminated site). Since bonding to edge sites is energetically favorable compared to bonding to terrace sites, enhanced diffusion should result in smoother films and increased surface coverage which is observed for the films deposited at 200°C (Figure 5.8e,f). Additionally, Figure 5.8d shows that the TiO₂ film has grown nearly to the edge of the MoS₂ flake, in contrast to the flake in Figure 5.8a, where the film has not migrated to the flake edge. The fact that TiO₂ film coverage increases with temperature further suggests differences between the reactions of TMA and TDMAT with MoS₂. However, elucidation of the exact differences in TMA/TDMAT reactions with the MoS₂ surface requires further study.

Though the TDMAT/H₂O process yields slightly better film coverage than the TMA/H₂O process on monolayer MoS₂, the TiO₂ films are not completely uniform or pinhole-free even at a thickness of 6 nm. It is, of course, well known that ALD films

of Al₂O₃ or HfO₂ on MoS₂ below ~15 nm in thickness rarely achieve complete, uniform surface coverage without some kind of surface treatment or special deposition conditions.^{32,33,38–44,79,81,82} This is in contrast to ALD of metal oxides on other hydrophobic surfaces, namely H-terminated silicon. ALD of HfO₂ on H-terminated Si using tetrakis dimethylamino hafnium (TDMAH) and H₂O was found to have a growth barrier for approximately the first four ALD cycles.⁹⁴ After 25 cycles, however, the HfO₂ film is continuous with a ~10 Å interfacial SiO₂ layer between the Si substrate and the HfO₂ film. The formation of this SiO₂ interfacial layer provides the necessary OH surface groups to allow for proper HfO₂ film nucleation. The lack of ability of the MoS₂ basal plane to oxidize readily (except at defect sites) means that no interfacial layer is formed during ALD, and substrate-inhibited growth occurs up to 100 ALD cycles or more.

5.5. Conclusions

We have studied the ALD of Al₂O₃ on mechanically exfoliated and CVD-grown MoS₂ and the ALD of TiO₂ on CVD-grown MoS₂. There is a high degree of variability in the surface coverage of Al₂O₃ films on exfoliated MoS₂ surfaces due to variations in the starting surfaces, likely caused by residual contamination and defects. CVD-grown MoS₂ shows less variation and thus more reproducible surfaces for the study of the ALD process chemistry. We find that neither Al₂O₃ nor TiO₂ films strongly follow the temperature dependence described by Langmuir adsorption; however, morphological differences between Al₂O₃ and TiO₂ films point to differences in the underlying surface reaction between TMA/MoS₂ and TDMAT/MoS₂.

5.6. Supplemental Information

5.6.1. AFM images of Al₂O₃ on silicon

Figure 5.10 shows AFM scans of ALD-grown Al₂O₃ films deposited on either 300 nm SiO₂ or native oxide silicon wafers. These films are continuous and smooth, with the RMS roughness affected mainly by the underlying substrate (300 nm SiO₂ wafers are expected to be rougher than native oxide wafers).

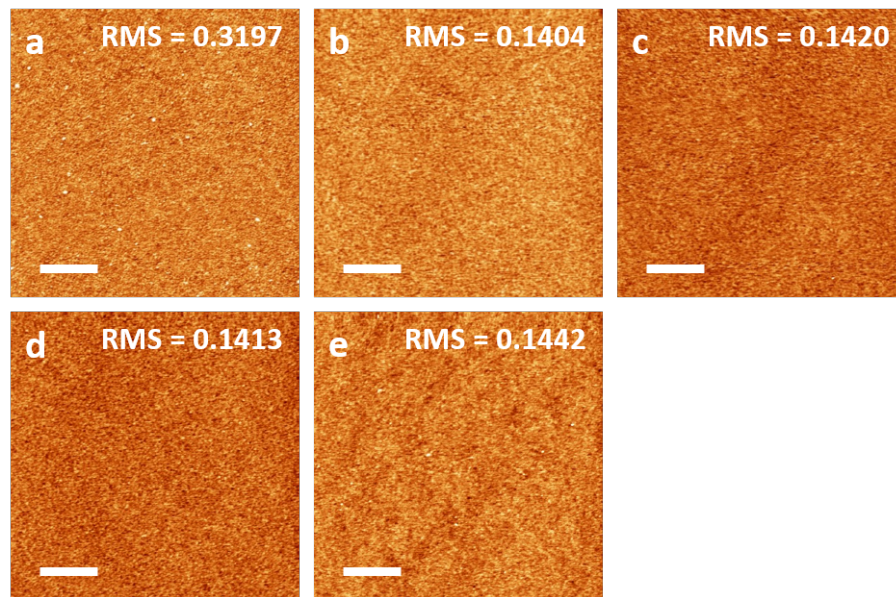


Figure 5.10. (a) 1 nm Al₂O₃ on 300 nm SiO₂ at 100°C. Also shown are 3 nm Al₂O₃ at (b) 100°C and (c) 200°C on native oxide Si. TiO₂ at 100°C shown for thicknesses of (d) 3 nm and (e) 6 nm at 100°C on native oxide Si. Scale bars are 600 nm.

5.6.2. Al₂O₃ films on MoS₂

Figure 5.11 plots the surface coverage of Al₂O₃ films deposited on CVD-grown MoS₂ at 200°C. As expected, the surface coverage increases with film thickness. The

average coverage for 1 nm films is 37% and the average coverage for 3 nm films is 66%. Figure 5.12 shows the AFM scans of 1 nm Al_2O_3 films on CVD-grown MoS_2 .

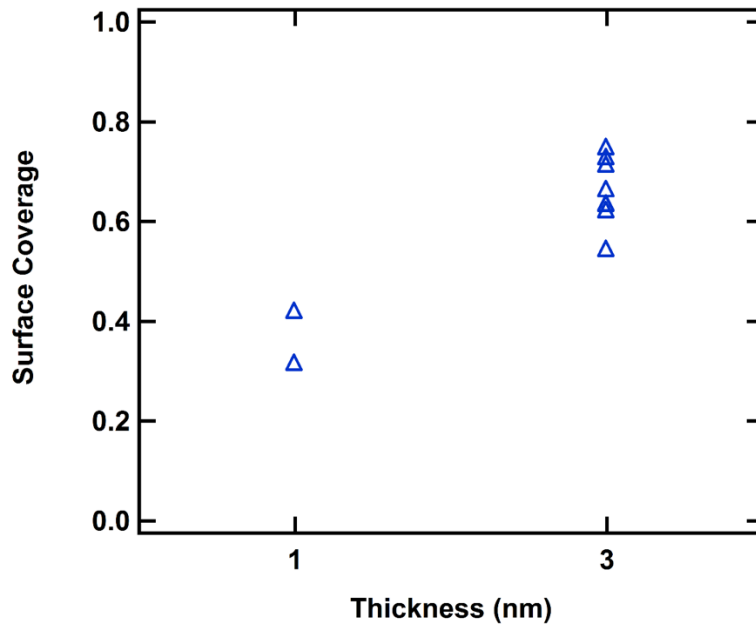


Figure 5.11. Surface coverage of Al_2O_3 on CVD-grown MoS_2 at 200°C.

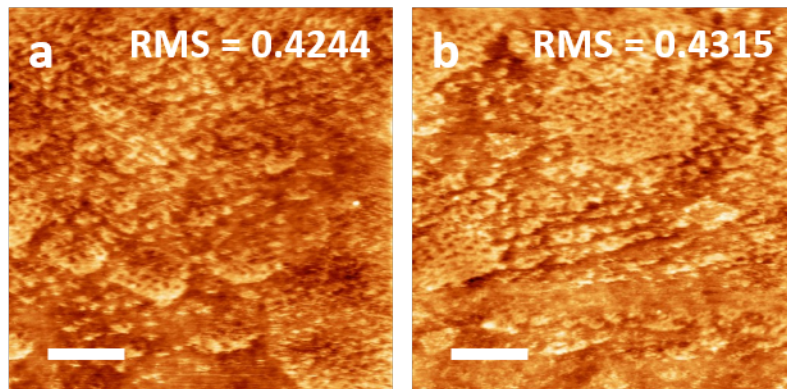


Figure 5.12. (a), (b) AFM scans of 1 nm Al_2O_3 deposited on CVD-grown MoS_2 at 200°C.

Chapter 6. Surface Defect Engineering of MoS₂ for Atomic Layer Deposition of TiO₂ Films

6.1. Introduction

Monolayer molybdenum disulfide (MoS₂) is a two-dimensional (2D) semiconductor material that primarily exists in a hexagonal structure (2H-MoS₂). Monolayer 2H-MoS₂ possesses a direct band gap of ~1.8 eV and is therefore of interest for electronic, optoelectronic, and sensing applications.^{9,95} Recently, chemical vapor deposition (CVD) methods have been developed to grow high quality, large-area single crystal MoS₂ monolayers.¹⁰⁻¹⁴ If these MoS₂ monolayers are to be used in a device such as a field-effect transistor, they need to be integrated with a high quality dielectric material. Atomic layer deposition (ALD) has been used extensively to deposit high-k dielectric films on mainstream semiconductors due to the high film quality, purity and the ability to coat non-planar geometries. For ALD of metal oxide films, a hydrophilic surface is required. The MoS₂ surface, however, is inert and hydrophobic. ALD of metal oxides on inert, hydrophobic surfaces such as hydrogen-terminated Si (Si-H) has been studied extensively, and in general it is known that film formation occurs on defect sites on these materials. The Si-H surface is unstable at normal processing temperatures leading to the progressive increase of the defect density and eventually the formation of continuous films after what is known as an incubation period.⁹⁴ Like Si-H, the MoS₂ surface is inert and hydrophobic, but unlike Si-H it is stable at normal processing temperatures and as a result not an ideal starting surface for the ALD of metal oxide films. However, even exfoliated MoS₂ surfaces contain up to ~10% sulfur vacancies which can be used as nucleation sites.⁸³ Still, deposition on such surfaces results in the

formation of non-continuous films even for films several nanometers in thickness. Surface treatments that alter the surface energy or special deposition conditions have been used to achieve uniform, pinhole-free films on MoS₂.^{32,38,40,42,44,96–99} Thiols are known to interact with the naturally occurring vacancies and may be used to functionalize the MoS₂ surface.^{58,59,100–111} Since the density of such naturally occurring vacancies is low, additional sulfur vacancies can be created via ion beam irradiation.^{58–60,112} To date, however, thiol functionalization has not been used to promote ALD film growth.

In this work, we investigate the effect of defect density on the surface coverage obtained for a typical ALD process by using Ar ion sputtering to control their density. Additionally, we examine the effectiveness of a mercaptoethanol interlayer as a seed layer for the ALD of TiO₂ both on as-received and argon ion-treated CVD MoS₂ surfaces. Mercaptoethanol (HOCH₂CH₂SH) is a short thiol with an -SH group at the tail and is hydroxyl terminated on its other end. Several previous studies have shown that thiols are likely to interact with sulfur vacancies on the MoS₂ surface.^{58,59,100–104,106–108} Since ME molecules do not interact strongly with the pristine surface, the surface density of defect sites is critical to the surface reactivity and the overall film quality achieved. The CVD-grown MoS₂ surfaces do not contain sufficiently high defect density, so it is desirable to find a method to enhance and control this as desired. It has been shown previously that sputtering the surface of MoS₂ with low-energy (~500 eV) argon ions selectively removes sulfur atoms to create single sulfur vacancies.^{58–60} It is expected that the -SH group will interact with the MoS₂ surface via the defect sites which will leave the -OH group at the other end available for interaction with the

precursor, as in a typical metal oxide ALD process. The experimental work is complemented by calculations of the energetics of thiol and ALD precursor adsorption on pristine and vacancy-containing MoS₂ surfaces using density functional theory. This combined approach provides significant insight into the mechanism of ALD film growth on MoS₂.

6.2. Experimental Methods

Monolayer MoS₂ samples were grown by Dr. Wenjuan Zhu and Ankit Sharma at UIUC. Monolayer MoS₂ is grown on 280 nm Si/SiO₂ substrates via CVD using solid precursors. Molybdenum trioxide (MoO₃) and sulfur (S) powder are placed into a 3" 3-zone tube furnace in a 1:8 ratio. The substrates are suspended face-down above 0.05g MoO₃ using a quartz stage and placed in the center zone of the furnace. The S powder is placed in the upstream zone. The growth is conducted at atmospheric pressure, but prior to beginning the temperature ramp, 500 sccm of argon is flowed as a carrier gas. The center zone is heated to 730 °C and the upstream zone is heated to 200 °C during the growth process ramp phase. The growth lasts for ~10 min. After the growth, the furnace is allowed to naturally cool to 50 °C prior to retrieving samples. Samples are examined using an optical microscope and under a Horiba Raman Confocal Imaging Microscope by Dr. Zhu to confirm the presence of monolayer MoS₂.

ALD of TiO₂ films is performed at 100°C using tetrakis dimethylamino titanium (TDMAT) and water as precursors. The deposition is performed in a custom-built ALD reactor previously described by Henegar and Gougousi.⁴⁵ Both precursors are introduced by short pulses under nitrogen flow. TDMAT and water pulses are separated by a 30 s nitrogen purge. The deposition consists of 100 ALD cycles for a nominal film

thickness of 6 nm. After ALD, the TiO₂ film morphologies are analyzed via atomic force microscopy (AFM) using a Veeco Dimension 3100 AFM. The AFM images are processed using the WSXM software package.⁸⁷

Mercaptoethanol (SHCH₂CH₂OH) treatment of MoS₂ samples is performed by fixing the samples to the underside of the cap of a vial containing 200 μL of pure mercaptoethanol liquid. The vials are sealed and left at room temperature for 3 hours. This thiol treatment is performed in a glove box under nitrogen atmosphere to avoid atmospheric contamination.

The MoS₂ samples are sputtered at an accelerating voltage of 700 V, and XPS data are taken *in situ* to monitor the sulfur concentration. Argon ion sputtering is performed under high vacuum at an accelerating voltage of 700 eV for 60-390 s using a Physical Electronics 04-303 differentially pumped ion gun. Sputtering was performed by Dr. Karen Gaskell at the University of Maryland, College Park. The sputter current is measured as ~100 nA. The ion fluence is calculated as $F = It/qA$, where I is the sputter current, t is the sputtering time, q is the elementary electron charge, and A is the area of sputtering. X-ray photoelectron spectroscopy (XPS) data are taken *in situ* using a Kratos AXIS 165 spectrometer with an Al monochromatic x-ray source (1486.6 eV). The resulting spectra are shifted to the C 1s peak at 284.8 eV, and the S:Mo ratios R are calculated by fitting the integrated peak areas of the S 2p and Mo 3d peaks, $A(S\ 2p)$ and $A(Mo\ 3d)$, respectively, as

$$R = \frac{A(S\ 2p)}{A(Mo\ 3d)} \quad (6.1)$$

The peak areas are corrected for the difference in relative sensitivity factor. This ratio is used to find the fraction of sulfur vacancies V_s as

$$V_s = 1 - R/2 \quad (6.2)$$

After sputtering, samples are removed from the XPS chamber under nitrogen atmosphere and sealed in vials to prevent air exposure. The vials are transferred to a nitrogen-filled glove box where select samples are treated with mercaptoethanol as described previously. The vials are resealed under N₂ atmosphere and left for 3 hours. After removal from the vials, the MoS₂ samples are transferred immediately to the ALD reactor. A control set of samples is prepared in the same manner, but without the thiol vapor treatment.

6.3. Computational Methods

DFT calculations are performed using the Vienna Ab initio Simulation Package (VASP).⁷³ Calculations are carried out within the generalized gradient approximation (GGA) of Perdew-Burke-Ernzerhof (PBE).⁶⁶ A cutoff energy of 520 eV and total energy convergence of 10⁻⁵ eV is used for all calculations. Sulfur vacancy concentrations are adjusted by placing a single vacancy in a 2×2×1, 3×3×1, or 4×4×1 supercell corresponding to vacancy concentrations of 12.5%, 5.5%, and 3%, respectively. K-points are generated in a gamma-centered mesh of 9×9×1, 6×6×1, or 5×5×1 for the 2×2×1, 3×3×1, or 4×4×1 supercells, respectively. All calculations include spin polarization effects. Calculations of the adsorption energy of molecules on the MoS₂ surface are performed by placing the molecule ~2 Å above the MoS₂ layer and allowing the system to relax. The adsorption energy of a molecule on the surface or sulfur vacancy is calculated as

$$E_{ads} = E(Mol + MoS_2) - E(Mol) - E(MoS_2) \quad (6.3)$$

where $E(\text{Mol}+\text{MoS}_2)$ is the total energy of the combined system, $E(\text{Mol})$ is the total energy of the isolated molecule, and $E(\text{MoS}_2)$ is the total energy of the isolated MoS₂ layer. The energy barrier for ME, H₂O, or O₂ molecules binding to a sulfur double vacancy in MoS₂ is calculated by fixing the molecule between 3 Å and 0 Å above the surface at 0.5 Å intervals. At each interval, only one atom in the ME molecule was fixed and all other atoms are allowed to relax fully, except for one Mo atom in the MoS₂ layer which is fixed to prevent overall translation of the structure. When the molecule is placed in the vacancy, all atoms are allowed to relax.

Ab initio molecular dynamics (AIMD) simulations are performed using VASP to determine the dynamical stability of several molecule-MoS₂ systems. The simulations are performed at a temperature of 600 K with a timestep of 0.5 fs and run for 2000 steps (1 ps total).

The cluster expansion method implemented using the Alloy Theoretic Automated Toolkit (ATAT)¹¹³ is used to generate MoS₂ structures containing sulfur vacancies in concentrations from 10-20 percent. The results from the cluster expansion are used to find the most energetically favorable vacancy-containing structures at the desired concentrations.

6.4. Results

6.4.1. Atomic Layer Deposition of TiO₂ on MoS₂

Deposition of TiO₂ films on untreated MoS₂ monolayers results in non-continuous films that contain many pinholes. As an example, Figure 6.1a,b shows AFM images of 6 nm TiO₂ deposited on MoS₂ at 100°C. AFM line profiles measure the depth of the

pinholes as 6 nm. Depositions of 6 nm films on ME treated surfaces (Figure 6.1c,d) show similar behavior. In fact, the films contain larger pinholes and on average show decreased surface coverage than films on the untreated surfaces.

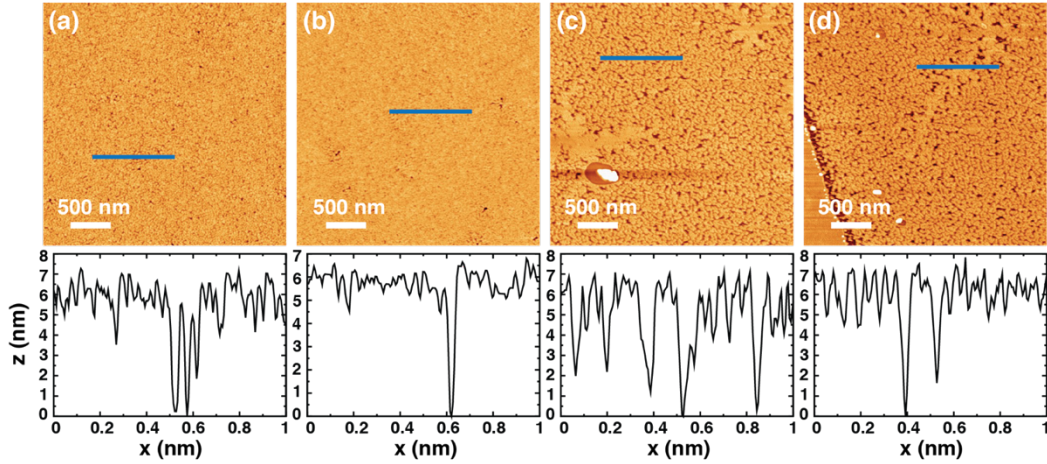


Figure 6.1. AFM images of ALD of 6 nm TiO₂ on (a,b) untreated MoS₂ and (c,d) MoS₂ treated with mercaptoethanol. Blue bars mark the location of line profiles shown below each image.

Because thiol atoms should primarily adsorb to sulfur vacancies on the MoS₂ surface, we sputter the MoS₂ monolayers with the aim of creating a high concentration of reactive sites before exposing the monolayers to thiol vapor. Analysis of the XPS results show that the as-grown CVD MoS₂ surface contains ~5% vacancy sites, which includes possible defects present on both sides of the monolayer. The evolution of the surface defect density as a function of sputter time and ion fluence is shown in Figure 6.2. Sputtering for 390 s (corresponding to an ion fluence of $F = 4.97 \times 10^{14} \text{ cm}^{-2}$) generates up to 20% sulfur vacancies. The shortest sputter duration, 30 s ($F = 3.83 \times 10^{13} \text{ cm}^{-2}$), generates ~8.5% sulfur vacancies. It is expected that the vacancies generated by sputtering are on the top side of the MoS₂ surface only.

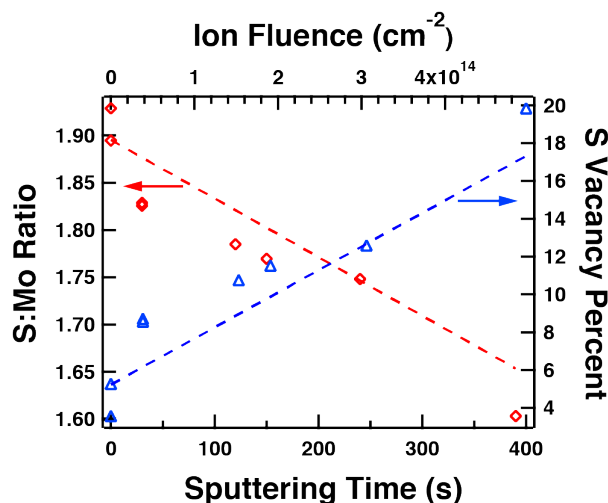


Figure 6.2. The left axis (red line) plots the sulfur:molybdenum ratio of MoS₂ as a function of sputter time (ion fluence) as calculated from XPS peak fitting. The right axis (blue line) plots the calculated sulfur vacancy percentage as a function of sputter time (ion fluence).

Ion bombardment is a highly invasive surface treatment, so it is important to consider its effect on the surface structure. Argon plasma has been shown to induce a phase change in MoS₂, and the change from the 2H phase to the 1T phase is detectable with XPS analysis.¹¹⁴ High resolution XP spectra of the Mo 3d and S 2p regions (Figure 6.3) taken before and after ion sputtering show little change in peak shape. This confirms that the treatment did not induce phase changes or destroy the MoS₂ layer, but preferentially creates sulfur vacancies on an otherwise intact 2H-MoS₂ surface.

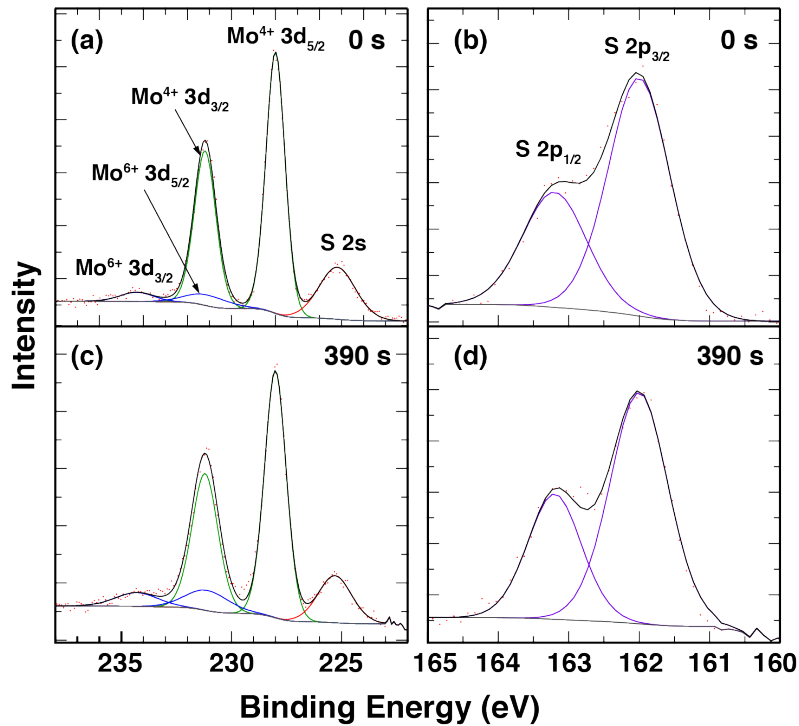


Figure 6.3. X-ray photoelectron spectra of the (a) Mo 3d region (no sputtering) and (b) S 2p region (no sputtering), and the (c) Mo 3d region (390s sputtering) and (d) S 2p region (390s sputtering).

The sputtered MoS₂ samples (up to 390s~20% S vacancies) are treated with mercaptoethanol vapor before subsequent ALD of 6 nm TiO₂. As a control, we also perform ALD on sputtered samples with no thiol treatment. After deposition, the films are analyzed via AFM. The characterization of the surface morphology of TiO₂ films on sputtered, ME-treated MoS₂ samples reveals films that are uniform and pinhole-free (Figure 6.4a-c). TiO₂ films on the control MoS₂ samples are similarly uniform and free of pinholes (Figure 6.4d-f). This suggests that the increased concentration of sulfur vacancies alone, as compared to as-grown CVD MoS₂, is sufficient to promote smooth, conformal, and coalesced ALD film growth. Both sets of samples exhibit dendritic structures on the surface that are ~1 nm in height. Similar features have been observed in thermally oxidized MoS₂, and it is possible that these dendrites are formed by oxidation of the defective MoS₂ layer.¹¹⁵

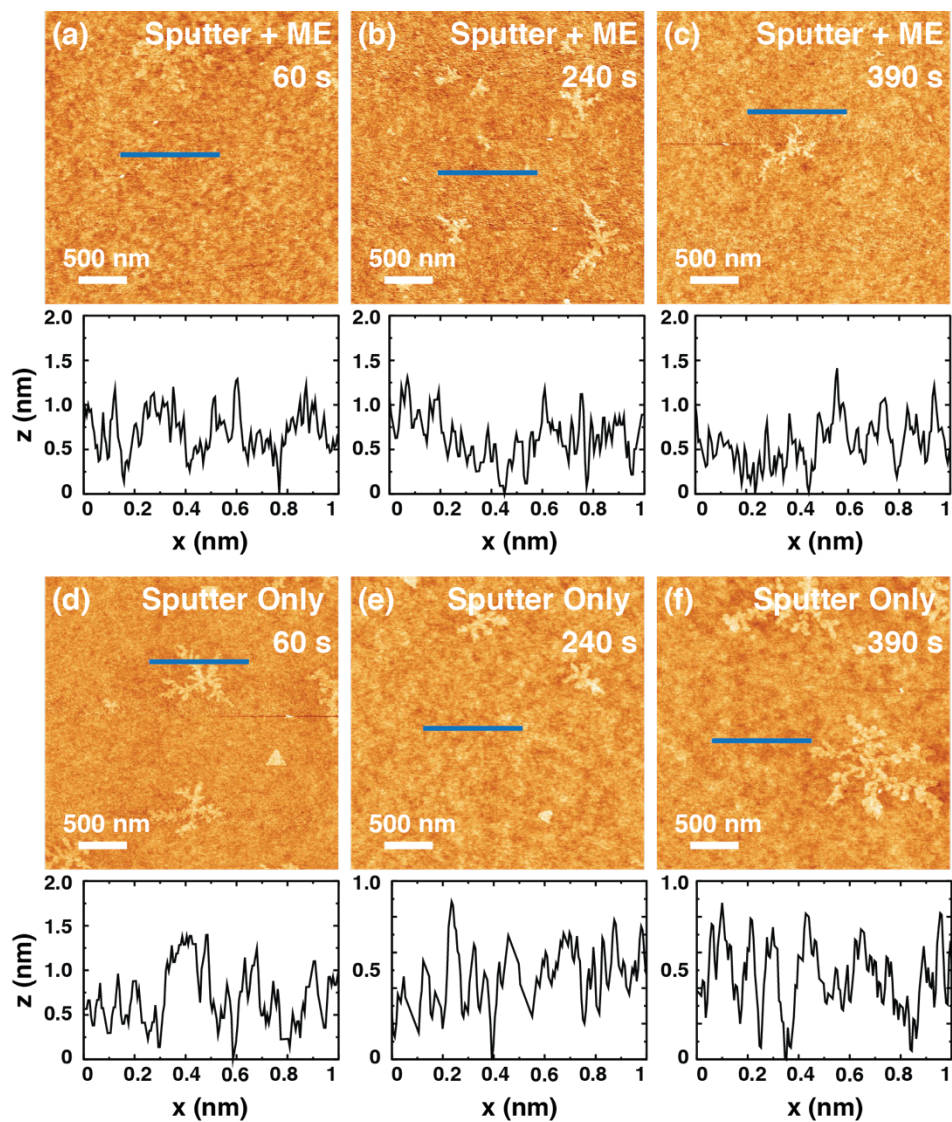


Figure 6.4. AFM images of 6 nm TiO_2 deposited on ME-treated MoS_2 that was sputtered for (a) 60 s, (b), 240 s, and (c) 390 s. Also shown are AFM images of 6 nm TiO_2 deposited on MoS_2 that was sputtered for (d) 60 s, (e) 240 s, and (f) 390 s with no ME treatment. Blue bars mark the location of line profiles shown below each image.

6.4.2. First-Principles Calculations

To understand better the energetics of the ME- MoS_2 interaction, we employ DFT to study the adsorption of ME molecules at several sites on the MoS_2 surface: the top S, top Mo, bridge, and hollow sites (Figure 6.5a). The calculated adsorption energies

for each site are reported in Table 6.1. The adsorption energy of the ME molecule in a $4 \times 4 \times 1$ supercell (corresponding to a thiol density of $7.09 \times 10^{13} \text{ cm}^{-2}$) ranges from -0.15 to -0.18 eV. The adsorption energy of ME on top of the sulfur vacancy is -0.27 eV, indicating that this is a more favorable adsorption site. We also calculate the adsorption energy after placing the ME molecule in the S vacancy. This geometry results in an adsorption energy of -0.25 eV. The final geometries for the ME molecule adsorbed on top of and inside the S vacancy are shown in Figure 6.5b and c, respectively.

Table 6.1. Calculated adsorption energies of mercaptoethanol on MoS₂ in a $4 \times 4 \times 1$ supercell for both pristine MoS₂ and S-vacancy-containing MoS₂.

Site	E_{ads} (eV) Pristine	E_{ads} (eV) S vacancy
Top S	-0.15	-0.27
Top Mo	-0.18	-
Bridge	-0.14	-
Hollow	-0.17	-

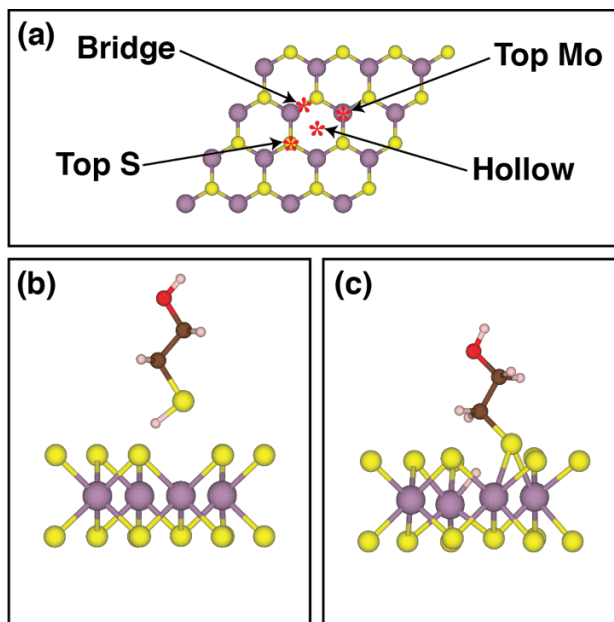


Figure 6.5. (a) The adsorption sites studied for mercaptoethanol. (b) The relaxed geometric structure of the ME molecule adsorbed above the S vacancy. (c) The relaxed geometric structure of the ME molecule adsorbed in the S vacancy. The atoms are: Mo (purple), S (yellow), O (red), C (brown), and H (white).

Motivated by the observation of uniform film growth on the 10-20% vacancy-containing MoS₂, we also calculate the adsorption energy of O₂, H₂O, and TDMAT molecules on the S vacancy site. We consider O₂ and H₂O molecules as possible seed molecules for TiO₂ film growth, as they are abundant in air and may react with TDMAT to form TiO₂.^{116,117} The final geometry and adsorption energy for these molecules on the S vacancy are shown in Figure 6.6. The adsorption energy of TDMAT on MoS₂ is calculated in a 6×6×1 supercell to avoid interactions between the relatively large TDMAT molecule and its periodic images. In agreement with previous works, we find that O₂ and H₂O adsorb weakly above the S vacancy.^{118,119} The adsorption energies of -0.09 eV and -0.15 eV for O₂ and H₂O, respectively. TDMAT binds most strongly of all molecules considered here, with adsorption energy of -0.43 eV. On the pristine MoS₂ surface, TDMAT adsorbs with an energy of -0.23 eV.

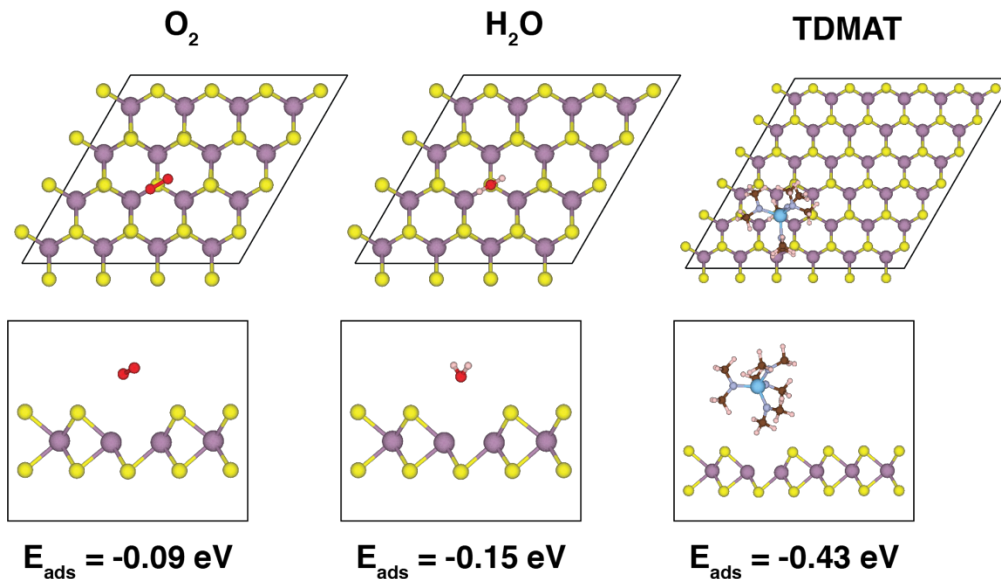


Figure 6.6. Adsorption geometry and energy of O₂, H₂O, and TDMAT on a single S vacancy. The atoms shown in the figure are: Mo (purple), S (yellow), O (red), C (brown), H (white), N (pale blue), and Ti (bright blue).

Because of the high concentration of defects on our sputtered MoS₂ surfaces, it is likely that extended defects are present. Cluster expansion is used to generate structures with the desired sulfur vacancy concentration (10-20 percent) and identify the most favorable arrangement of such vacancies. Our cluster expansion calculations reveal that extended line defects are favorable at these defect concentrations. As calculations of molecule adsorption on structures containing line defects are computationally demanding, we perform a calculation of ME adsorption on both an extended line defect and a simpler double sulfur vacancy. The adsorption energies of ME on these structures are similar, with $E_{ads} = -2.66$ eV (line vacancy) and $E_{ads} = -2.43$ eV (double vacancy) so we can use the double vacancy as a proxy for more extended defects. To study the interaction of other molecules with such defects, we calculate the adsorption energy of O₂, H₂O, and TDMAT on top of a double sulfur vacancy (two adjacent vacancies). The adsorption energy of TDMAT on the double vacancy does not change significantly, with a value of -0.45 eV. The adsorption energies of O₂ and H₂O on top of the double vacancy are likewise unchanged (calculated as -0.08 eV and -0.15 eV, respectively). ME can overcome an energy barrier of ~0.09 eV to chemisorb inside the vacancy with a adsorption energy of -2.43 eV (Figure 6.7). In this situation, the S-H bond is broken, and the thiol chain passivates one sulfur vacancy site while the H atom bonds in the neighboring site. The thiol remains chemisorbed in the vacancy after 4 ps of AIMD simulations at 600 K, indicating that this system is dynamically stable. Similar calculations indicate that the energy barrier for an O₂ atom to chemisorb in the double vacancy is ~0.1 eV and the resulting adsorption energy is $E_{ads} = -2.30$ eV. The H₂O molecule does not chemisorb in the vacancy, but remains physisorbed on the surface.

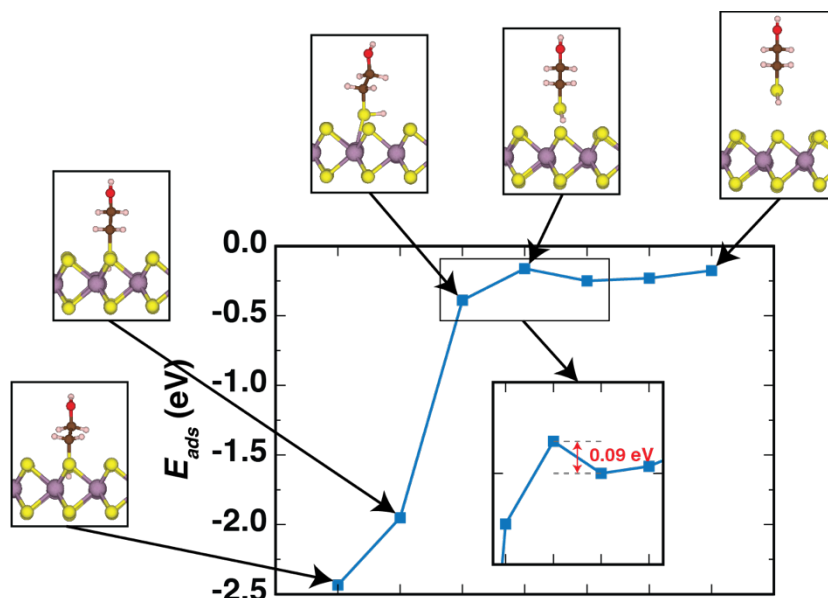


Figure 6.7. Energy barrier calculations of the ME molecule in a sulfur double vacancy. The inset shows the barrier measured at ~ 0.09 eV. The atoms shown in the figure are: Mo (purple), S (yellow), O (red), C (brown), and H (white).

In order to investigate the utility of defective and functionalized MoS₂ for electronic devices, we calculate the band structures and density of states of pristine, defective, and thiol-functionalized MoS₂ monolayers using DFT. The band gap of pristine MoS₂ calculated in the generalized gradient approximation is 1.62 eV (Figure 6.8a), in good agreement with previously published works.^{120,121} Although GGA is known to underestimate the true band gap, trends in changes to the band gap are preserved. To study the effects of S vacancies on the electronic structure, we compare the density of states of pristine and vacancy-containing MoS₂ with and without ME adsorption. A single isolated vacancy introduces a localized state below the conduction band (Figure 6.8b). The double sulfur vacancy introduces several states below the conduction band (Figure 6.8c), while the extended line vacancy results in a drastically altered band structure where the band gap is reduced to 0.37 eV (Figure 6.8d). ME adsorption on the pristine surface does not alter the electronic properties significantly (Figure 6.8e),

but Figure 6.8f shows that ME bonding to a single sulfur vacancy removes the gap state and completely passivates the vacancy. However, ME bonding to the double (Figure 6.8g) or line vacancy (Figure 6.8h) cannot fully passivate the vacancy and does not remove the gap states.

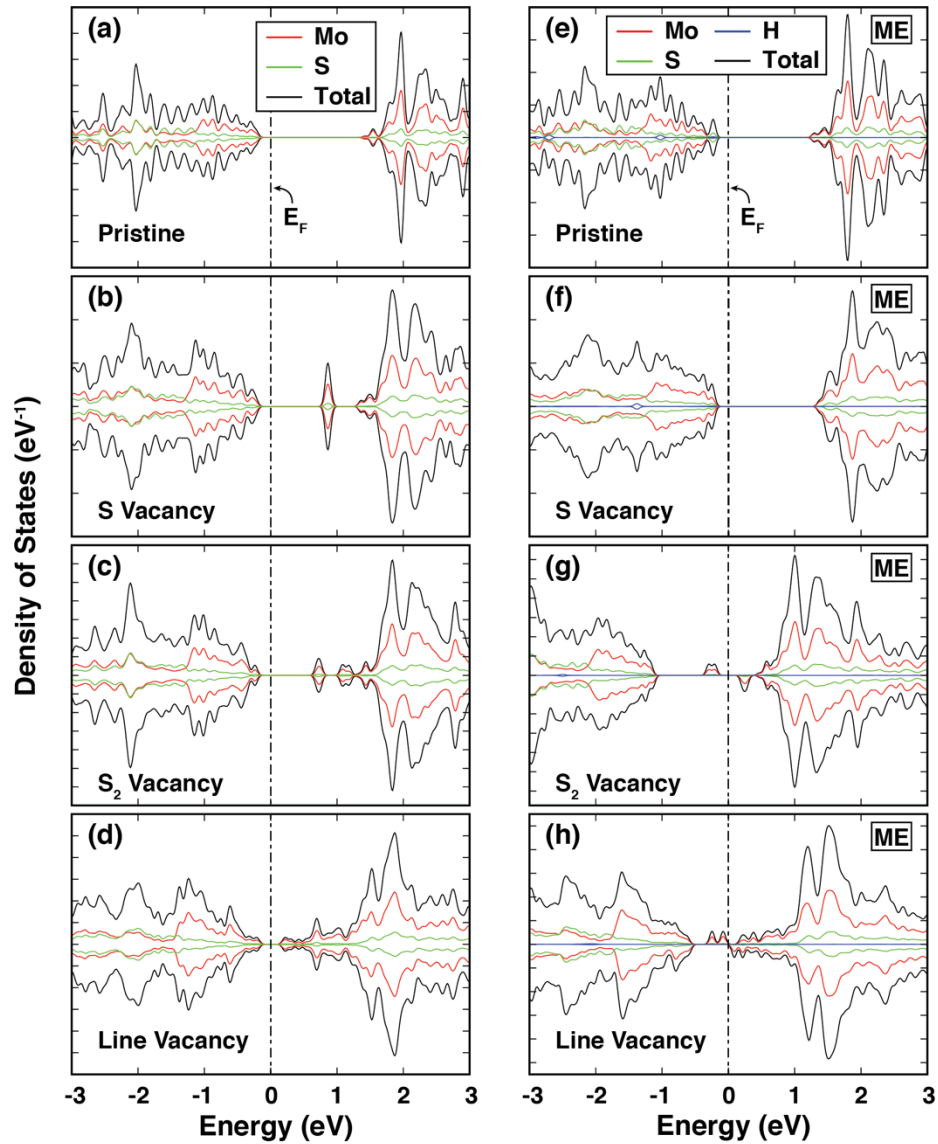


Figure 6.8. Density of states of (a) pristine MoS₂, (b) MoS₂ with a single S vacancy, (c) MoS₂ with a double S vacancy, and (d) MoS₂ with a line vacancy. Also shown are (e) ME on pristine MoS₂, (f) ME in a single S vacancy, (g) ME in a double S vacancy, and (h), ME in a line vacancy.

The O₂ molecule can also overcome a small energy barrier to bond in the double S vacancy. The double vacancy is not fully passivated in this state either, and gap states are present below the conduction band (Figure 6.9).

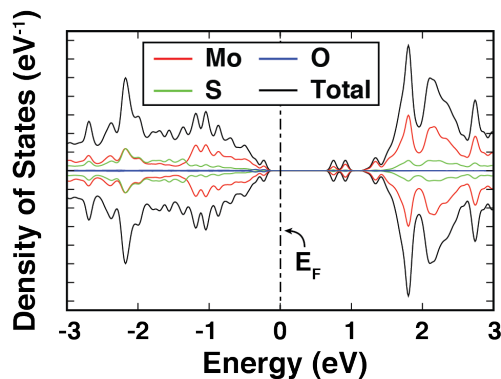


Figure 6.9. Density of states of an O₂ molecule in a double sulfur vacancy.

6.5. Discussion

It is well known that ALD of metal oxides on pristine, untreated MoS₂ surfaces typically results in poor quality films that are not fully coalesced.^{32,38,40,42,44,96–99} This necessitates the use of seeding approaches to modify the surface energy and consequently its reactivity. Self-assembled monolayer (SAM) type approaches are quite popular as they rely on self-assembly that can be accomplished in exposure times ranging from a few minutes to several hours. Thiols are commonly used SAM molecules and have been used on MoS₂ surfaces as they are expected to interact with the -S terminated surface or sulfur vacancies.^{58,59,100–111} One such thiol, mercaptoethanol (that has an -OH terminal group) is used in this work to promote the growth of TiO₂ ALD films on MoS₂. However, the results presented here suggest that a simple ME vapor treatment is not sufficient to improve film nucleation. Previous studies suggest that thiols primarily interact with sulfur vacancies on the MoS₂

surface,^{58,59,100–104,106–108} and our DFT calculations indicate that ME adsorption on the pristine MoS₂ surface is weak. Coupled with XPS analysis of the as-received CVD MoS₂ starting surfaces that indicates a low (~5%) concentration of sulfur defects, these facts explain the formation of non-continuous ALD films on ME-treated MoS₂. This observation points out that an increased concentration of surface defect sites may be required to achieve uniform film growth. Sputtering the MoS₂ surface with argon ions to create sulfur vacancies is used to produce increased concentrations (~8.5-20%) of sulfur vacancies and *in situ* XPS during ion bombardment show that the S:Mo ratio decreases with sputtering time (Figure 6.2), indicating that sulfur is preferentially removed during ion irradiation. Importantly, the XPS measurements do not show any noticeable changes in peak shapes for the Mo 3d and S 2p regions which indicate that the ion bombardment does not destroy the surface geometry. After treating these samples with ME, ALD of TiO₂ films result in uniform film growth, with no visible pinholes or gaps. However, sputtered samples that were not treated with ME show very similar film morphology (Figure 6.4).

6.5.1. Possible Growth Mechanisms

Sulfur vacancies are known to be reactive and may be passivated with oxygen or other species.^{93,118,119,122–129} We investigate several possible mechanisms for the uniform film growth on untreated, vacancy-containing MoS₂, including O₂ and H₂O adsorption on the S vacancy. The O₂ adsorption energy on the S vacancy is calculated as -0.09 eV, indicating weak physisorption. It has been shown previously that oxygen may chemisorb strongly in the S vacancy, and may do so dissociatively.^{93,118,119,124–126} However, in order for molecular oxygen to transition from the physisorbed state to the

chemisorbed state, it must overcome an energy barrier of 0.74 eV, for which the transition time is estimated to be ~ 20 h.¹¹⁸ To reach the dissociated state where one oxygen atom fills the S vacancy and one oxygen adsorbs on a nearby S atom, another energy barrier of 0.8-0.93 eV must be overcome.^{93,124} Though dissociative adsorption of O₂ would leave adsorbed oxygen atoms on the surface which are known to seed ALD films,³⁸ this pathway is deemed unlikely as our MoS₂ samples were exposed to air for a few minutes at most as they were transferred from the glove box into the ALD chamber. Adsorbed H₂O is also unlikely, as even on the reactive S vacancy, an H₂O molecule adsorbs with an adsorption energy of just -0.15 eV. In light of these results, we expect that single sulfur vacancies remain unpassivated and reactive prior to thiol treatment and ALD. DFT studies indicate that ME does not interact strongly with single sulfur vacancies or the pristine MoS₂ surface ($E_{ads} \sim -0.25$ eV). As the ALD process takes place at elevated temperatures, it is thus expected that the molecules may have desorbed from the surface before the film growth began.

As extended vacancies are possible at the high defect concentrations studied here, we chose to calculate the adsorption of ME on a double sulfur vacancy. While the ME molecule is unlikely to bind strongly to a single sulfur vacancy, it may bind strongly to a double vacancy. In this case, the S-H bond is broken, and the thiol chain and H atom occupy the neighboring vacancies. AIMD indicates that this functionalized structure is stable at high temperature, and therefore functionalization of extended vacancies may be a possible pathway for the smooth film growth observed in Figure 6.4a-c. O₂ may also bind strongly with a double vacancy. However, electronic structure calculations

reveal that the double vacancy is not fully passivated in this case (Figure 6.9) and thus may still be reactive to other chemical species.

Since the untreated, sputtered surfaces in Figure 6.4d-f also results in smooth ALD film growth, the interaction of TDMAT with the MoS₂ surface is considered. Calculations of TDMAT adsorption on the S vacancy show that the interaction between TDMAT and the vacancy-containing MoS₂ layer is strong ($E_{ads} = -0.43$ eV), and AIMD simulations at 600K do not result in desorption of the TDMAT molecule. Calculations of TDMAT adsorption on double sulfur vacancies result in similar adsorption energies. Therefore, TDMAT adsorption on single S vacancies is one possible pathway of seeding TiO₂ film growth on the defective MoS₂ seen in Figure 6.4d-f. The weak interaction of O₂ and H₂O with the single S vacancy suggests that adsorption of these molecules on single vacancies is unlikely, but adsorption of these molecules on extended vacancies is expected as a result of their strong binding with double S vacancies. Furthermore, at the low deposition temperature used here, some precursor condensation on the pristine surface is expected. Condensation alone is not sufficient to promote smooth film growth, as evidenced by the pinhole-containing films in Figure 6.1a,b, but we expect that the smooth films seen in Figure 6.4d-f are a result of a convolution of TDMAT condensation and TDMAT adsorption on S vacancies. This result should be applicable to all precursors of the same alkylamine family but whether it applies to other ALD precursor families should be investigated separately. Based on these results, the smooth film growth on ME-treated surfaces (Figure 6.4a-c) results from a combined effect of precursor condensation, TDMAT adsorption on unpassivated vacancies, and TDMAT reaction with adsorbed ME.

6.5.2. Electronic Properties of Defective MoS₂

While a smooth oxide layer is important for device applications, the question remains as to the usefulness of defective MoS₂ for electronic devices. DFT calculations of the electronic structure show that introducing S vacancies creates a gap state that reduces the band gap of the MoS₂ monolayer (Figure 6.8b). These gap states can trap or scatter charge carriers and decrease the charge carrier mobility. Passivation of the single S vacancy with ME is possible and does remove the gap state. However, density of states calculations of ME-passivated extended vacancies reveal that the gap states are not removed, but are modified upon ME bonding (Figure 6.8g,h). The adsorbed thiol molecule does not heal these vacancies, but introduces spin-dependent gap states above and below the Fermi level. While the chemisorbed thiol chain can passivate the S vacancy that it occupies, the H atom occupying the neighboring site can not satisfy the dangling bonds left by the lack of a sulfur atom. Likewise, O₂ and H₂O cannot passivate the double S vacancy and leave the system with less than desirable electronic properties.

Although our calculations show that TDMAT adsorption on S vacancies is strong, it is not clear whether the resulting ALD reaction products passivate the vacancy. However, previous works have shown that encapsulating the MoS₂ layer with a high-k dielectric material increases charge carrier mobility,^{130–132} and such effects may still be possible in this system. Additionally, some of the damaging effects of surface vacancies may be mitigated in systems of bi-layer or tri-layer MoS₂, as has been reported for devices formed using plasma-enhanced ALD.¹³³

6.6. Conclusions

In summary, as a result of the combined experimental and computational treatment of the TDMAT-ME-vacancy rich MoS₂ system we can conclude that a high surface density of S vacancies is desired to achieve the deposition of a high-quality dielectric with thickness <10 nm. The high reactivity of the TDMAT precursor with the surface vacancies is sufficient to produce a continuous film. However, the resulting electronic structure is not favorable due to the presence of gap states. ME passivation of single sulfur vacancies results in removal of the gap state, but ME bonding to double vacancies does not. Introduction of O₂ or H₂O to the double vacancy likewise cannot remove the electronic gap states. Nevertheless, this work reveals how surface defect engineering can increase the reactivity of the MoS₂ surface and can lead to further advances in the tailoring of the surface and electrical properties of two-dimensional materials.

Chapter 7. Spontaneous Curvature of Janus Transition Metal Dichalcogenide Nanoribbons

7.1. Introduction

Janus transition metal dichalcogenides (TMDs) are a subset of TMDs where one entire side of chalcogen atoms is replaced with another chalcogen type (S, Se, or Te), resulting in a material with two different faces, resulting in a layered structure of X-M-Y (M = metal, X, Y = chalcogens). These materials have been predicted theoretically and MoSSe has been experimentally synthesized.^{134,135} The synthesis of Janus TMDs provides another path towards tuning the electronic properties of single-layer TMDs. The properties of Janus TMDs have been studied in monolayers,^{134–138} bilayers,^{139,140} and nanotubes.^{141–143} Janus TMDs possess an intrinsic dipole moment, and thus may be useful for interesting device applications. For example, molybdenum-based Janus TMDs have been proposed as efficient photocatalysts for water splitting.^{144,145}

The creation of quasi-one-dimensional nanoribbons can have drastic impacts on the electronic and magnetic properties of TMDs and other hexagonal-structured materials. For instance, while two-dimensional graphene does not have a band gap, graphene nanoribbons exhibit finite band gaps as a result of quantum confinement and edge effects, both of which are direct consequences of the reduced dimensionality.^{146–148} Semiconducting MoS₂ becomes metallic and magnetic when cut into zigzag nanoribbons,^{149–152} while armchair nanoribbons maintain their semiconducting properties with a band gap that is dependent on the ribbonwidth.^{149,150,153} As such, reducing the dimensionality of two-dimensional materials to quasi-one-dimensional structures provides another mechanism for carefully tuning the electronic and magnetic

properties of the material. Nanoribbons can have a variety of uses in nanoelectronics and other applications. For example, semiconducting MoS₂ nanoribbons have been used as the channel material in field effect transistors.¹⁵⁴ Ferromagnetic zigzag MoS₂ nanoribbons have been predicted to be useful for spintronic devices¹⁵² and even effective cathode materials for Mg-based batteries.¹⁵⁵ Graphene nanoribbons may be used as nanoscale metallic junctions¹⁵⁶ or for catalysis of oxygen evolution/oxygen reduction reactions.¹⁵⁷

In this work, we investigate the structural, electronic, and magnetic properties of molybdenum-based and tungsten-based Janus TMD nanoribbons in the H phase. We find that unsupported nanoribbons undergo spontaneous curvature as a result of strain between the top and bottom sides of the ribbons. We investigate the effects of curvature on the electronic and magnetic properties of both zigzag and armchair nanoribbons. While curvature does not strongly affect the magnetic properties of zigzag nanoribbons, it can modify the band gap of semiconducting armchair nanoribbons. Finally, we investigate the effects of hydrogen edge passivation on both the electronic and magnetic properties of the ribbons and on the reconstruction of the ribbon edges. Hydrogen passivation stabilizes the nanoribbon edges against reconstruction and enhances the magnetic properties of zigzag nanoribbons. Passivation tends to widen and stabilize the band gap of armchair nanoribbons. These results suggest that Janus TMD nanoribbons could be suitable for a number of applications, such as spintronics or metallic junctions (zigzag nanoribbons) or nanoelectronics devices (armchair nanoribbons).

7.2. Computational Details

The electronic, magnetic, and structural properties of two-dimensional Janus TMDs and Janus TMD nanoribbons are calculated using density functional theory (DFT) implemented in the Vienna Ab initio Simulation (VASP) package,⁷³ with the generalized gradient approximation (GGA) of Perdew-Burke-Ernzerhof (PBE) for the exchange-correlation functional.⁶⁶ We calculate the electronic properties of the two-dimensional Janus TMD materials using PBE, including spin-orbit coupling (SOC), as well as with the hybrid functional of Heyd-Scuseria-Ernzerhof (HSE)¹⁵⁸ with SOC. For two-dimensional Janus TMDs, we use a cutoff energy of 450 eV and Monkhorst-Pack k-point sampling with $20 \times 20 \times 1$ k-points. For all nanoribbons, we use a cutoff energy of 300 eV to reduce the computational demands, as these simulation cells contain up to 42 atoms and long vacuum lengths in two directions. We set the vacuum length of the unit cells to be 20 Å to avoid spurious interaction between images. For structural optimization and self-consistent calculations of the nanoribbons, Monkhorst-Pack k-point sampling with $1 \times 1 \times 16$ k-points is used. This optimal k-point sampling was chosen after convergence tests. For all calculations, Gaussian smearing with a value of $\sigma = 0.01$ is used. Structural optimization of all materials is performed with an energy convergence criterion of 10^{-5} eV and a force convergence criterion of 0.05 eV/Å.

7.3. Results and Discussion

7.3.1. Structural Properties

We begin our study by investigating the properties of six Mo- and W-based Janus TMDs in their two-dimensional form. The optimized geometries, equilibrium lattice

parameters, and band structures (calculated with HSE+SOC) of these materials are shown in Figure 7.1.

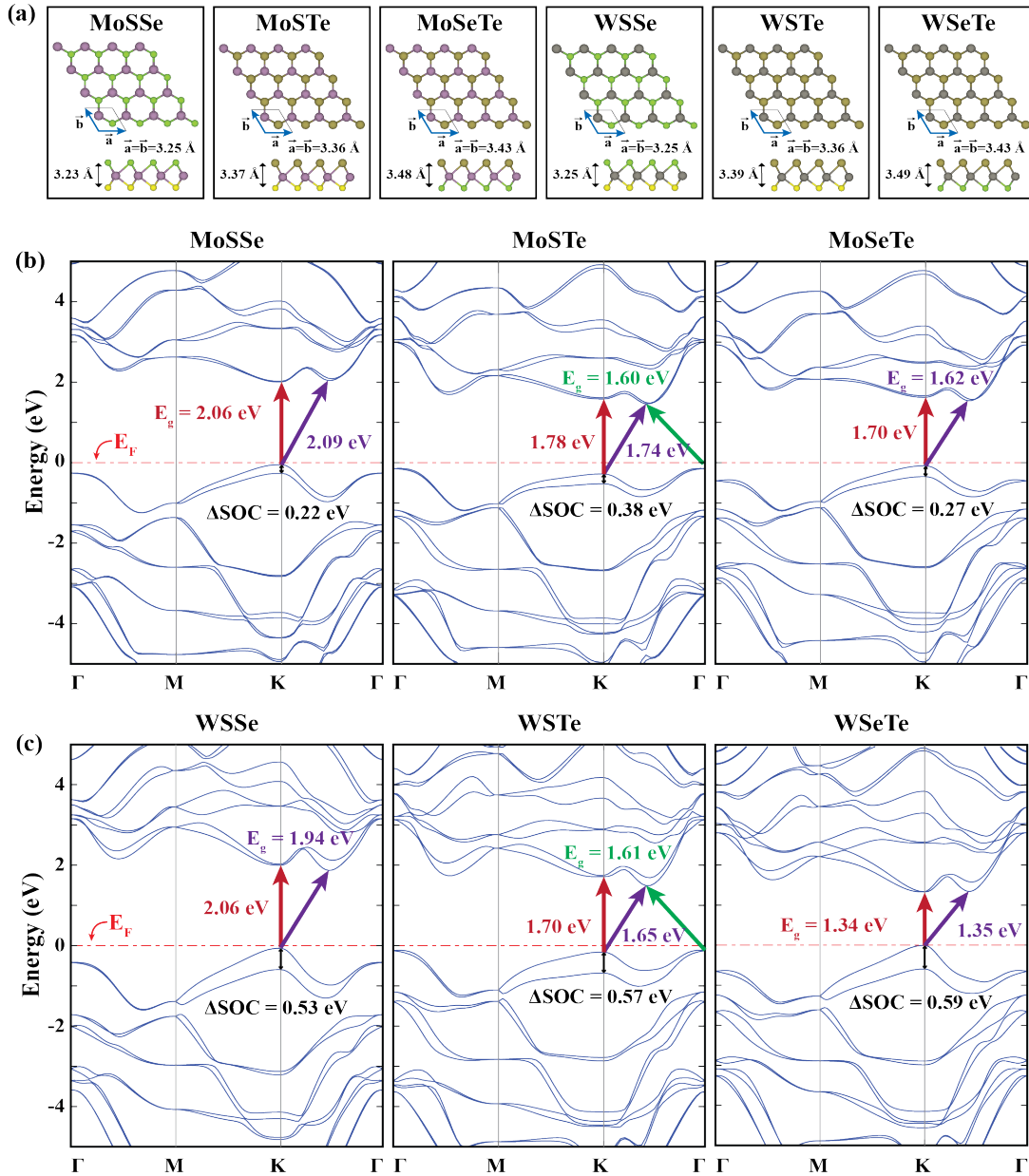


Figure 7.1. (a) Optimized structures of the 2D Janus TMDs (relaxed with PBE) (b) and the band structures (calculated with HSE+SOC) of Mo-based (c) and W-based Janus TMDs. The dashed red line denotes the Fermi level. The red, green, and purple arrows denote the competing band gap energies: red (direct gap at the K point), purple (K point to low point of valence band), and green (indirect band gap of MoSTe and WSTe structures). The spin-orbit splitting at the K point (ΔSOC) is labeled in black.

The band structures reveal competing transitions between a direct gap at the K point and an indirect gap from the K point to midway between K and Γ points. MoSTe and WSTe materials exhibit an indirect band gap from the Γ point to the K point.

The lattice parameters of the 2D Janus materials and 2D MX₂ materials calculated with PBE are compiled in Table 7.1. Also included in Table 7.1 are the band gaps of these materials calculated with PBE and HSE (with and without SOC). The lattice parameter of all Janus MXY materials is equal to the average of the corresponding MX₂/MY₂ structures. For example, the lattice parameter of MoSSe is 3.25 Å, which equals the average of MoS₂ (lattice parameter = 3.18 Å) and MoSe₂ (lattice parameter = 3.32 Å). Similarly, the band gap of a Janus MXY material is very nearly the average of the band gap of the corresponding MX₂/MY₂ materials, except in the case of MoSTe and WSTe, which are indirect gap materials.

Table 7.1. Lattice properties and band gaps of Mo/W TMDs and Janus TMDs.

Material	a = b (Å)	Band Gap PBE (eV)	Band Gap PBE+SOC (eV)	Band Gap HSE+SOC (eV)	Direct Band Gap K Point (eV)	Band Character
MoS ₂	3.18	1.68	1.56	2.23	2.23	Direct
MoSe ₂	3.32	1.44	1.29	1.61	1.61	Direct
MoTe ₂	3.55	1.08	0.89	1.49	1.49	Direct
MoSSe	3.25	1.54	1.45	2.06	2.06	Direct
MoSTe	3.36	1.02	1.00	1.60	1.78	Indirect
MoSeTe	3.43	1.27	1.15	1.70	1.62	Indirect
WS ₂	3.18	1.90	1.52	1.92	1.92	Direct
WSe ₂	3.32	1.63	1.23	1.85	1.85	Direct
WTe ₂	3.55	1.13	0.72	0.95	0.95	Direct
WSSe	3.25	1.69	1.42	1.94	2.06	Indirect
WSTe	3.36	1.22	1.14	1.61	1.70	Indirect
WSeTe	3.43	1.35	1.06	1.34	1.34	Direct

For traditional TMDs such as MoS_2 , it has been shown that the creation of one-dimensional nanoribbons can drastically alter the electronic and magnetic properties of the material.^{149–151,153,159} In this work, we investigate the structural deformation of, and the electronic and magnetic properties of Janus TMD nanoribbons. Xiong et al. previously showed via classical molecular dynamics simulations that freestanding sheets of MoSSe undergo spontaneous curling to form bowl-like or tube-like structures,¹⁶⁰ and thus, we expect to see similar curling of the Janus TMD nanoribbons. Here, we consider nanoribbons classified both by their edge structure (zigzag and armchair) and their width. The width of the nanoribbons is specified by the number (n) of metal (Mo, W) atoms in the unit cell. We study armchair nanoribbons (ANRs) of widths $n=6$ to $n=14$ and zigzag nanoribbons (ZNRs) of widths $n=4$ to $n=8$. These widths are chosen as they represent physical nanoribbon widths of 10-20 Å.

Examples of an armchair and a zigzag nanoribbon of MoSSe are depicted in Figure 7.2. The zigzag ribbon in Figure 7.2 with $n=8$ is denoted as Z8 MoSSe , and the armchair ribbon with $n=14$ is denoted as A14 MoSSe . The nanoribbons extend infinitely in the z -direction.

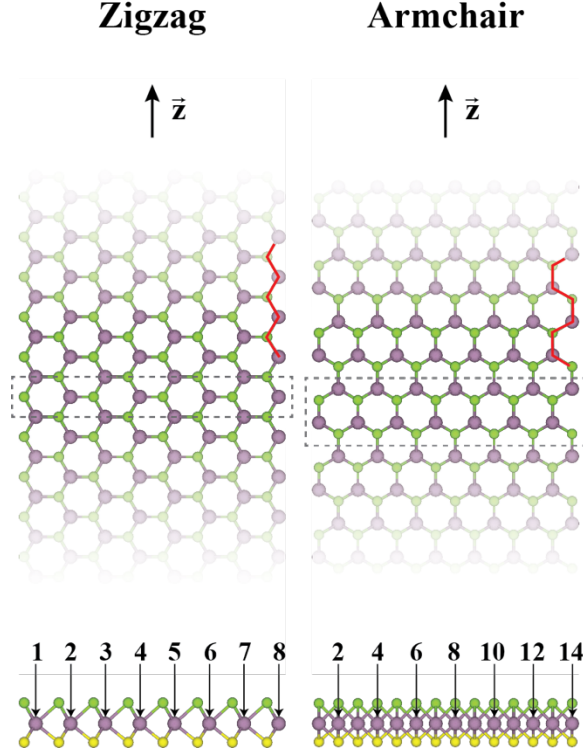


Figure 7.2. Unrelaxed structures for zigzag (left, Z8) and armchair (right, A14) nanoribbons. The nanoribbon widths are characterized by the number of metal atoms in the unit cell. The unit cells are outlined with gray dashed lines and the zigzag/armchair edges are outlined in red on each structure.

The nanoribbons undergo spontaneous curvature as a result of the lattice mismatch between the top and bottom sides. As the Janus TMD lattice parameter is the average of the two MX_2 structures, the top side (larger atom) experiences positive strain while the bottom side (smaller atom) experiences negative strain. These combined strain effects force the nanoribbon to curl about the z-axis. The radius of curvature of all nanoribbons is calculated by fitting the y-coordinate of the nanoribbons' metal atoms to a least-squares circle. The cohesive energy of the relaxed nanoribbons is calculated as

$$E_{coh} = [E_0 - n \times (E_M + E_X + E_Y)]/3n \quad (7.1)$$

where n is the number of metal atoms in each unit cell (and also the number of X and Y atoms in each cell). Here E_0 is the total relaxed nanoribbon energy and E_M , E_X , and

E_Y are the free energies of an isolated M atom, X atom, and Y atom, respectively. As a proxy for substrate-supported ribbons, we also perform structural relaxation of the nanoribbons with the z-coordinate of the metal atoms fixed (henceforth referred to as “flat” nanoribbons). These structures are used to calculate the curvature energy of the unsupported nanoribbons as

$$E_{curvature} = E_0 - E_{flat} \quad (7.2)$$

where E_0 and E_{flat} are the total energy of the curved and flat relaxed nanoribbons, respectively. The curvature energy is plotted as a function of nanoribbon width in Figure 7.3. The radius of curvature, cohesive energy, and curvature energy of all nanoribbons are compiled in Table A-1.

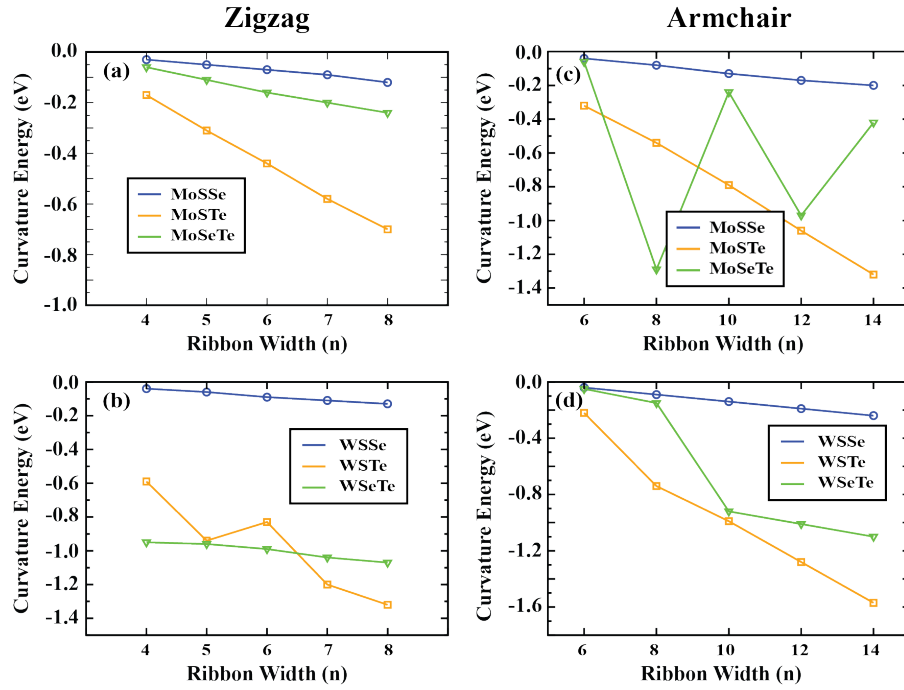


Figure 7.3. Curvature energy as a function of nanoribbon width for (a) zigzag Mo-based nanoribbons, (b) zigzag W-based nanoribbons, (c) armchair Mo-based nanoribbons, and (d) armchair W-based nanoribbons.

Generally, the radius of curvature tends to increase as the nanoribbon width increases. The curvature energy tends to become more negative as the nanoribbon

width increases, indicating that wider nanoribbons more strongly prefer to exist in their curved state. However, curvature energy calculations also include edge reconstruction effects, which causes the curvature energy to fluctuate in the case of WSTe ZNRs (Figure 7.3b) and MoSeTe ANRs (Figure 7.3c). The relaxed structures for the widest of each species of nanoribbon are shown in Figure 7.4. The relaxed zigzag nanoribbons of MoSSe and WSSe exhibit mild curvature and edge reconstruction (Figure 7.4a,d) because of the low lattice mismatch between the MS_2 and MSe_2 structures. In both MoSTe and MoSeTe ZNRs, the Mo-terminated edge undergoes a reconstruction to a more linear-like geometry, with the Te atoms aligning in the z-direction. The WSTe and WSeTe ZNRs display further reconstruction of the W-terminated edge. The lowest-energy geometry for these structures is when the Te atoms on the right edge are displaced along the x-axis away from the ribbon center and the W atom on the right edge is displaced in the z-direction (out of the plane of the ribbon).

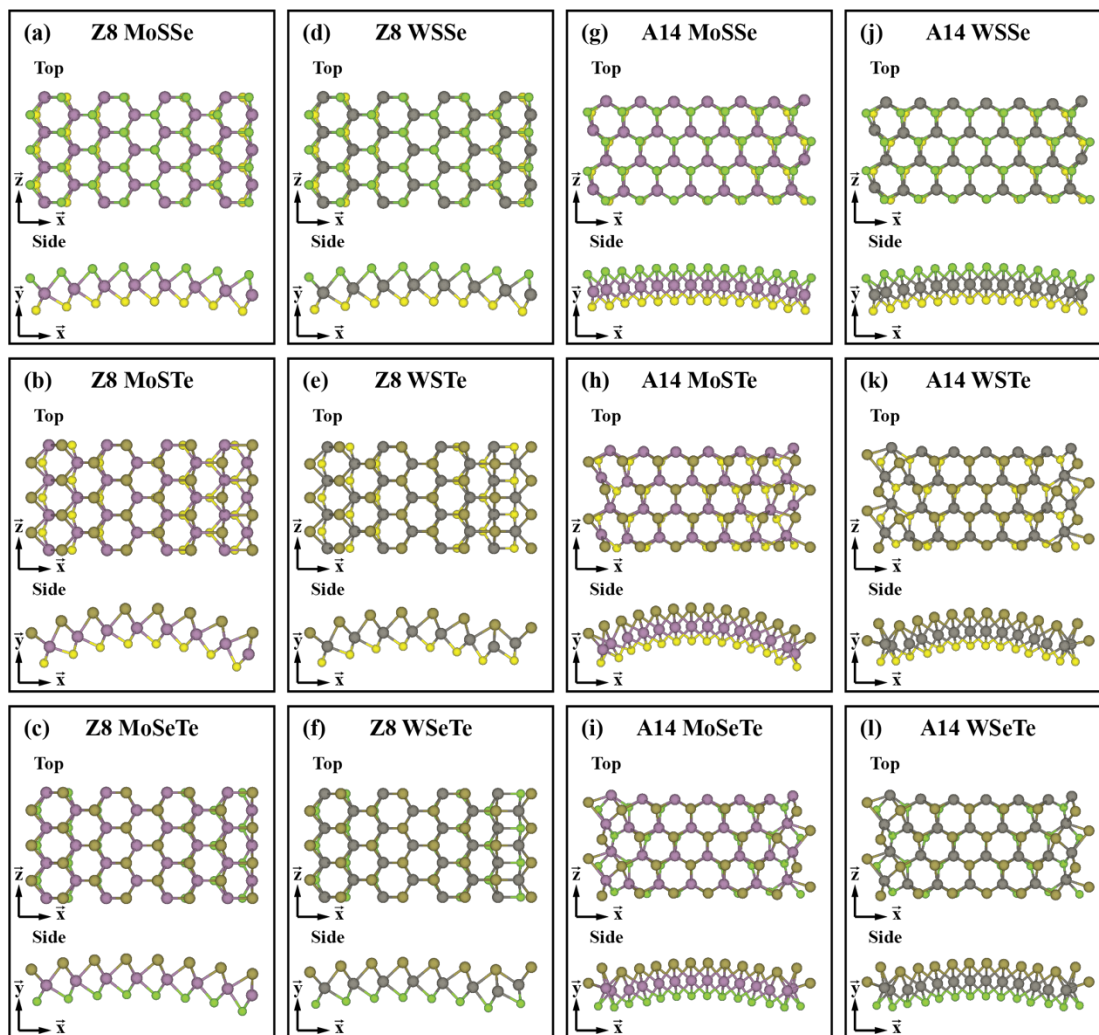


Figure 7.4. Fully relaxed geometries for Z8 (a) MoSSe, (b) MoSTe, (c) MoSeTe, (d) WSSe, (e) WSTe, and (f) WSeTe. Fully relaxed geometries for A14 (g) MoSSe, (h) MoSTe, (i) MoSeTe, (j) WSSe, (k) WSTe, and (l) WSeTe.

Initially, relaxation of the WSTe structures lead to a positive curvature energy, as a consequence of the reconstruction of the flat nanoribbon edges differing from the reconstruction of the curved nanoribbon edges. In fact, not all of the flat WSTe ribbons initially displayed the same edge reconstruction. To resolve this issue, we performed low-temperature (100 K) molecular dynamics relaxations of the flat WSTe ZNRs to overcome the activation barrier for edge reconstruction, and then optimized the final flat structures with DFT. The ground-state flat structures for W-based ZNRs with $n=8$

are shown in Figure 7.5. The displacement of Te atoms in the WSTe and WSeTe ZNRs occurs during relaxation of the flat nanoribbons. After this final DFT optimization, a full geometric relaxation allows the ribbons to curve, resulting in the optimized ground state geometry described above.

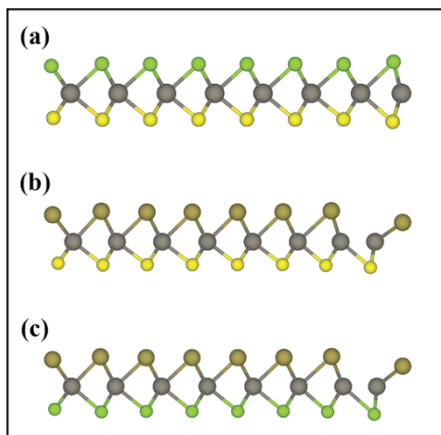


Figure 7.5. Relaxed flat structures for Z8 (a) WSSe, (b) WSTe, and (c) WSeTe.

Armchair nanoribbons undergo varying degrees of edge reconstruction depending on the nanoribbon's composition. MoSSe and WSSe ANRs display only mild distortion of the ribbon edges, while MoSTe, MoSeTe, WSTe, and WSeTe ANRs exhibit more serious edge reconstruction. Particularly, the two Mo atoms nearest to each edge in the MoSeTe ANRs align in a nearly linear formation along the z-direction. The outermost Mo atoms in the widest MoSeTe nanoribbon (A14) also dislocate out of the plane of the ribbon in the y-direction. MoSTe ANRs do not exhibit complete linear alignment of the Mo edge atoms, but the outermost Mo atoms do move along the x-direction towards the center of the ribbon, distorting the hexagonal lattice at the ribbon edges. WSTe and WSeTe ANRs display similar reconstruction to the MoSTe ANRs. Like the MoSeTe A14 nanoribbon, the edge W atoms of the WSeTe A10-A14 nanoribbons and the WSTe A8-A14 nanoribbons dislocate out of the plane in the y-direction.

7.3.2. Electronic and Magnetic Properties

It has previously been shown that MoS₂ and WS₂ zigzag nanoribbons are metallic and magnetic^{149–151,153,159,161} and similarly, zigzag Janus MoSSe nanoribbons were shown to be ferromagnetic metals.¹⁶² Calculations performed in this work show that all Mo- and W-based zigzag Janus nanoribbons are likewise metallic and magnetic. Initial magnetic moments between 1 and 3 μB were investigated to find the ground state ordering. The magnetic coupling between the nanoribbon edges is weak, so the conjugate gradient algorithm cannot easily converge to the lowest possible state upon normal electronic minimization. As a result of several trials, we conclude that the magnetic properties presented here are the most likely ground state properties. The calculated magnetic moments are compiled in Table A-1 and shown graphically in Figure 7.6.

Curvature of the nanoribbons does not strongly change their magnetic moments, as the magnetic nature is a result of edge effects rather than the arrangement of atoms. The magnetic moment of the Mo-based nanoribbons generally increases as the ribbon width increases (Figure 7.6a). However, the MoSTe nanoribbons do not exhibit a monotonic increase in magnetic moment as a result of differences in magnetic ordering between the n=4-6 and n=7-8 nanoribbons, which will be discussed later.

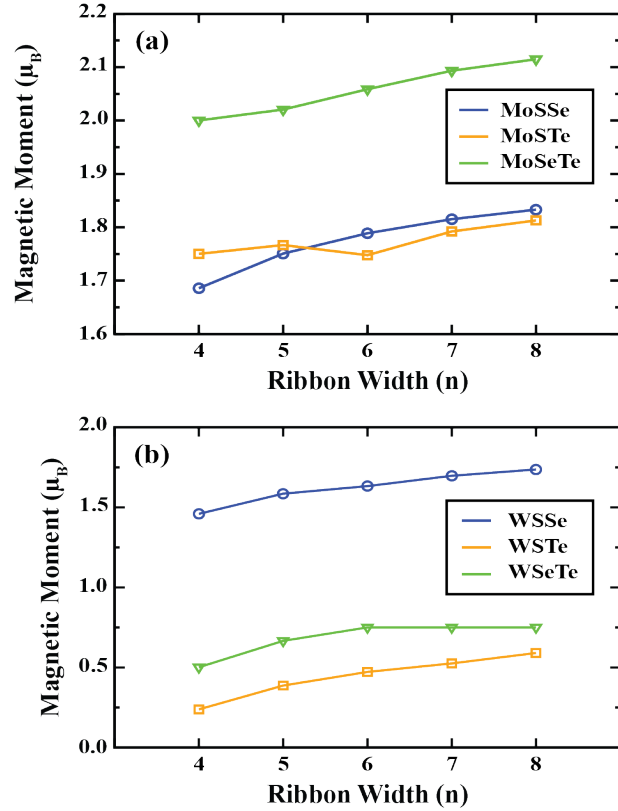


Figure 7.6. Magnetic moments vs nanoribbon width for (a) Mo-based and (b) W-based zigzag nanoribbons.

WSSe and WSTe ZNRs display a monotonically increasing magnetic moment, while the magnetic moment of WSeTe nanoribbons increases until saturation at a width of $n=6$ (Figure 7.6b). In addition to calculations of the total magnetic moment, examination of the magnetic ordering of the nanoribbons reveals four classes of magnetic structure as identified by the magnitude and direction of the electron spin on each atom. This is shown schematically in Figure 7.7. In all cases, the most significant contributions to the overall magnetic moment come from the atoms nearest to the nanoribbon edges. The primary contributions are from the metal atoms near the edge, but there are also contributions from chalcogen atoms with unsaturated bonds.

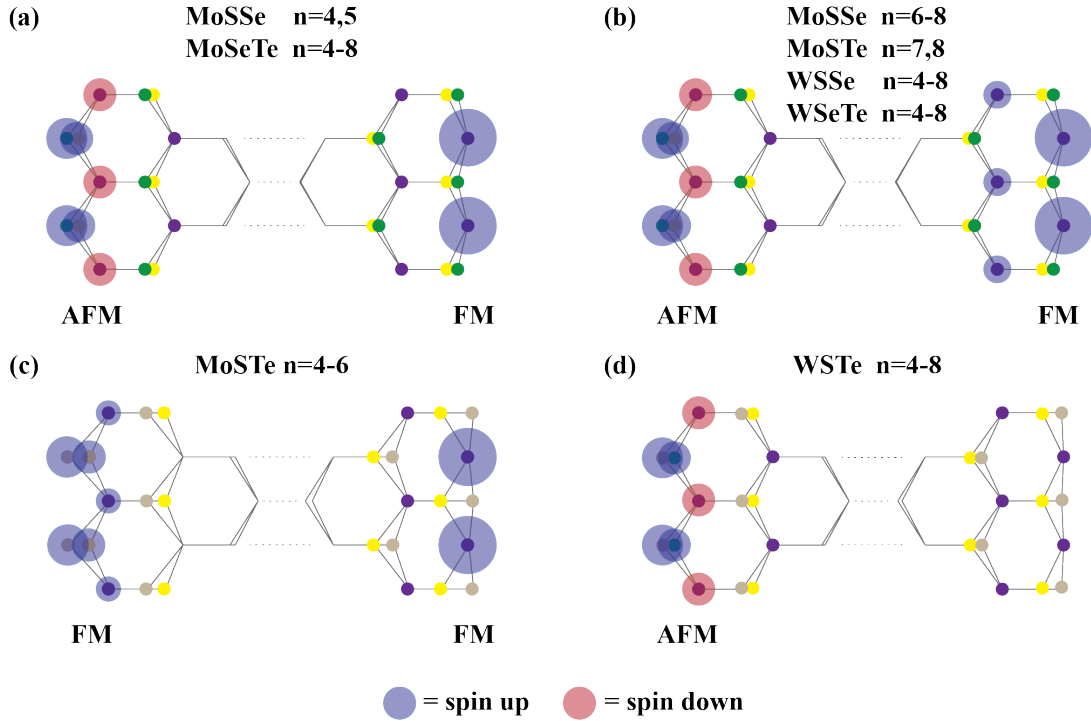


Figure 7.7. Schematic diagram of magnetic ordering of zigzag nanoribbons.

Most ZNRs display antiferromagnetic (AFM) coupling between the metal and chalcogen atoms on the left edge and ferromagnetic (FM) coupling of the metal atoms on the right edge. Narrow MoSSe ZNRs ($n=4,5$) display AFM coupling on the left edge and FM coupling on the right edge, with FM contributions from only the edge Mo atoms (Figure 7.7a). Wider MoSSe ZNRs ($n=6-8$) have an additional contribution to the FM coupling on the right edge from the nearest-neighbor Mo atoms (Figure 7.7b). While performing calculations to find the ground state magnetic ordering of MoSTe ZNRs, we found that there are very small (on the order of 0.001 eV) energy differences between configurations with AFM coupling and configurations with FM coupling. Thus, we performed calculations including spin-orbit coupling for the MoSTe ZNRs to determine the ground state magnetic ordering. For MoSTe ZNRs of widths $n=4-6$, we observe FM coupling of the metal and chalcogen atoms on the left edge (Figure 7.7c)

along with linear edge reconstruction and FM coupling of metal atoms on the right edge. The ordering reverts to left edge AFM coupling for MoSTe ZNRs of widths $n=7,8$. All MoSeTe ZNRs display AFM coupling of the left edge and FM coupling of the right edge (Figure 7.7a). WSSe ZNRs display similar magnetic ordering to the wider ($n=6-8$) MoSSe ZNRs (Figure 7.7b). WSeTe ZNRs also display the magnetic ordering depicted in Figure 7.7b. Similar to the MoSTe ZNRs, there are small energy differences between AFM and FM orderings of the WSTe ZNRs. Therefore, to find the ground state magnetic ordering of the WSTe ZNRs, we carried out calculations including spin-orbit coupling. The WSTe ZNRs display AFM coupling only along the left edge between the W atoms (spin down) and chalcogen atoms (spin up), with no significant contribution from W atoms on the right edge of the ribbon (Figure 7.7d).

Similar to the single-layer Janus materials and to MoS₂ nanoribbons, the armchair nanoribbons are semiconductors.^{149,150,153} While 2D single-layer MoSSe has a direct band gap, all MoSSe ANRs possess indirect band gaps. MoSTe ANRs remain indirect band gap semi-conductors. However, the remaining ANRs (MoSeTe, WSSe, WSTe, and WSeTe) undergo a transition from indirect to direct gap semiconductors as the nanoribbon width increases. This transition occurs at $n=8$ for all materials except WSeTe, where the transition occurs at $n=10$. The $n=8$ ribbons are very narrow (10 Å) so we expect physically realized nanoribbons of these materials to be primarily direct gap semiconductors. The band gap values as a function of ribbon width are shown in Figure 7.8 for both curved and flat ribbons, and the band gaps and gap character are compiled in Table A-1. The band gaps of MoSSe and WSSe ANRs are virtually unaffected by curvature and generally increase with ribbon width.

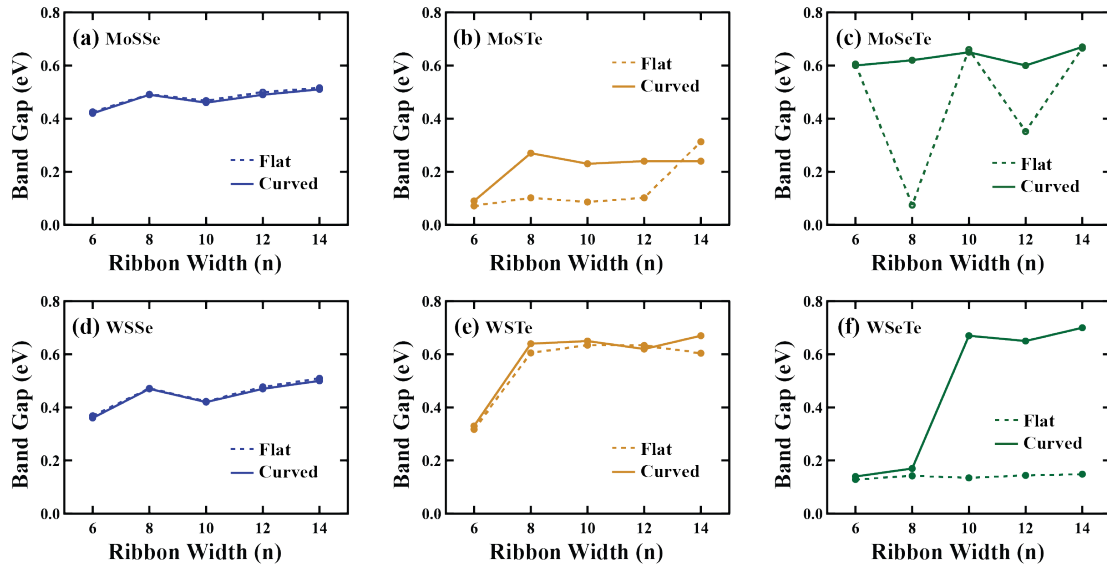


Figure 7.8. Band gaps vs. nanoribbon width for curved and flat armchair nanoribbons.

These ribbons display only a small degree of curvature, and thus the band gaps are relatively unchanged. Additionally, the band gaps of the WSTe ribbons are unchanged by curvature. The band gaps of the WSTe ribbons increase with ribbon width, but quickly saturate to ~ 0.63 eV at a width of $n=8$. In contrast, MoSTe and MoSeTe ANRs display changes in band gap values after they undergo spontaneous curvature. Curved MoSTe ribbons display a similar trend to WSTe ribbons, with an increasing band gap saturating at a width of $n=8$ and a gap value of ~ 0.23 eV. All flat MoSTe ribbons have a band gap of ~ 0.1 eV, except $n=14$ ($E_g \sim 0.3$ eV). For curved MoSTe nanoribbons, the band gaps are arising from the edge states as a result of significant edge reconstruction. However, for flat MoSTe ribbons, similar edge reconstruction does not appear until at or after $n=14$. For narrower flat MoSTe ribbons, because of lack of edge reconstruction, the conduction band minimum (CBM) is homogeneously distributed over the ribbon.

One can observe the most severe difference between flat and curve armchair ribbons on MoSeTe and WSeTe. Curved MoSeTe ribbons all display a band gap

of ~ 0.6 - 0.65 eV, while for flat MoSeTe ribbons, the band gap oscillates with increasing ribbon width. Since the trends on the curvature energy (Fig. 7.3c) and the band structure of MoSeTe are similar, one has to focus on the edge reconstruction on the $n=8$ and $n=12$ nanoribbons to understand the divergence. The main difference between $n=8$ and $n=12$ flat and curved ribbons is that while for curved ribbons the CBM is dispersed across the ribbon, for flat ribbons the CBM is mainly localized to edge states as a result of different edge reconstruction.

For WSeTe ribbons, there is a change in band structure from narrow ribbons ($n=6, 8$) to wider ribbons ($n=10, 12, 14$). Narrow curved and flat ribbons exhibit similar edge reconstruction, and the valence band maximum (VBM) of the narrow ribbons (curved and flat) arises from localized edge states, while the CBM of the narrow ribbons is distributed across the ribbons. For the wider ribbons, the flat ribbons undergo stronger edge reconstruction and the VBM is now distributed homogeneously across the band. The VBM for the curved ribbons remains localized to the edges. The CBM is localized to the edges for both curved and flat ribbons, but the gap value changes as a result of differing edge reconstruction.

7.3.3. Hydrogen Passivation

Previously, we studied bare nanoribbons whose edge atoms possess unsaturated bonds. In this section, we investigate the effects of hydrogen passivation of the nanoribbon edges on the electronic and magnetic properties of the nanoribbons. The edge M atoms (Mo, W) are passivated with two H atoms each and the edge chalcogen atoms (S, Se, Te) are passivated with one H atom each. The relaxed structures for the

widest H-passivated nanoribbons are shown in Figure 7.9. Hydrogen passivation stabilizes both the zigzag and armchair edges, resulting in less severe edge reconstruction. H-passivated zigzag WSTe and WSeTe nanoribbons (Figure 7.9) do not exhibit the same dislocation of the edge W atoms seen in the case of the bare ribbons (Figure 7.4). Additionally, hydrogen passivation prevents the dislocation of edge Mo and W atoms in the MoSeTe and WSTe/WSeTe ANRs, respectively.

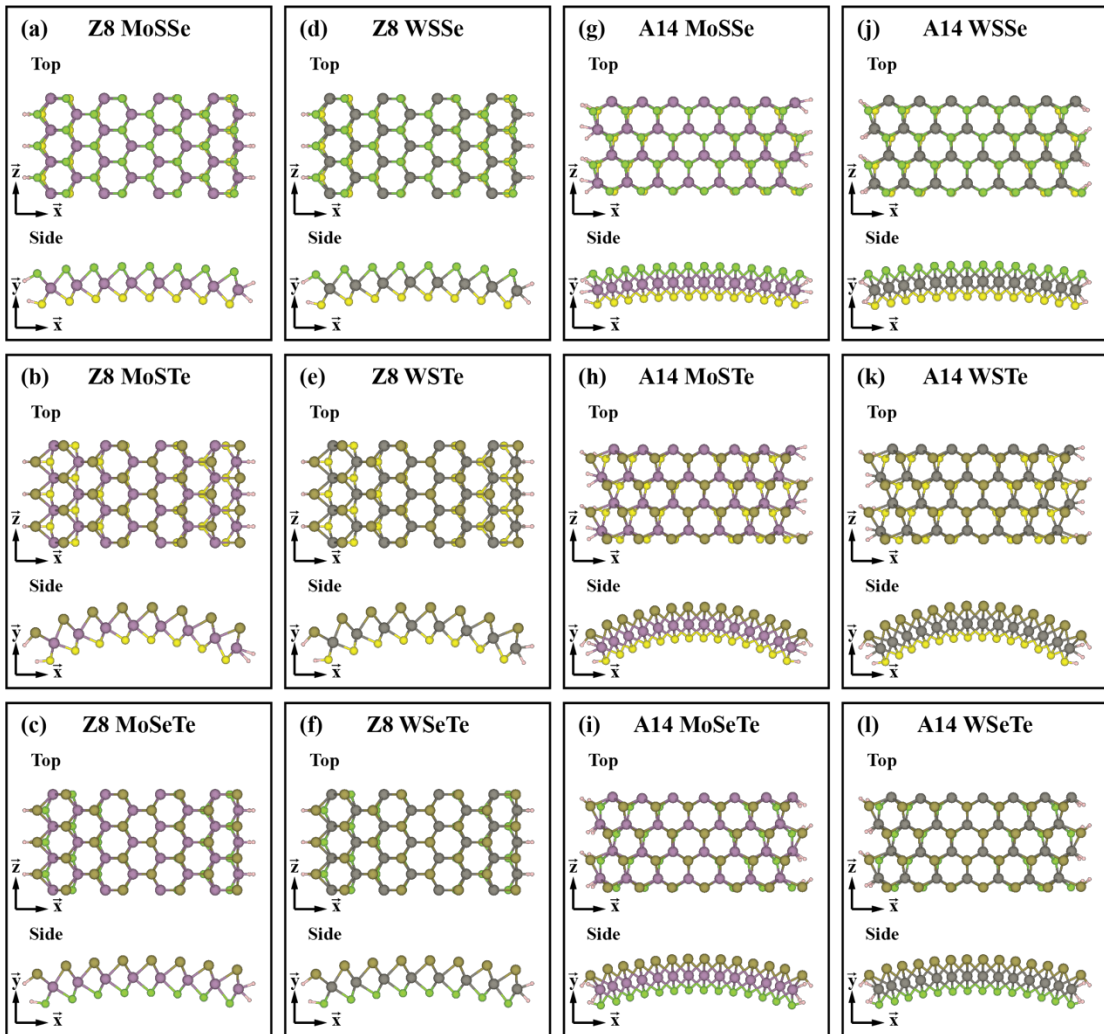


Figure 7.9. Fully relaxed geometries for hydrogen-passivated Z8 (a) MoSSe, (b) MoSTe, (c) MoSeTe, (d) WSSe, (e) WSTe, and (f) WSeTe. Fully relaxed geometries for hydrogen-passivated A14 (g) MoSSe, (h) MoSTe, (i) MoSeTe, (j) WSSe, (k) WSTe, and (l) WSeTe.

Similar to the bare nanoribbons, H-passivated ZNRs are metallic and magnetic (except for WSeTe ZNRs, which are non-magnetic metals) while H-passivated ANRs are semiconducting, similar to the bare nanoribbons. Upon investigation of the magnetic ordering of the H-passivated ZNRs, we find four classes of magnetic structure. A schematic of the observed magnetic orderings is shown in Figure 7.10.

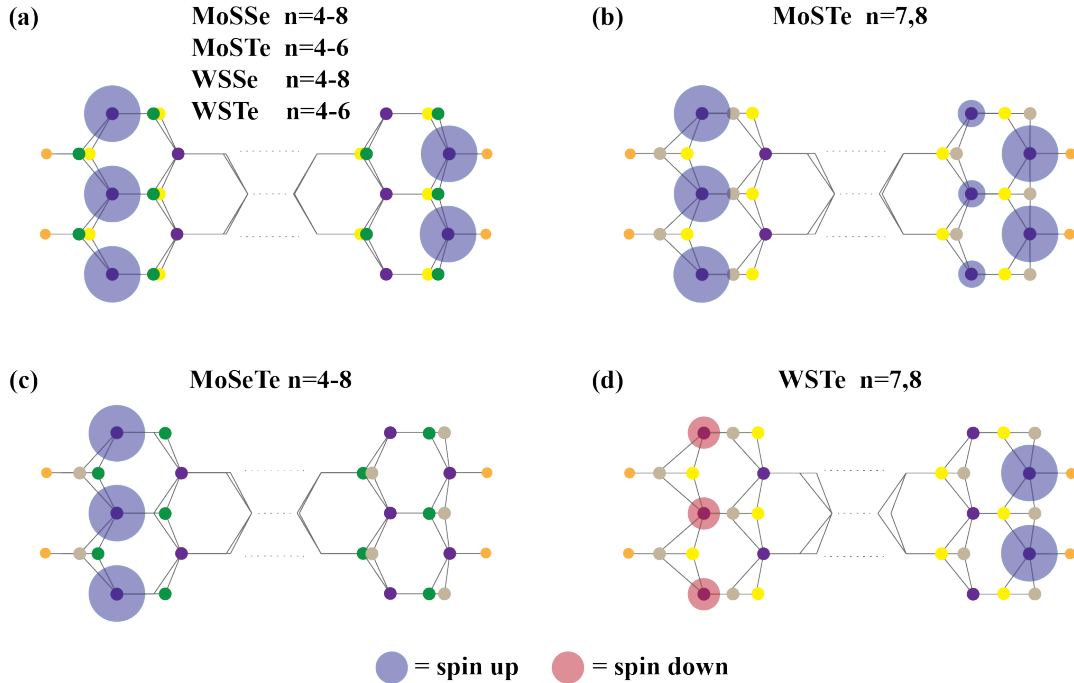


Figure 7.10. Schematic diagram of the magnetic ordering of hydrogen-passivated zigzag nanoribbons.

Notably, most ZNRs now exhibit only FM coupling between edge metal atoms, with the exception of the n=7,8 ribbons of WSTe (AFM ordering) and the WSeTe ribbons (non-magnetic). In contrast to the bare ribbons, the edge chalcogen atoms do not possess a significant spin moment and thus do not contribute to the overall magnetic moment of the ZNRs. This is expected, as the edge chalcogen atoms now have completely saturated bonds. For MoSSe and WSSe ZNRs, there is FM coupling of the Mo/W atoms on both edges (Figure 7.10a). The MoSTe ZNRs show similar FM coupling, but with linear edge reconstruction for n=4-6, and additional FM coupling

from the nearest-neighbor Mo atoms (Figure 7.10b) for $n=7,8$. The MoSeTe ZNRs only have significant FM coupling of the Mo atoms on the left edge, with linear reconstruction of the right edge (Figure 7.10c). The WSTe ZNRs of $n=4-6$ show the same FM coupling as the MoSTe $n=4-6$ ribbons. However, the $n=7,8$ WSTe ZNRs now display AFM ordering where the W atoms on the left edge have a net spin down moment, and the W atoms on the right edge have a net spin up moment (Figure 7.10d). In contrast to all other structures, the WSeTe ZNRs are non-magnetic.

There are also differences in the magnetic moments of H-passivated ZNRs, compared to their bare counterparts. Most notably, all H-passivated WSeTe ZNRs are non-magnetic. Additionally, we do not observe the magnetic moment increasing as nanoribbon width increases. Instead, they possess either a constant magnetic moment (H-passivated MoSSe, WSSe), or a magnetic moment that decreases as nanoribbon width increases (H-passivated MoSTe, MoSeTe, WSTe).

Hydrogen passivation of the ANRs changes the nature of the band gap of MoSSe and MoSTe nanoribbons from indirect to direct gaps. Additionally, the band gap of these materials increases for all ribbon widths (Figure 7.11a-b). However, for MoSeTe ANRs, the band gap decreases for all ribbon widths (Figure 7.11c). The indirect to direct gap transition observed in bare MoSeTe ANRs is still present, although this transition now occurs at $n=10$ rather than $n=8$. In contrast to Mo-based structures, the band gaps of H-passivated WSSe and WSTe ANRs do not vary greatly from their unpassivated counterparts. However, both sets of passivated WSSe and WSTe ribbons no longer show an indirect to direct gap transition with increasing ribbon width; instead, all widths exhibit direct band gaps. The H-passivated WSeTe ANRs exhibit an

indirect to direct gap transition now at $n=8$. The band gap of the WSeTe ribbons now generally decreases as ribbon width increases, unlike the bare WSeTe ANRs.

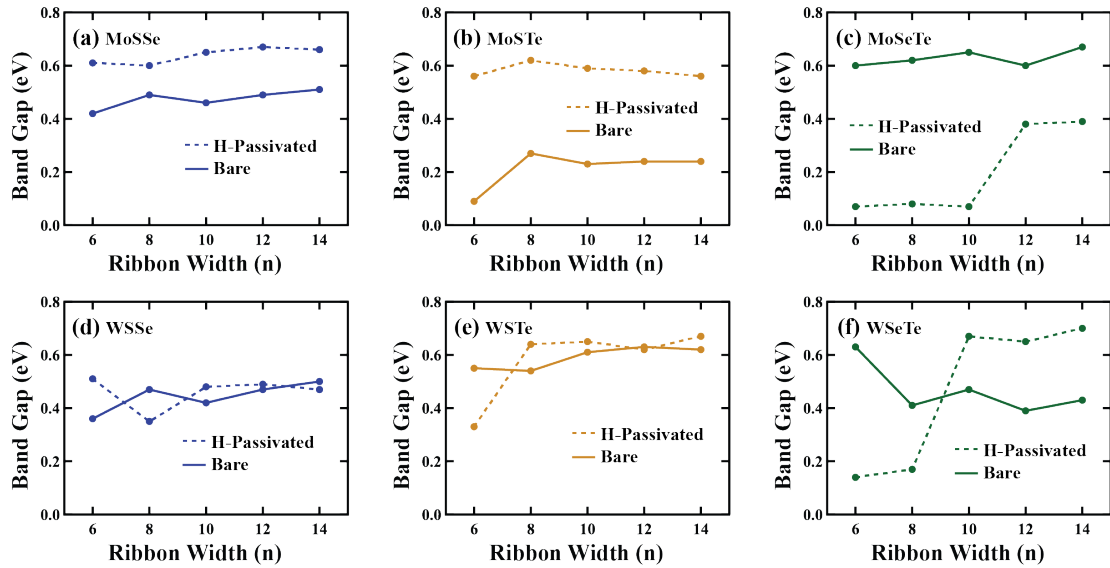


Figure 7.11. Band gaps of hydrogen-passivated and bare armchair nanoribbons.

7.4. Conclusions

We have investigated the structural, magnetic and electronic properties of Mo- and W-based Janus TMD nanoribbons of physical widths $\sim 10\text{-}20$ Å. We have found that all Janus TMD nanoribbons undergo spontaneous curvature and may also exhibit some degree of edge reconstruction. In particular, armchair-edged nanoribbons show a strong propensity for edge reconstruction. Zigzag-edge nanoribbons are metallic and magnetic, with magnetic ordering dependent on both ribbon width and atomic composition. These nanoribbons may be suitable for use in spintronic devices or as nanoscale metallic contacts. Armchair nanoribbons are either direct gap or indirect gap semiconductors, depending on the nanoribbon composition and width. Semiconducting armchair nanoribbons may find applications in nanoscale electronics such as field

effect transistors. We also investigated the effects of hydrogen passivation of the bare nanoribbon edges for zigzag and armchair nanoribbons. Hydrogen passivation stabilizes the nanoribbon edges and prevents significant edge reconstruction. Passivation also tends to stabilize the magnetic properties of the zigzag nanoribbons. Passivation of the armchair nanoribbon edges sometimes results in significant modification of the band gap value, and also tends to transform the gap character from indirect to direct. Therefore, we find that edge passivation of the armchair nanoribbons may provide a useful pathway towards tuning the nanoribbons' electronic properties.

Chapter 8. Electronic Properties of Bare and Functionalized Two-Dimensional Tellurene Structures

This chapter is based on the published manuscript Electronic Properties of Bare and Functionalized Two-Dimensional Tellurene Structures. *Phys. Chem. Chem. Phys.* **2020**, *22*, 6727.

My contributions to this work included the structural optimization and stability analysis of fluorinated Te surfaces, along with electronic structure calculations. My contributions also included calculations of bond-folding energy and *ab initio* molecular dynamics simulations of H₂, O₂, and F₂ molecules on Te surfaces. Further work from the published manuscript has been omitted from this chapter. Reproduced from Ref. [163] with permission from the PCCP Owner Societies.

8.1. Introduction

Apart from two-dimensional TMDs, 2D mono-elemental materials such as group-IV and group-VA monolayers have attracted a particular interest due to their unique chemical and physical properties.^{164–166} Among these 2D mono-elemental materials exists group-VI Tellurene (Te), which has recently been investigated theoretically and experimentally synthesized.^{167–170} High carrier mobility and significant air stability make Tellurene a promising candidate for next generation devices.^{167,170}

Theoretical studies have shown that 2D Tellurene can exist in the α -Te phase (1T-MoS₂ like) and the tetragonal β -Te phase.¹⁶⁷ It has also been shown that when the thickness decreases to $N = 8$ (where N is the number of Tellurene layers), the geometric structure of bulk Te (γ -Te) transforms into multilayered α -Te after structural optimization. In contrast to α -Te, which is obtained from a thickness-dependent phase

transition from bulk Te, β -Te occurs as a natural result of structural relaxation when the bulk Te structure is truncated along the [100] or [010] directions into thin films at the correct thickness.¹⁶⁷ The α -Te and β -Te phases possess a nearly-direct and direct band gap, respectively, which results in enhanced optical absorption properties. Both of these phases also possess higher hole carrier mobilities ($1.76 \times 10^3 \text{ cm}^2 \text{ V}^{-1} \text{ s}^{-1}$ for α -Te and $1.98 \times 10^3 \text{ cm}^2 \text{ V}^{-1} \text{ s}^{-1}$ for β -Te) than 2H-MoS₂, which has a hole carrier mobility of $0.29 \times 10^3 \text{ cm}^2 \text{ V}^{-1} \text{ s}^{-1}$.¹⁶⁷ Theoretical studies have indicated that certain structures such as square Tellurene exhibit topological insulating properties, hosting non-trivial edge states¹⁷¹ and experimental studies have confirmed that 2D α -Te exhibits topological insulating properties.¹⁷² First-principles calculations also indicate that 2D Tellurene is an excellent thermoelectric material with a high room temperature Seebeck coefficient ($S_{xx} = 0.38 \text{ mV K}^{-1}$, $S_{yy} = 0.36 \text{ mV K}^{-1}$), and an anisotropic lattice thermal conductivity ($\kappa_{xx}^1 = 0.43 \text{ W m}^{-1} \text{ K}^{-1}$, $\kappa_{yy}^1 = 1.29 \text{ W m}^{-1} \text{ K}^{-1}$).¹⁷³ Additionally, the Quantum Hall effect can be observed in few layer 2D Tellurene ($\sim 10 \text{ \AA}$ thick flakes) under high magnetic field ($\sim 5\text{-}20 \text{ T}$).¹⁷⁴

Quasi-2D structures such as high-mobility Te nanoflakes have been solution-synthesized with potential applications for shortwave infrared photodetectors (SWIR). Although these nanoflakes possess an indirect band gap, they can be utilized for SWIR photodetectors when placed on optical cavity substrates (such as Au/Al₂O₃) to increase the absorption in the semiconductor.¹⁷⁵ First-principles calculations have determined that by applying strain, phase transitions and mechanical property modulations can be induced in 2D Tellurene.^{176,177} Recently, the effects of adatoms and gas molecules such as H₂, O₂, NO₂, H₂O, and NH₃ on the surface of α -Te and β -Te monolayers at dilute

doping concentrations have been theoretically studied and the effects on the electronic structure have been reported.¹⁷⁸ The results of this study indicate that while most adatoms are chemisorbed on Te sheets with large adsorption energies, some adatoms such as Ca, Fe, Co, and Ni give rise to structural deformations and local reconstructions which result in different induced electronic structures. These calculations also show that all considered gas molecules are physisorbed on Te sheets and have a weak effect on the electronic structure.¹⁷⁸

Previous studies have also indicated that functionalization by dense doping of impurities can tune the electronic properties of certain 2D materials.^{179–184} For example, σ -character Dirac cones can be engineered in phosphorene (2D phosphorous) when the material is single- and double-side hydrogenated and fluorinated.¹⁸¹ Similarly when 2D monolayer arsenic (arsenene) is hydrogenated, the same σ -type Dirac cones have been predicted.¹⁸² Theoretical studies also indicate that the oxidation of 2D antimony (antimonene, an indirect semiconductor), can tune the band gap to direct and widen the band gap value depending on the concentration of oxygen added.¹⁷⁹ Interesting electronic properties arise when group-III monochalcogenides, which possess wide band gaps in the visible region (2.04–3.47 eV), are functionalized with oxygen atoms. After oxygen functionalization, the band gaps of these group-III monochalcogenides decrease (under 1 eV). Double-site oxygen functionalization causes InS, InSe and InTe to become 2D topological insulators with sizable band gaps (up to 0.21 eV).¹⁸⁵

In this study, motivated by how hydrogenation, oxidation and fluorination modify the properties of certain other 2D materials,^{179–184} we investigated the stability, structural and electronic properties of 2D bare and functionalized Tellurene structures

using density-functional theory (DFT) and ab-initio molecular dynamics (MD) calculations within the projector augmented-wave method.^{72,73} For bare 2D α -Te and β -Te sheets, we calculated band gaps of 0.44 eV and 1.02 eV, respectively. When functionalized with H, O, and F atoms, the band gaps of 2D α -Te and β -Te decrease and the structures become metallic except hydrogenated β -Te, which remains semiconducting, but now has a band gap of 1.37 eV. From our phonon dispersion and MD simulations, we found that oxygenated β -Te is stable and hydrogenated β -Te is meta-stable. We also report that H, O, and F functionalization fully disrupts the structure of α -Te. Additionally, H and F functionalization causes the β -Te layers to separate into functionalized chains, and O causes a total structural transformation of β -Te to a Te_3O_2 -like structure. To investigate these structural changes further, we calculated the binding/dissociation energies of single H, O and F atoms and single H_2 , O_2 , and F_2 molecules on monolayer α and β -Te. To gain an understanding of how adatom coverage effects the stable Te structures, we varied the H and O coverage of bare β -Te and found that fully functionalized O- β -Te and H- β -Te have the strongest adatom binding energies. We also performed MD simulations for high coverage of H_2 , O_2 , and F_2 (6-8 molecules on each side) on the α and β -Te surfaces. To extend our simulations to more realistic systems, we studied the effects of the stable functionalized Te structures (O- β -Te and H- β -Te) on a GaSe substrate. We found that the stability of layered Te structures are enhanced since these structures bind strongly to GaSe surface and remain intact. Our results confirm that 2D Tellurene structures are excellent candidates for metallic contacts in nanoscales junctions and are suitable for next generation optoelectronic devices.

8.2. Computational Details

Our theoretical calculations were obtained via first-principles pseudopotential calculations based on spin-polarized density functional theory within the generalized gradient approximation (GGA), and including van der Waals (vdW) corrections using the DFT-D2 method¹⁸⁶ and spin-orbit coupling (SOC) effects. We used projector augmented-wave (PAW) potentials and approximated the exchange-correlation potential with the Perdew-BurkeErnzerhof (PBE) functional.^{66,72} The Vienna ab initio simulation package (VASP) code was used for numerical calculations.⁷³ The kinetic energy cutoff of our plane-wave basis set was taken to be $\hbar^2|\mathbf{k} + \mathbf{G}|^2/2m = 450$ eV. The Monkhorst-Pack scheme was used to sample the Brillouin zone (BZ) using a $20 \times 20 \times 1$ mesh in k space for 2D structures.⁶⁸ The number of k-points was scaled accordingly with the size of the supercell in our simulations. Atomic positions were optimized using the conjugate gradient method, where the total energy and the atomic forces were minimized. A maximum force of 0.01 eV/Å was allowed on each atom and the energy convergence value between two consecutive steps was chosen to be 10^{-5} eV. The vacuum spacing between periodic layers was set to at least 20 Å to minimize interlayer coupling. The Gaussian-type Fermi-level smearing method is used with a smearing width of 0.01 eV. Self-consistent field calculations of the electronic band structure and the total and orbital projected density of states (with the smearing width increased to 0.05 eV) were carried out including SOC effects. The cohesive energy of each structure is obtained by the expression $E_{coh} = (nE_{Te} + mE_{atom} - E_{2D-Te})/(n + m)$, where E_{Te} , E_{atom} and E_{2D-Te} are the isolated total energy of the free Te atoms, the isolated total energy of the functionalization atoms (H, O, F) and the total energy

of the bare/functionalized 2D Te structures respectively. The number of Te atoms and adatoms in the cell are labeled as n and m , respectively. The phonon dispersion curves were obtained using the finite-displacement method ($4 \times 4 \times 1$ supercell for α -Te, $4 \times 3 \times 1$ for β -Te) implemented in the PHONOPY code.¹⁸⁷ In phonon dispersion simulations, SOC effects are excluded due to computational limitations. For single atom and molecule adsorption simulations we used a $4 \times 4 \times 1$ supercell for α -Te and a $4 \times 3 \times 1$ supercell for β -Te. The thermal stability of our optimized structures was also tested using finite-temperature *ab initio* molecular dynamics simulations at 300 K and 600 K with a time step of 0.5 fs. These simulations were run at time scales of 3-8 ps and used the Nosé-Hoover thermostat to obtain the canonical (NVT) ensemble. Bader charge analysis was used to obtain the charge distribution on the atoms in our simulations.^{188,189} The VESTA program was used to visualize of the atomic structures.¹⁹⁰

8.3. Results and Discussion

8.3.1. Bare 2D Te

Bulk Tellurium (γ -Te) has a space group of $P3_121$. The unit cell of γ -Te contains three two-fold coordinated Te atoms that form helical chains parallel to the c-axis with a bond distance of $d_{Te-Te} = 2.89 \text{ \AA}$. The calculated lattice parameters of γ -Te are $a = b = 4.34 \text{ \AA}$, $c = 6.02 \text{ \AA}$ and the structure is depicted in Figure 8.1. As the number of Te layers decreases in the γ -Te, the helical chains become closer together and the structure turns to α -Te with a space group of $\bar{P}3m1$. The decreased distance between helical chains results in a bond distance of $d_{Te-Te} = 3.02 \text{ \AA}$ with lattice parameters of

$a = b = 4.15 \text{ \AA}$. Another stable form of Tellurium known as β -Te (Figure 8.1) has space group P2/m. This structure arises from the cutting of Te-Te bonds in bulk γ -Te along the [100] or [010] direction. This results in two bond distances of $d_{\text{Te-Te}} = 2.76 \text{ \AA}$ and $d_{\text{Te-Te}} = 3.02 \text{ \AA}$ with lattice parameters of $a = 4.17 \text{ \AA}$ and $b = 5.47 \text{ \AA}$. The van der Waals (vdW) radius of Tellurium is 2.06 \AA and the average bond distance of our present structures is $\sim 2.9 \text{ \AA}$. A purely van der Waals interaction would have bond lengths of $\sim 4.1 \text{ \AA}$, so this implies there is stronger bonding between Te atoms including metal-ligand multiple and covalent bonds.

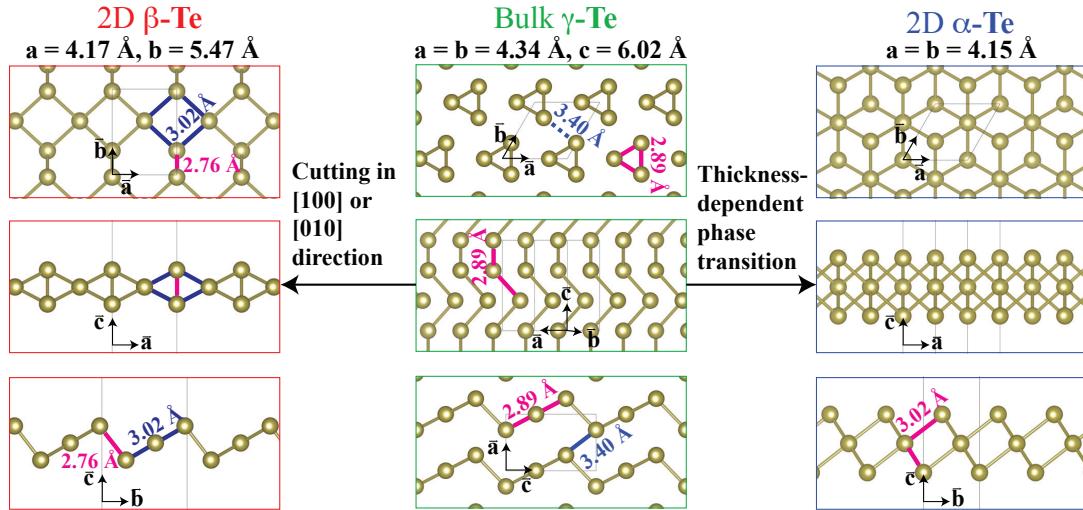


Figure 8.1. Top and side views of the helical chain structure of bulk γ -Te (middle column), the rectangular structure of monolayer β -Te (left column), and the hexagonal structure of monolayer α -Te (right column), respectively. Bond lengths (represented by pink and blue lines), lattice parameters and interchain distances are given in the insets.

Monolayer β -Te has both three-fold and four-fold bonds and α -Te has three-fold and six-fold bonds, whereas bulk γ -Te has twofold bonds (inside chains). Increasing from two-fold bonds to higher bond order results in a decrease in cohesive energy of the Te structures and bond strength and an increase in bond length. For instance, calculated cohesive energy with (without) SOC of γ -Te is 2.35 (2.80) eV/atom, while

this value is 2.26 (2.63) and 2.23 (2.58) eV/atom for 2D α -Te and β -Te (on average) monolayers, respectively. In order to relate bond energy to the number of fold bonds, we calculated bond breaking energy for all 2D-Te structures with SOC. For γ -Te in which all the bonding in the chain-like structure is the same and covalent in character and weak interaction between chains, bond energy is calculated as 0.97 eV/bond (calculated by $(d \cdot E_{coh} - E_b)/(n \cdot d)$ where n is the number of folding of bonds, d is the number of Te atoms in the primitive cell and E_b is the interchain binding energy which will be discussed in the upcoming subsection). For α - and β -Te, we calculate the bond energy of the n -fold bonds as $E_{BE} = (E_{vac} + E_{Te_{coh}} - E_{2D})/n$, where E_{2D} is the energy of the pristine 2D layer, E_{vac} is the energy of the vacancy-containing layer, and $E_{Te_{coh}}$ is the cohesive energy of a Te atom obtained from γ -Te. For α -Te, there exists a metalligand-like bonding between the central atom (six-fold) and the outer atoms (three-fold). The bond energy of the three-fold and six-fold bonded Te atoms in α -Te are 0.75 eV/bond and 0.62 eV/bond, respectively. For the β -Te monolayer, the outer atoms have three-fold bonding: two with a metal-ligand-like bonding with two neighboring central atoms and one with a strong σ bonding between upper and lower atoms. The central atoms have four metal-ligand-like bonding to the neighboring outer atoms. The average bond energy of the three-fold and four-fold bonded Te atoms in β -Te are 0.77 eV and 0.66 eV, respectively. From these calculations, we conclude that Te atoms prefer to bond with lower bond order which results in lower bond length and higher cohesive energy per bond.

For the sake of comparison with the literature, we also calculated the electronic band structures of bare Te structures. Our calculations indicate that γ -Te has an indirect

band gap of 0.31 eV, while β -Te has an indirect band gap of 1.17 eV and α -Te has an indirect band gap of 0.76 eV. Similar to other mono-elemental materials from the fifth row of the periodic table such as Sb,¹⁹¹ SOC becomes dominant in the electronic band structures of Te materials because of an increase of *d*-orbitals in Te atoms.¹⁶⁷ As a result, SOC decreases these band gap values by 0.15 eV for β -Te and 0.32 eV for α -Te and turns them to direct gap semiconductors as shown in Figure 8.2. These values are comparable with previous theoretical results.¹⁶⁷

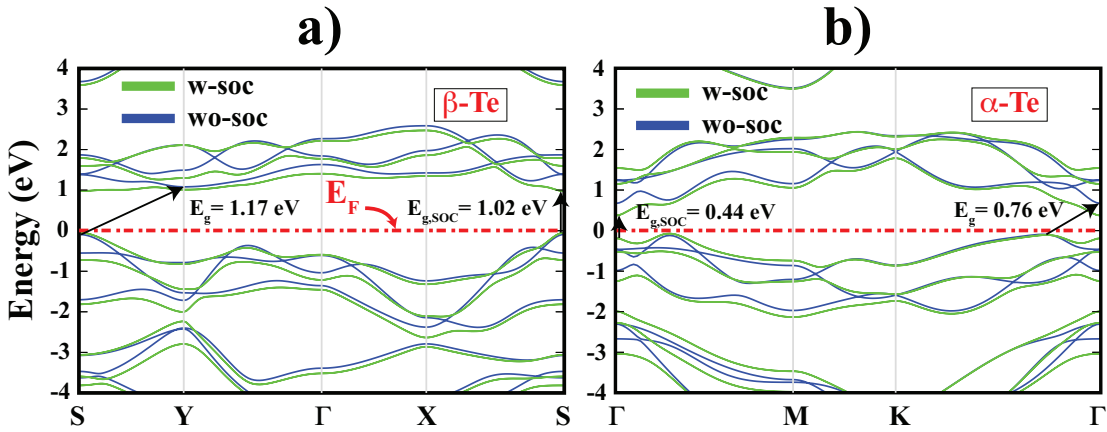


Figure 8.2. The electronic band structure of bare a) β -Te and b) α -Te with (green) and without (blue) spin-orbit coupling (SOC) effects.

Because of these significant changes to the electronic structure when SOC is taken into account and due to the heavy atomic mass (atomic number) nature of Te atoms,¹⁶⁷ we carried out all numerical calculations (except phonon dispersion curves due to computational limitations) including SOC effects. A full description of the underlying physics of SOC in Te-based materials can be found in the following references [167,171,192–194].

In addition to SOC, we also employed vdW corrections to the energy in all of our simulations. Although it is a common misconception that vdW corrections are only needed in multi-layer/bulk systems, monolayer materials require this correction to

correctly describe the long-range interactions. This is especially needed in 2D Te structures, where functionalization causes the structure to either separate into chains or layers (this will be discussed in detail in the next subsection). This separation results in a weak vdW interaction between the chains/layers that requires a correction to the energy.

8.3.2. Functionalized 2D Te Structures

8.3.2.1. Modification of atomic structure upon functionalization

Functionalized 2D Tellurene structures may exhibit different properties than their bare 3D bulk and 2D counterparts. Therefore, to investigate the effects of the functionalization of α - and β -Te monolayers at high adatom concentrations, we placed H, O, or F atoms 2 Å above each outer Te atom in the primitive cell and performed geometric optimization calculations. Figure 8.3 shows the cohesive energies of all the considered H, O, and F α - and β -Te structures as a function of lattice constant (for the \vec{a} direction). All functionalized structures except O- β -Te have a local minimum and a global minimum at different lattice constant values. All global minima structures indicate that functionalization results in a decrease of the lattice constant.

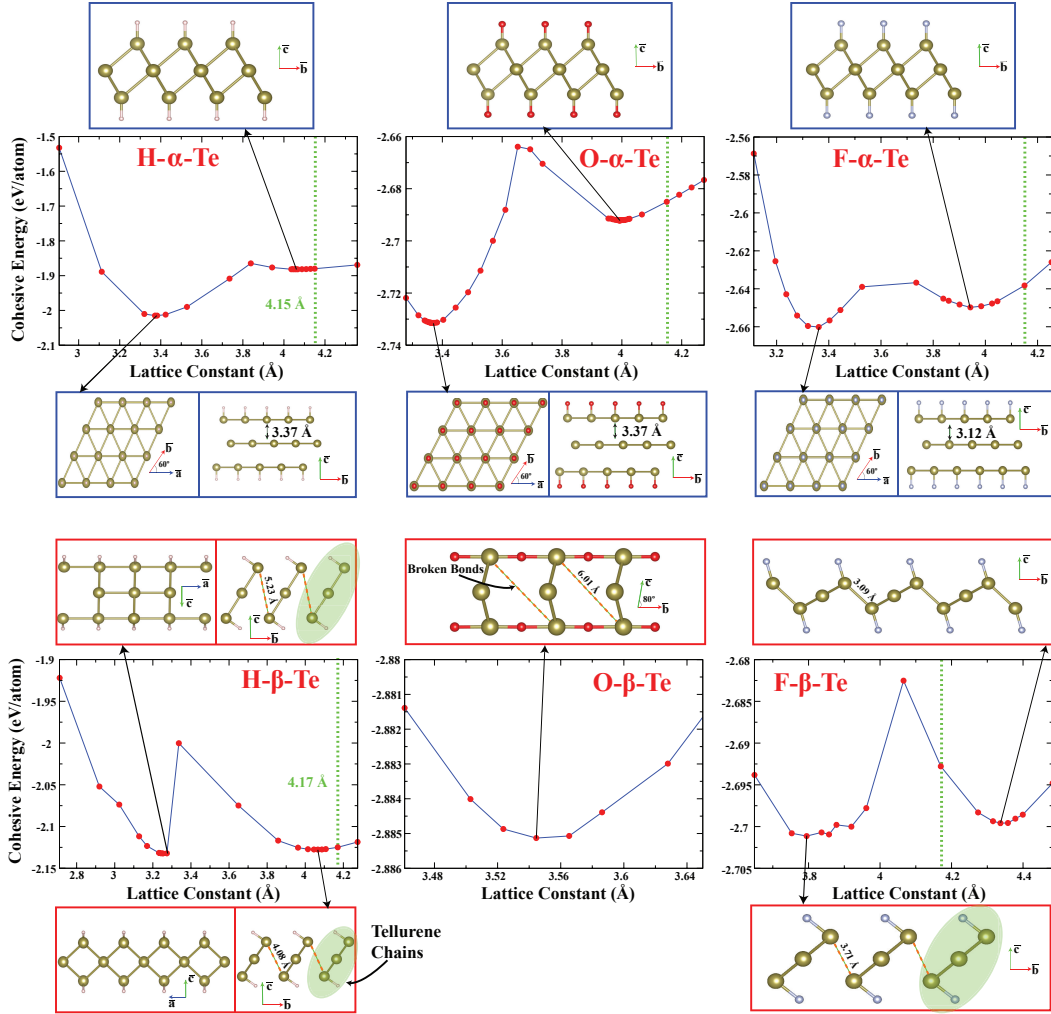


Figure 8.3. The cohesive energy (in eV per atom) as a function of lattice constant (for the a-direction) for 2D β -Te functionalized with H, O, and F. We observe one local and one global cohesive energy minimum for all functionalized structures except O- β -Te, which contains a single global minimum. The optimized geometry of the functionalized Tellurene structures at each minimum are depicted above and below the corresponding energy landscape. Bond breaking for O, H and F- β -Te is indicated by the orange dashed lines. The green dashed lines represent the lattice constant (in the a-direction) for bare monolayer α -Te and β -Te, respectively.

For all the functionalized α structures, the bare α -Te shape is preserved at the local minimum while the Te layers separate at the global minimum with an average c distance of 3.29 Å between each layer (as compared to an interlayer distance of ~ 1.8 Å for bare 2D α -Te). The compression of the lattice constants along the a and b -axes lead to stronger nearest-neighbor interactions between Te atoms in the same plane. This change in bonding environment leads to a separation of the layers along the c -axis (out

of plane movement of the surface Te atoms), which results in a new charge distribution in the structure. Bader analysis indicates that, for the H- α -Te at the local minimum, both H atoms accept 0.23 electrons (e^-) from the Te atoms. The outer (surface) Te atoms donate 0.19 e^- each and the inner Te atom donates 0.09 e^- . However, for the H- α -Te at the global minimum, the inner Te atom takes 0.20 e^- from the outer Te atoms. Therefore, the inner Te layer becomes negatively charged and this charge transfer results in polarization between Te layers. The calculated charge transfer values are higher for O and F functionalization. Each O atom takes 0.80 e^- and each F atom takes 0.61 e^- from the outer layer of Te atoms at the respective local minimum. These values are slightly lower for the global minimum of each structure because the inner Te atoms also accept electrons from the outer Te atoms. The effects of lattice compression and modification of charge transfer between Te layers on the electronic structure of Te monolayers will be discussed in the further subsections.

The functionalization of β -Te structures results in different structural changes when compared to that of α -Te. For H- β -Te, functionalization causes the strong covalent bond between outer Te atoms to break (as highlighted by orange dashed lines in the Figure 8.3 insets) at both minima. This causes the structure to change drastically at the global minimum to one composed of parallel, planar H-Te chains extending along the a-axis. These chains are highlighted with green ellipses in Figure 8.3. However, we note that there is a negligible difference in cohesive energy between the local and global minima of H- β -Te of only 4 meV/atom. We attribute this to both structures at each minimum having a H-Te chain structure with only slightly different chain-chain distances (both are larger than twice of Te atoms vdW radius) and angles between the

c-axis and a-b plane. F- β -Te exhibits a similar structural transition as H- β -Te. Since the functionalized chains are weakly bonded, the Bader charge analysis report similar charge distribution in both chain structures. H and F atoms get charges from outer Te atoms and negatively charged by ~ 0.17 and ~ 0.62 electrons, respectively.

To further analyze the chain-like nature of the H- and F- β -Te structures, we calculated the interchain binding energies and compared the values to that of γ -Te, which is proposed to be formed of covalently bonded chains.¹⁹⁵ The interchain binding energy is defined as $E_b = E_{chain} - E_{Te}$ where E_{chain} is the total energy of the isolated functionalized H- or F-Te chain and E_{Te} is the total energy of the functionalized 2D β -Te structures (at the local or global minima). The calculated E_b for the bulk chain structure (γ -Te) is 1.26 eV, which is in good agreement with the literature.¹⁹⁵ In contrast, we find values for H-Te of $E_b = 0.24$ eV at the local minimum and 0.27 eV at the global minimum. For F-Te, $E_b = 0.31$ eV at the local minimum and 0.32 eV at the global minimum. These values are lower than that of γ -Te and thus indicate weak chain-to-chain interaction in hydrogenated and fluorinated β -Te. They also support our discussion why local and global minimum structures are energetically very close and the chains are bonded dominantly by vdW interaction.

Oxidation of Te results in a different structural transformation for β -Te. For O- β -Te, the O atoms break the Te-Te bond, penetrate into the Te layers, and bond to the outer two Te atoms, resulting in a Te₃O₂-like structure. This structural transformation results in a buckling of Te atoms on the c-axis with a singular global minimum. The highest amount of charge transfer ($1.07 e^-$ from Te atoms to the O atoms) occurs with

this structural transformation. For this new structure, inner site Te atoms also lose 0.12 e^- and donate to O atoms.

8.3.2.2. Stability analysis

It has previously been stated that two methods to filter out stable 2D materials include the calculation of the phonon dispersion relation for the whole BZ and ensuring there are no negative frequencies and performing an *ab-initio* molecular dynamics (MD) simulation to test dynamical stability at finite temperatures.¹⁹⁶ Applying just one of these filters cannot guarantee stability, but using both in conjunction with one another can provide strong insight to whether or not a 2D structure is stable.

To investigate the stability of the functionalized α and β structures at each minimum, we first performed phonon calculations. Obtained phonon dispersion curves indicate that O- β -Te has positive phonon frequencies for the whole BZ (Figure 8.4b). For H- β -Te, we observe that the local minimum contains few negative frequencies (Figure 8.4a).

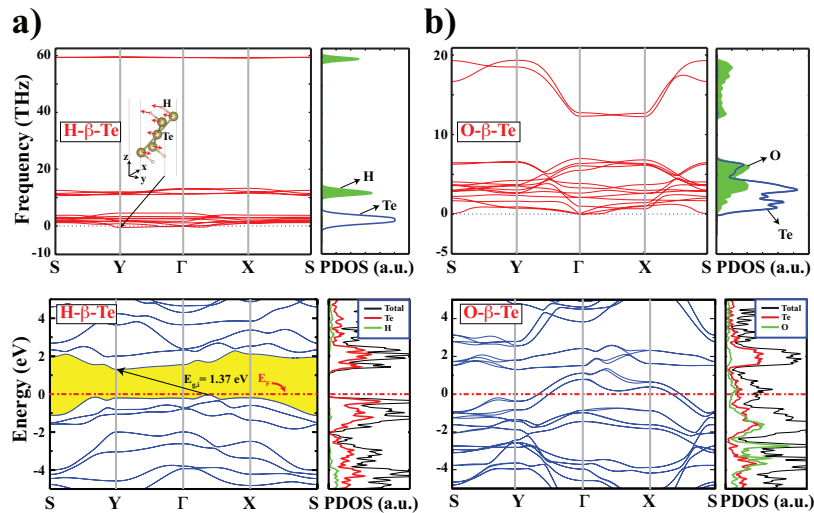


Figure 8.4. The phonon band structure and phonon projected density of states (PDOS), in addition to the electronic band structure and orbital projected density of states (PDOS) of (a) H- β -Te at its local energy minimum and (b) O- β -Te at its singular global energy minimum. For H- β -Te, the atomic movements at the negative frequency at the Y high symmetry point are shown (red arrows depict the vibration direction).

The atomic movements and the phonon partial density of states (PDOS) indicate that the instability is not related with the Te-H bonds, but due to the breaking of strong covalent bonding between outer Te atoms. The lack of restoring force for the rotation of Te_3H_2 chains causes the instability. Similar instability is also observed for the global minimum H- β -Te structure. This slight instability can easily disappear if the H- β -Te structure is placed on a suitable substrate such as graphene, Cu, Ni, Pt, GaS, or GaSe.^{168,197,198} Recently, Yang et al. showed that bare Te sheets can be synthesized on GaSe substrates and that they are well-oriented along the GaSe armchair lattice direction.¹⁹⁸ Theoretically and experimentally, it has also been proposed that Tellurene monolayers can be stabilized by CdTe interfaces.¹⁹⁹ The remaining phonon dispersion curves indicate that F- β -Te and all functionalized α structures are unstable due to the presence of a larger number of negative phonon frequencies (Figure 8.5).

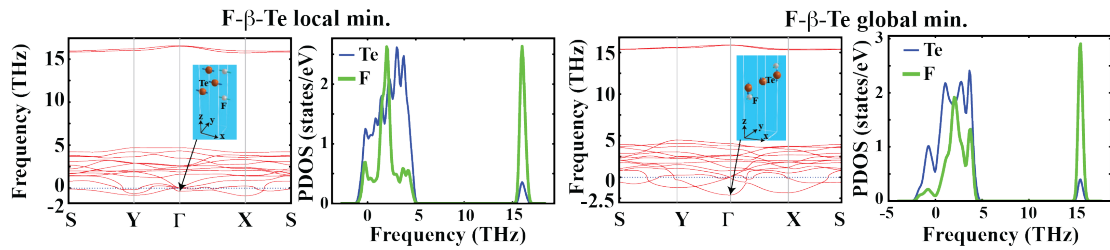


Figure 8.5. The phonon dispersion curves and phonon projected density of states (PDOS) of the F-functionalized α -Te and β -Te structures at the local and global minima. These dispersion curves and PDOS plots indicate that these structures are unstable in free standing form. Atomic movements for certain negative frequencies at the special high symmetry points are given in the insets.

As discussed in the previous section, F adatoms withdraw significant electrons from the α -Te structure and at global minimum structures, they result in separation of Te layers. For F- α -Te, both the local and global minima have five negative frequency bands that are a mixture of acoustic and optical modes. The global and local minima for F- β -Te feature negative acoustic modes spanning the whole BZ. In addition to

weakening of the covalent bonding between Te atoms on the outer edges like H- β -Te, F adatoms are destabilizing the structure by out-of-phase vibrations (Figure 8.5).

To further examine the stability of the structures which contained negative phonon frequencies, we performed MD simulations at a finite temperature of 300 K and a time scale of 3 ps with a time step of 0.5 fs. After 3 ps, we observed significant disruption of the structures, which confirm our stability calculations. For O- β -Te, we observe no disruption to the structure with the O atoms oscillating in the c-direction. For H- β -Te at the local minimum we observe no disruption until 2 ps and minimal disruption after 3 ps, with some H dissociating from the surface. This might signify that at lower H atom doping concentrations on Te monolayers, functionalized structures can be stable. Since O- β -Te and the local minimum of H- β -Te both satisfy the phonon and dynamical stability tests (aside from the small negative frequency of H- β -Te that can be lifted by a substrate), we can say with confidence that these two structures are stable.

8.3.2.3. Electronic Properties of Functionalized 2D Te

For all the structures considered, we calculated the electronic band structures and partial density of states (PDOS) with spin orbit coupling effects. The band structures and corresponding PDOS of the structures that contain negative frequencies in the phonon dispersion curves (unstable structures) are shown in Figure 8.6.

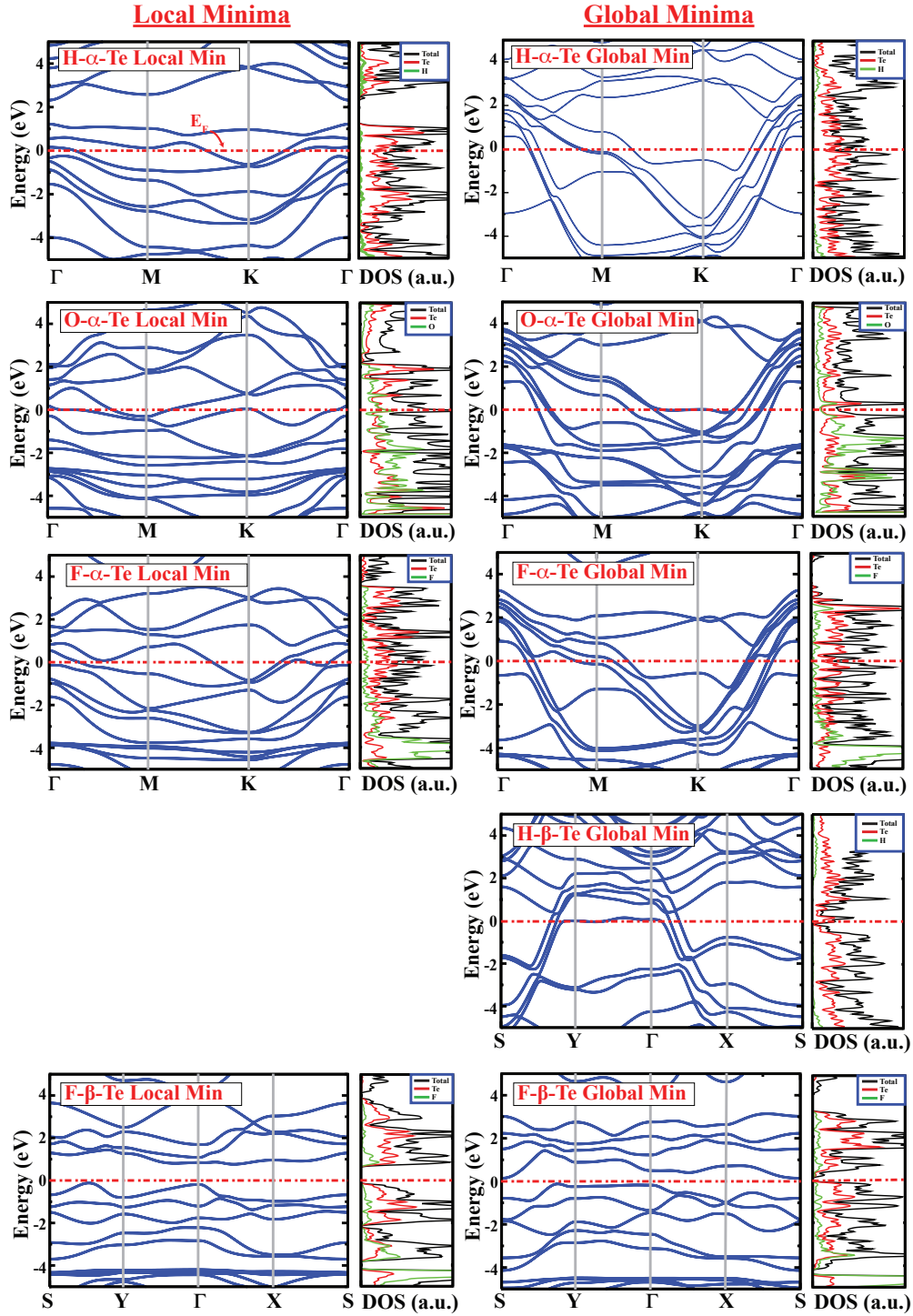


Figure 8.6. The electronic band structures and orbital projected density of states (PDOS) of functionalized Te structures at their local minimum and global minimum.

Although the cohesive energy difference between the local and global minima of H- β -Te is very small, the structural differences between these two minima have a significant effect on the electronic band structure. At the local minimum we observe an indirect band gap of 1.37 eV (Figure 8.4a), while at the global minimum H- β -Te has metallic characteristics (Figure 8.6). The metallic channel in the global minimum originates from the shortened middle layer Te bonds which provides further evidence for the dual character of Te bonds.¹⁶⁷ At the local minimum we see the valence band maximum (VBM) shift away from the Γ point and toward the X point (when compared with the band structure of bare β -Te). However, the conduction band minimum (CBM) remains at the same high symmetry point (Y). From the PDOS we see that the 1s H orbitals are mainly located below -4 eV. The VBM and CBM are dominated by p orbitals of Te.

In Figure 8.4b we see that fully oxygenated Te has a metallic character and oxygen p states give a similar contribution as Te p states. The amount of charge transferred from Te to O is much larger than the charge transferred from Te to H in H- β -Te (local min.) and we have significant charge accumulation around the embedded O atoms and a significant charge depletion around the outer Te atoms. This considerable transfer of electrons from outer Te atoms to O provides a viable explanation to why O functionalization causes such a significant structural transformation to a Te₃O₂-like structure. Even though the metal-ligand-like bonding between the middle and outer Te atoms are preserved, outer Te and O atoms have ionic bond character instead of the strong covalent bonding between upper-lower Te layers. This ionic bonding between Te and O results in states around the Fermi level. Because O- β -Te is a stable form of

metallic 2D Tellurene, it is suitable for metallic contact applications in nanoscale junctions. The additional O- α -Te band structures and PDOS at the local and global minima in Figure 8.6 are also metallic, which proves that oxygen functionalization causes all Te structures to become metallic.

8.3.3. Single atom and molecule binding

After phonon calculations revealed the stability of functionalized Te structures, we calculated the binding energy and bonding geometry of single H, F, and O atoms on the top Te site of α - and β -Te to obtain a deeper understanding of how adatom impurities interact with the Te surface. We also investigated the effects of single-molecule interaction of H₂, F₂, and O₂ with the bare α and β -Te surfaces. For these calculations, we used a 4 \times 4 \times 1 supercell for α -Te and a 4 \times 3 \times 1 supercell for β -Te. We calculated the binding energy of the adatom (and H₂, F₂, and O₂ molecules) as $E_{binding} = (E_{Te+A,M} - E_{Te} - nE_{A,M})/n$, where $E_{Te+A,M}$ is the total energy of the Te sheet and the atom (A) or molecule (M) together, E_{Te} is the total energy of the bare Te sheet, $E_{A,M}$ is the total energy of the isolated atom or molecule, and n is the number of adatoms. The binding energies and charge transfer values are compiled in Table 8.1. We find that H, F, and O atoms bind directly above the Te atom top site of α -Te. However, for β -Te the H, F, and O atoms bond off center from the Te top site. For dilute concentration where adatom-adatom interactions are excluded, one can report that the dominant interaction is between the adatom and the nearest Te. Bond lengths, charge transfer values and binding energies show similar trend for both Te layered structures.

Table 8.1. The binding or dissociation energies ($E_{binding/diss}$) of single H, O and F atoms and single H₂, O₂, and F₂ molecules on α and β -Te. The * indicates dissociation energy. Values of charge transferred to each adatom/molecule calculated from Bader charge analysis are also given.

Structure	$E_{binding/diss}$ (eV)	Bond length (Å)	Charge transfer (e^-)
H on α -Te	-1.01	1.72	0.22
O on α -Te	-3.15	1.85	0.91
F on α -Te	-3.02	2.04	0.68
H on β -Te	-1.37	1.70	0.20
O on β -Te	-3.52	1.85	0.92
F on β -Te	-3.44	2.04	0.69
H ₂ on α -Te	-0.02	3.38	0.00
O ₂ on α -Te	-0.09	3.28	0.03
F ₂ on α -Te	1.86*	—	0.66
H ₂ on β -Te	-0.01	3.04	0.00
O ₂ on β -Te	0.10	2.95	0.04
F ₂ on β -Te	2.42*	—	0.64

To simulate single-molecule binding, we placed the molecule 2 Å above the bare Te surfaces and relaxed the structure (Figure 8.7). Single H₂ and O₂ molecules placed on one side of the α - and β -Te surfaces do not disrupt the Te structures and are physisorbed on the surface. There is not significant charge transfer resulting from this physisorption.

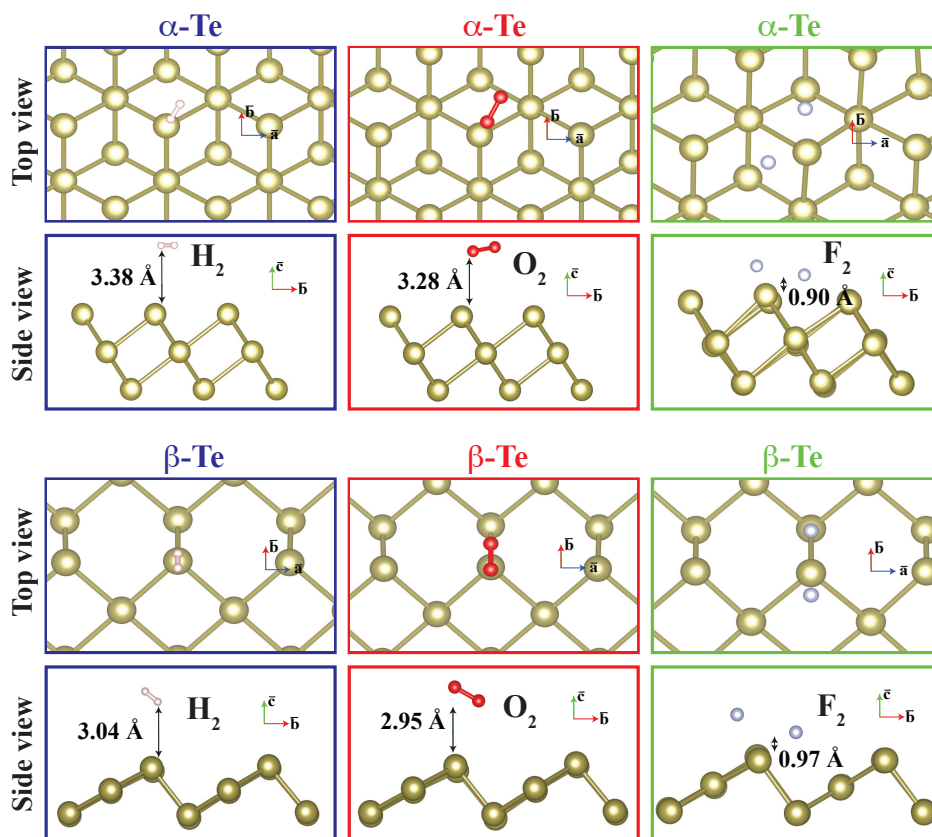


Figure 8.7. The optimized geometry of 2D α and β -Te when single H_2 , O_2 and F_2 molecules are initially placed 2 Å above the surface.

In contrast, F_2 molecules dissociate on both the α - and β -Te surfaces. From this, we can infer that Te monolayers react strongly with fluorine. This conclusion is further supported by simulations of exposure of one or both sides of the Te structures to many F_2 molecules. MD simulations for these cases result in the destruction of the Tellurene layer (Figure 8.8).

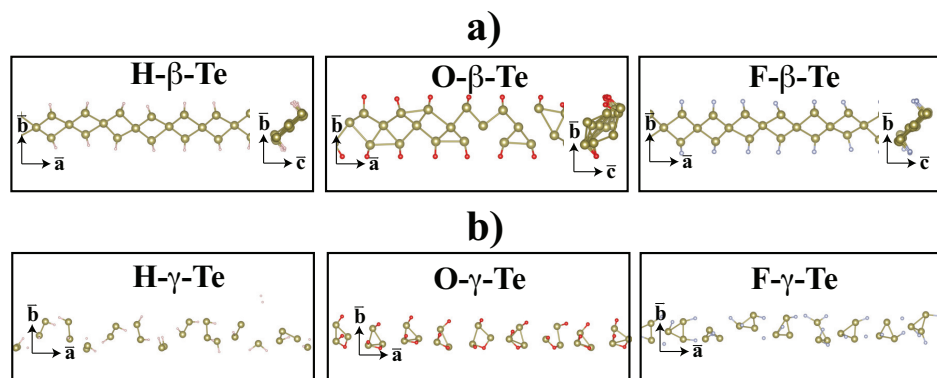


Figure 8.8. Initial and final (after 2 ps) snapshots of MD calculations at 300 K for high coverage of H₂, O₂, and F₂ molecules above the surface of a) α -Te and b) β -Te.

Because F₂ molecules dissociate on the Te surface, we instead calculated the dissociation energy for F₂ as $E_{diss} = E_{binding,F_2} - 2E_{binding,F}$ where $E_{binding,F_2}$ is the binding energy of a single fluorine molecule and $E_{binding,F}$ is the binding energy of a fluorine atom. The positive valued dissociation energy is 1.86 eV for α -Te and 2.42 for β -Te, indicating that the dissociation of F₂ on either Tellurene surface is exothermic.

We extended our studies of Tellurene interaction with molecular hydrogen, oxygen, and fluorine by considering high coverage of H₂, F₂, and O₂ molecules placed on one or both sides of the α and β -Te surfaces. We placed 8 molecules per side of a 4×4×1 supercell of α -Te and 6 molecules per side of a 4×3×1 supercell of β -Te, which results in coverage of $\sim 2 \times 10^{14}$ cm⁻² per side. Initially, molecules were randomly placed 2 Å above the bare Te surface. We performed MD simulations of these systems at 300 K with a timestep of 0.5 fs for 2 ps. As mentioned previously, F₂ molecules disrupt both α and β -Te monolayers. H₂ molecules interact weakly with either Tellurene surface, with only a few molecules interacting via physisorption. For α -Te and β -Te, high concentrations of O₂ cause minor structural deformation of the Tellurene layer. From

these results, we can confirm that α and β -Te remain intact against H_2 and O_2 molecules while they are disrupted by F_2 .

8.4. Conclusions

We have provided a comprehensive study of the electronic properties of 2D Tellurene structures including bare and functionalized (with H, O, and F) α - and β -Te monolayers. We find that functionalization results in significant structural changes for monolayer Te such as disruption of the structure of α -Te by H, O, and F; separation of β -Te into functionalized chains by H and F; and the complete transformation of β -Te into a metallic Te_3O_2 -like structure by O. The functionalization of these α and β -Te monolayers also result in metallic properties for all structures except H- β -Te, which has a band gap of 1.37 eV and can be utilized for devices in the near infrared range. Coverage results indicate that fully functionalized H- β -Te and O- β -Te have the strongest adatom binding energies. These results, in addition to the recent experimental progress in synthesizing Te structures, prove that bare and functionalized 2D Te structures are viable candidates for next generation optoelectronic devices and can be used as metallic contacts in nanoscale junctions.

Chapter 9. Conclusions

This work has investigated, both experimentally and theoretically, several two-dimensional materials for device purposes. One key focus of this work was the integration of high-k dielectric films with MoS₂ via atomic layer deposition. This work extended our knowledge of how the starting surface of MoS₂ affects the quality of the film growth. Further studies investigated surface engineering techniques to improve ALD on MoS₂. Finally, this work branched out to study the properties other novel 2D materials and their applicability for electronic device purposes. This chapter summarizes the key findings of these studies.

9.1. Atomic Layer Deposition of Al₂O₃ and TiO₂ on MoS₂ surfaces

The quality of the starting surface of MoS₂ is crucial to the success of ALD on this material. This study found that mechanically exfoliated surfaces exhibit a high degree of variability, and thus the surface coverage of ALD films is variable and unpredictable. These variations likely arise from a combination of contamination and differences in intrinsic defect concentration. CVD-grown MoS₂ monolayers were found to have more consistent starting surfaces and thus provide a reliable starting point for further studies of ALD film growth on MoS₂.

9.2. Surface Defect Engineering of MoS₂ for Atomic Layer Deposition of TiO₂ Films

In this chapter, it was determined that reactive sulfur vacancies are the most likely pathway for seeding ALD growth of TiO₂ on MoS₂ using TDMAT and water precursors. A high density of sulfur vacancies results in continuous films that are free

of pinholes. However, sulfur vacancies introduce localized states into the band gap, degrading the electronic properties of the material. It is possible to further modify the electronic properties of defective MoS₂ using thiols such as mercaptoethanol. This chapter provides further insight into the growth mechanisms of ALD films on MoS₂ as well as possible pathways for tuning its electronic properties.

9.3. Spontaneous Curvature of Janus Transition Metal Dichalcogenide Nanoribbons: Effects on Optoelectronic, Magnetic and Mechanical Properties

Modification of the properties of two-dimensional materials can be extended by reducing dimensionality. In this chapter, nanoribbons of Janus transition metal dichalcogenides were studied using density functional theory. Freestanding nanoribbons were found to spontaneously curve as a result of the mismatched strain between the top and bottom sides. The zigzag nanoribbons are metallic and magnetic, while armchair nanoribbons are semiconducting. The properties of these nanoribbons can be tuned by adjusting their width, and also by edge passivation with hydrogen atoms. Hydrogen passivation stabilizes the nanoribbons against edge reconstruction and can modify the band gap of armchair nanoribbons. This work provides the foundation for future device applications based on these materials.

9.4. Electronic properties of bare and functionalized Two-Dimensional Tellurene structures

Other two-dimensional materials such as Tellurene may also be suitable for device purposes. In this chapter, the functionalization of Tellurene was studied. Fluorine was found to disrupt both α - and β -Te structures, but hydrogen and oxygen functionalization

resulted in stable structures with semiconducting and metallic properties, respectively. Therefore, the choice of functional adatom can play a key role in tailoring two-dimensional Te for specific applications in semiconducting electronics (H-functionalization) or nanoscale metallic contacts (O-functionalization).

Appendices

Appendix A. Properties of Bare and Hydrogenated Janus Nanoribbons

Table A-1. Properties of bare Janus TMD nanoribbons. Reported are the cohesive energy (E_{coh}), band gap (E_g), band gap character, magnetic moment (μ), magnetic character, curvature radius (r_{curve}), and curvature energy (E_{curve}).

	E_{coh} (eV)	E_g (eV)	Gap Character	μ (μ_B)	Magnetic Character	r_{curve} (\AA)	E_{curve} (eV)
Z4 MoSSe	-4.53	—	—	1.67	AFM	50.12	-0.03
Z5 MoSSe	-4.60	—	—	1.75	AFM	49.45	-0.05
Z6 MoSSe	-4.65	—	—	1.79	AFM	48.27	-0.07
Z7 MoSSe	-4.68	—	—	1.82	AFM	49.03	-0.09
Z8 MoSSe	-4.70	—	—	1.83	AFM	53.51	-0.12
Z4 MoSTe	-4.27	—	—	1.75	FM	19.60	-0.17
Z5 MoSTe	-4.33	—	—	1.77	FM	20.23	-0.31
Z6 MoSTe	-4.37	—	—	1.75	FM	20.64	-0.44
Z7 MoSTe	-4.40	—	—	1.79	AFM	20.90	-0.58
Z8 MoSTe	-4.42	—	—	1.81	AFM	22.24	-0.70
Z4 MoSeTe	-4.02	—	—	2.00	AFM	34.15	-0.06
Z5 MoSeTe	-4.08	—	—	2.02	AFM	35.43	-0.11
Z6 MoSeTe	-4.12	—	—	2.06	AFM	36.40	-0.16
Z7 MoSeTe	-4.15	—	—	2.09	AFM	41.52	-0.20
Z8 MoSeTe	-4.17	—	—	2.11	AFM	44.21	-0.24
Z4 WSSe	-5.36	—	—	1.46	AFM	45.65	-0.04
Z5 WSSe	-5.43	—	—	1.59	AFM	45.61	-0.06
Z6 WSSe	-5.48	—	—	1.63	AFM	46.91	-0.09
Z7 WSSe	-5.52	—	—	1.70	AFM	48.46	-0.11
Z8 WSSe	-5.54	—	—	1.74	AFM	56.17	-0.13
Z4 WSTe	-5.02	—	—	0.24	AFM	26.09	-0.59
Z5 WSTe	-5.08	—	—	0.39	AFM	21.37	-0.94
Z6 WSTe	-5.12	—	—	0.47	AFM	21.11	-0.83
Z7 WSTe	-5.15	—	—	0.53	AFM	20.84	-1.20
Z8 WSTe	-5.18	—	—	0.59	AFM	23.31	-1.32
Z4 WSeTe	-4.83	—	—	0.50	AFM	34.31	-0.95
Z5 WSeTe	-4.86	—	—	0.67	AFM	36.47	-0.96
Z6 WSeTe	-4.88	—	—	0.75	AFM	33.50	-0.99

Z7 WSeTe	-4.90	—	—	0.75	AFM	40.27	-1.04
Z8 WSeTe	-5.06	—	—	0.75	AFM	44.57	-1.07
A6 MoSSe	-4.45	0.42	I	—	NM	51.11	-0.04
A8 MoSSe	-4.56	0.49	I	—	NM	46.26	-0.08
A10 MoSSe	-4.62	0.46	I	—	NM	52.41	-0.13
A12 MoSSe	-4.67	0.49	I	—	NM	57.36	-0.17
A14 MoSSe	-4.70	0.51	I	—	NM	67.48	-0.20
A6 MoSTe	-4.45	0.09	I	—	NM	12.89	-0.32
A8 MoSTe	-4.26	0.27	I	—	NM	16.44	-0.54
A10 MoSTe	-4.31	0.23	I	—	NM	17.91	-0.79
A12 MoSTe	-4.35	0.24	I	—	NM	19.31	-1.06
A14 MoSTe	-4.38	0.24	I	—	NM	20.49	-1.32
A6 MoSeTe	-4.00	0.60	I	—	NM	32.40	-0.06
A8 MoSeTe	-4.06	0.62	D	—	NM	35.90	-1.29
A10 MoSeTe	-4.10	0.65	D	—	NM	34.94	-0.24
A12 MoSeTe	-4.12	0.60	D	—	NM	32.13	-0.97
A14 MoSeTe	-4.13	0.67	D	—	NM	36.95	-0.42
A6 WSSe	-5.29	0.36	I	—	NM	45.43	-0.04
A8 WSSe	-5.40	0.47	D	—	NM	48.01	-0.09
A10 WSSe	-5.46	0.42	D	—	NM	50.28	-0.14
A12 WSSe	-5.51	0.47	D	—	NM	50.49	-0.19
A14 WSSe	-5.54	0.50	D	—	NM	50.78	-0.24
A6 WSTe	-4.96	0.33	I	—	NM	15.98	-0.22
A8 WSTe	-5.11	0.64	D	—	NM	19.28	-0.74
A10 WSTe	-5.15	0.65	D	—	NM	19.67	-0.99
A12 WSTe	-5.18	0.62	D	—	NM	20.31	-1.28
A14 WSTe	-5.21	0.67	D	—	NM	20.36	-1.57
A6 WSeTe	-4.66	0.14	I	—	NM	29.32	-0.05
A8 WSeTe	-4.79	0.17	I	—	NM	35.96	-0.15
A10 WSeTe	-4.85	0.67	D	—	NM	32.44	-0.92
A12 WSeTe	-4.88	0.65	D	—	NM	49.18	-1.01
A14 WSeTe	-4.90	0.70	D	—	NM	40.15	-1.10

Table A-2. Properties of hydrogen-passivated Janus TMD nanoribbons. Reported are the cohesive energy (E_{coh}), band gap (E_g), band gap character, magnetic moment (μ), magnetic character, curvature radius (r_{curve}), and curvature energy (E_{curve}).

	E_{coh} (eV)	E_g (eV)	Gap Character	μ (μ_B)	Magnetic Character	r_{curve} (Å)	E_{curve} (eV)
Z4 MoSSe	-4.02	—	—	1.125	FM	44.39	-0.04
Z5 MoSSe	-4.16	—	—	1.125	FM	54.54	-0.06
Z6 MoSSe	-4.26	—	—	1.125	FM	55.62	-0.08
Z7 MoSSe	-4.33	—	—	1.125	FM	56.26	-0.10
Z8 MoSSe	-4.39	—	—	1.125	FM	73.52	-0.11
Z4 MoSTe	-3.81	—	—	1.125	FM	19.67	-0.21
Z5 MoSTe	-3.93	—	—	1.125	FM	19.34	-0.34
Z6 MoSTe	-4.02	—	—	1.125	FM	21.50	-0.47
Z7 MoSTe	-4.08	—	—	1.40	FM	23.96	-0.39
Z8 MoSTe	-4.13	—	—	1.38	FM	22.94	-0.56
Z4 MoSeTe	-3.63	—	—	0.875	FM	37.79	-0.07
Z5 MoSeTe	-3.74	—	—	0.875	FM	36.80	-0.11
Z6 MoSeTe	-3.81	—	—	0.68	FM	37.82	-0.16
Z7 MoSeTe	-3.88	—	—	0.76	FM	40.28	-0.20
Z8 MoSeTe	-3.92	—	—	0.37	FM	45.30	-0.24
Z4 WSSe	-4.66	—	—	1.25	FM	46.92	-0.04
Z5 WSSe	-4.83	—	—	1.25	FM	49.93	-0.06
Z6 WSSe	-4.95	—	—	1.25	FM	58.17	-0.09
Z7 WSSe	-5.04	—	—	1.25	FM	52.51	-0.11
Z8 WSSe	-5.11	—	—	1.25	FM	70.39	-0.13
Z4 WSTe	-4.39	—	—	0.50	FM	20.18	-0.22
Z5 WSTe	-4.54	—	—	0.50	FM	19.67	-0.37
Z6 WSTe	-4.65	—	—	0.50	FM	20.96	-0.52
Z7 WSTe	-4.73	—	—	0.25	AFM	21.13	-0.67
Z8 WSTe	-4.80	—	—	0.25	AFM	20.81	-0.82
Z4 WSeTe	-4.44	—	—	—	NM	36.19	-0.07
Z5 WSeTe	-4.68	—	—	—	NM	37.57	-0.12
Z6 WSeTe	-4.85	—	—	—	NM	40.40	-0.17
Z7 WSeTe	-4.97	—	—	—	NM	38.38	-0.22
Z8 WSeTe	-5.06	—	—	—	NM	45.36	-0.26
A6 MoSSe	-3.85	0.61	D	—	NM	47.73	-0.05
A8 MoSSe	-4.04	0.60	D	—	NM	52.12	-0.09
A10 MoSSe	-4.18	0.65	D	—	NM	51.06	-0.13
A12 MoSSe	-4.27	0.67	D	—	NM	56.45	-0.17

A14 MoSSe	-4.34	0.66	D	—	NM	65.86	-0.20
A6 MoSTe	-3.63	0.56	D	—	NM	22.13	-0.23
A8 MoSTe	-3.80	0.60	D	—	NM	21.80	-0.48
A10 MoSTe	-3.92	0.59	D	—	NM	20.26	-0.75
A12 MoSTe	-4.00	0.58	D	—	NM	21.64	-1.01
A14 MoSTe	-4.06	0.56	D	—	NM	22.39	-1.27
A6 MoSeTe	-3.43	0.07	I	—	NM	32.64	-0.07
A8 MoSeTe	-3.58	0.08	I	—	NM	38.88	-0.15
A10 MoSeTe	-3.68	0.07	I	—	NM	36.97	-0.34
A12 MoSeTe	-3.76	0.38	D	—	NM	38.87	-0.34
A14 MoSeTe	-3.82	0.39	D	—	NM	36.81	-0.43
A6 WSSe	-4.44	0.36	D	—	NM	45.02	-0.06
A8 WSSe	-4.68	0.47	D	—	NM	48.50	-0.10
A10 WSSe	-4.85	0.42	D	—	NM	50.29	-0.15
A12 WSSe	-4.97	0.47	D	—	NM	56.19	-0.20
A14 WSSe	-5.06	0.50	D	—	NM	60.33	-0.24
A6 WSTe	-4.18	0.33	D	—	NM	20.21	-0.29
A8 WSTe	-4.40	0.64	D	—	NM	20.63	-0.57
A10 WSTe	-4.55	0.65	D	—	NM	20.54	-0.87
A12 WSTe	-4.66	0.62	D	—	NM	21.45	-1.16
A14 WSTe	-4.74	0.67	D	—	NM	20.57	-1.46
A6 WSeTe	-3.96	0.14	I	—	NM	30.91	-0.10
A8 WSeTe	-4.16	0.17	D	—	NM	37.06	-0.18
A10 WSeTe	-4.30	0.67	D	—	NM	38.09	-0.27
A12 WSeTe	-4.39	0.65	D	—	NM	41.41	-0.36
A14 WSeTe	-4.47	0.70	D	—	NM	40.34	-0.47

References

- (1) Das, S.; Robinson, J. A.; Dubey, M.; Terrones, H.; Terrones, M. Beyond Graphene: Progress in Novel Two-Dimensional Materials and van Der Waals Solids. *Annu. Rev. Mater. Res.* **2015**, *45* (1), 1–27. <https://doi.org/10.1146/annurev-matsci-070214-021034>.
- (2) Mueller, T.; Malic, E. Exciton Physics and Device Application of Two-Dimensional Transition Metal Dichalcogenide Semiconductors. *Npj 2D Mater. Appl.* **2018**, *2* (1), 1–12. <https://doi.org/10.1038/s41699-018-0074-2>.
- (3) Ren, Y.; Qiao, Z.; Niu, Q. Topological Phases in Two-Dimensional Materials: A Review. *Rep. Prog. Phys.* **2016**, *79* (6), 066501. <https://doi.org/10.1088/0034-4885/79/6/066501>.
- (4) Brun, C.; Cren, T.; Roditchev, D. Review of 2D Superconductivity: The Ultimate Case of Epitaxial Monolayers. *Supercond. Sci. Technol.* **2016**, *30* (1), 013003. <https://doi.org/10.1088/0953-2048/30/1/013003>.
- (5) Li, X.; Zhu, H. Two-Dimensional MoS₂: Properties, Preparation, and Applications. *J. Materiomics* **2015**, *1* (1), 33–44. <https://doi.org/10.1016/j.jmat.2015.03.003>.
- (6) Radisavljevic, B.; Radenovic, A.; Brivio, J.; Giacometti, V.; Kis, A. Single-Layer MoS₂ Transistors. *Nat. Nanotechnol.* **2011**, *6* (3), 147–150. <https://doi.org/10.1038/nnano.2010.279>.
- (7) Zhu, W.; Low, T.; Lee, Y.-H.; Wang, H.; Farmer, D. B.; Kong, J.; Xia, F.; Avouris, P. Electronic Transport and Device Prospects of Monolayer Molybdenum Disulphide Grown by Chemical Vapour Deposition. *Nat. Commun.* **2014**, *5*, ncomms4087. <https://doi.org/10.1038/ncomms4087>.
- (8) Desai, S. B.; Madhvapathy, S. R.; Sachid, A. B.; Llinas, J. P.; Wang, Q.; Ahn, G. H.; Pitner, G.; Kim, M. J.; Bokor, J.; Hu, C.; Wong, H.-S. P.; Javey, A. MoS₂ Transistors with 1-Nanometer Gate Lengths. *Science* **2016**, *354* (6308), 99–102. <https://doi.org/10.1126/science.aah4698>.
- (9) Mak, K. F.; Lee, C.; Hone, J.; Shan, J.; Heinz, T. F. Atomically Thin MoS₂: A New Direct-Gap Semiconductor. *Phys. Rev. Lett.* **2010**, *105* (13), 136805. <https://doi.org/10.1103/PhysRevLett.105.136805>.
- (10) Lee, Y.-H.; Zhang, X.-Q.; Zhang, W.; Chang, M.-T.; Lin, C.-T.; Chang, K.-D.; Yu, Y.-C.; Wang, J. T.-W.; Chang, C.-S.; Li, L.-J.; Lin, T.-W. Synthesis of Large-Area MoS₂ Atomic Layers with Chemical Vapor Deposition. *Adv. Mater.* **2012**, *24* (17), 2320–2325. <https://doi.org/10.1002/adma.201104798>.
- (11) Liu, K.-K.; Zhang, W.; Lee, Y.-H.; Lin, Y.-C.; Chang, M.-T.; Su, C.-Y.; Chang, C.-S.; Li, H.; Shi, Y.; Zhang, H.; Lai, C.-S.; Li, L.-J. Growth of Large-Area and Highly Crystalline MoS₂ Thin Layers on Insulating Substrates. *Nano Lett.* **2012**, *12* (3), 1538–1544. <https://doi.org/10.1021/nl2043612>.
- (12) Najmaei, S.; Liu, Z.; Zhou, W.; Zou, X.; Shi, G.; Lei, S.; Yakobson, B. I.; Idrobo, J.-C.; Ajayan, P. M.; Lou, J. Vapour Phase Growth and Grain Boundary Structure of Molybdenum Disulphide Atomic Layers. *Nat. Mater.* **2013**, *12* (8), 754–759. <https://doi.org/10.1038/nmat3673>.

- (13) Zhan, Y.; Liu, Z.; Najmaei, S.; Ajayan, P. M.; Lou, J. Large-Area Vapor-Phase Growth and Characterization of MoS₂ Atomic Layers on a SiO₂ Substrate. *Small* **2012**, *8* (7), 966–971. <https://doi.org/10.1002/sml.201102654>.
- (14) Dumcenco, D.; Ovchinnikov, D.; Marinov, K.; Lazić, P.; Gibertini, M.; Marzari, N.; Sanchez, O. L.; Kung, Y.-C.; Krasnozhan, D.; Chen, M.-W.; Bertolazzi, S.; Gillet, P.; Fontcuberta i Morral, A.; Radenovic, A.; Kis, A. Large-Area Epitaxial Monolayer MoS₂. *ACS Nano* **2015**, *9* (4), 4611–4620. <https://doi.org/10.1021/acsnano.5b01281>.
- (15) Liou, J. J.; Ortiz-Conde, A.; Garcia-Sanchez, F. *Analysis and Design of MOSFETs: Modeling, Simulation, and Parameter Extraction*; Springer Science & Business Media, 2012.
- (16) Bohr, M. T.; Chau, R. S.; Ghani, T.; Mistry, K. The High-k Solution. *IEEE Spectr.* **2007**, *44* (10), 29–35. <https://doi.org/10.1109/MSPEC.2007.4337663>.
- (17) Schwierz, F.; Pezoldt, J.; Granzner, R. Two-Dimensional Materials and Their Prospects in Transistor Electronics. *Nanoscale* **2015**, *7* (18), 8261–8283. <https://doi.org/10.1039/C5NR01052G>.
- (18) Robertson, J.; Wallace, R. M. High-K Materials and Metal Gates for CMOS Applications. *Mater. Sci. Eng. R Rep.* **2015**, *88*, 1–41. <https://doi.org/10.1016/j.mser.2014.11.001>.
- (19) Auth, C.; Cappellani, A.; Chun, J. S.; Dalis, A.; Davis, A.; Ghani, T.; Glass, G.; Glassman, T.; Harper, M.; Hattendorf, M.; Hentges, P.; Jaloviar, S.; Joshi, S.; Klaus, J.; Kuhn, K.; Lavric, D.; Lu, M.; Mariappan, H.; Mistry, K.; Norris, B.; Rahhal-orabi, N.; Ranade, P.; Sandford, J.; Shifren, L.; Souw, V.; Tone, K.; Tambwe, F.; Thompson, A.; Towner, D.; Troeger, T.; Vandervoorn, P.; Wallace, C.; Wiedemer, J.; Wiegand, C. 45nm High-k + Metal Gate Strain-Enhanced Transistors. In *2008 Symposium on VLSI Technology*; 2008; pp 128–129. <https://doi.org/10.1109/VLSIT.2008.4588589>.
- (20) Ye, P. D.; Wilk, G. D.; Kwo, J.; Yang, B.; Gossmann, H. J. L.; Frei, M.; Chu, S. N. G.; Mannaerts, J. P.; Sergent, M.; Hong, M.; Ng, K. K.; Bude, J. GaAs MOSFET with Oxide Gate Dielectric Grown by Atomic Layer Deposition. *IEEE Electron Device Lett.* **2003**, *24* (4), 209–211. <https://doi.org/10.1109/LED.2003.812144>.
- (21) Takagi, S.; Iisawa, T.; Tezuka, T.; Numata, T.; Nakaharai, S.; Hirashita, N.; Moriyama, Y.; Usuda, K.; Toyoda, E.; Dissanayake, S.; Shichijo, M.; Nakane, R.; Sugahara, S.; Takenaka, M.; Sugiyama, N. Carrier-Transport-Enhanced Channel CMOS for Improved Power Consumption and Performance. *IEEE Trans. Electron Devices* **2008**, *55* (1), 21–39. <https://doi.org/10.1109/TED.2007.911034>.
- (22) Sylvia, S. S.; Park, H.-H.; Khayer, M. A.; Alam, K.; Klimeck, G.; Lake, R. K. Material Selection for Minimizing Direct Tunneling in Nanowire Transistors. *IEEE Trans. Electron Devices* **2012**, *59* (8), 2064–2069. <https://doi.org/10.1109/TED.2012.2200688>.
- (23) Novoselov, K. S.; Geim, A. K.; Morozov, S. V.; Jiang, D.; Zhang, Y.; Dubonos, S. V.; Grigorieva, I. V.; Firsov, A. A. Electric Field Effect in

- Atomically Thin Carbon Films. *Science* **2004**, *306* (5696), 666–669.
<https://doi.org/10.1126/science.1102896>.
- (24) Novoselov, K. S.; Jiang, D.; Schedin, F.; Booth, T. J.; Khotkevich, V. V.; Morozov, S. V.; Geim, A. K. Two-Dimensional Atomic Crystals. *Proc. Natl. Acad. Sci. U. S. A.* **2005**, *102* (30), 10451–10453.
<https://doi.org/10.1073/pnas.0502848102>.
- (25) Rai, A.; Valsaraj, A.; Movva, H. C. P.; Roy, A.; Ghosh, R.; Sonde, S.; Kang, S.; Chang, J.; Trivedi, T.; Dey, R.; Guchhait, S.; Larentis, S.; Register, L. F.; Tutuc, E.; Banerjee, S. K. Air Stable Doping and Intrinsic Mobility Enhancement in Monolayer Molybdenum Disulfide by Amorphous Titanium Suboxide Encapsulation. *Nano Lett.* **2015**, *15* (7), 4329–4336.
<https://doi.org/10.1021/acs.nanolett.5b00314>.
- (26) Kaasbjerg, K.; Thygesen, K. S.; Jacobsen, K. W. Phonon-Limited Mobility in n-Type Single-Layer MoS₂ from First Principles. *Phys. Rev. B* **2012**, *85* (11), 115317. <https://doi.org/10.1103/PhysRevB.85.115317>.
- (27) Gomez, L.; Aberg, I.; Hoyt, J. L. Electron Transport in Strained-Silicon Directly on Insulator Ultrathin-Body n-MOSFETs With Body Thickness Ranging From 2 to 25 Nm. *IEEE Electron Device Lett.* **2007**, *28* (4), 285–287. <https://doi.org/10.1109/LED.2007.891795>.
- (28) Liu, H.; Neal, A. T.; Ye, P. D. Channel Length Scaling of MoS₂ MOSFETs. *ACS Nano* **2012**, *6* (10), 8563–8569. <https://doi.org/10.1021/nn303513c>.
- (29) Jena, D.; Konar, A. Enhancement of Carrier Mobility in Semiconductor Nanostructures by Dielectric Engineering. *Phys. Rev. Lett.* **2007**, *98* (13), 136805. <https://doi.org/10.1103/PhysRevLett.98.136805>.
- (30) Kim, S. Y.; Park, S.; Choi, W. Enhanced Carrier Mobility of Multilayer MoS₂ Thin-Film Transistors by Al₂O₃ Encapsulation. *Appl. Phys. Lett.* **2016**, *109* (15), 152101. <https://doi.org/10.1063/1.4964606>.
- (31) Liu, H.; Ye, P. D. Dual-Gate MOSFET With Atomic-Layer-Deposited as Top-Gate Dielectric. *IEEE Electron Device Lett.* **2012**, *33* (4), 546–548. <https://doi.org/10.1109/LED.2012.2184520>.
- (32) Qian, Q.; Zhang, Z.; Hua, M.; Tang, G.; Lei, J.; Lan, F.; Xu, Y.; Ruyue Yan; Chen, K. J. Enhanced Dielectric Deposition on Single-Layer MoS₂ with Low Damage Using Remote N₂ Plasma Treatment. *Nanotechnology* **2017**, *28* (17), 175202. <https://doi.org/10.1088/1361-6528/aa6756>.
- (33) Yang, W.; Sun, Q.-Q.; Geng, Y.; Chen, L.; Zhou, P.; Ding, S.-J.; Zhang, D. W. The Integration of Sub-10 Nm Gate Oxide on MoS₂ with Ultra Low Leakage and Enhanced Mobility. *Sci. Rep.* **2015**, *5*, 11921. <https://doi.org/10.1038/srep11921>.
- (34) Puurunen, R. L. A Short History of Atomic Layer Deposition: Tuomo Suntola's Atomic Layer Epitaxy. *Chem. Vap. Depos.* **2014**, *20* (10-11-12), 332–344. <https://doi.org/10.1002/cvde.201402012>.
- (35) Puurunen, R. L. Surface Chemistry of Atomic Layer Deposition: A Case Study for the Trimethylaluminum/Water Process. *J. Appl. Phys.* **2005**, *97* (12), 121301. <https://doi.org/10.1063/1.1940727>.
- (36) George, S. M. Atomic Layer Deposition: An Overview. *Chem. Rev.* **2010**, *110* (1), 111–131. <https://doi.org/10.1021/cr900056b>.

- (37) Kobayashi, N. P.; Donley, C. L.; Wang, S.-Y.; Williams, R. S. Atomic Layer Deposition of Aluminum Oxide on Hydrophobic and Hydrophilic Surfaces. *J. Cryst. Growth* **2007**, *299* (1), 218–222. <https://doi.org/10.1016/j.jcrysgro.2006.11.224>.
- (38) Azcatl, A.; McDonnell, S.; C, S. K.; Peng, X.; Dong, H.; Qin, X.; Addou, R.; Mordi, G. I.; Lu, N.; Kim, J.; Kim, M. J.; Cho, K.; Wallace, R. M. MoS₂ Functionalization for Ultra-Thin Atomic Layer Deposited Dielectrics. *Appl. Phys. Lett.* **2014**, *104* (11), 111601. <https://doi.org/10.1063/1.4869149>.
- (39) McDonnell, S.; Brennan, B.; Azcatl, A.; Lu, N.; Dong, H.; Buie, C.; Kim, J.; Hinkle, C. L.; Kim, M. J.; Wallace, R. M. HfO₂ on MoS₂ by Atomic Layer Deposition: Adsorption Mechanisms and Thickness Scalability. *ACS Nano* **2013**, *7* (11), 10354–10361. <https://doi.org/10.1021/nn404775u>.
- (40) Qian, Q.; Li, B.; Hua, M.; Zhang, Z.; Lan, F.; Xu, Y.; Yan, R.; Chen, K. J. Improved Gate Dielectric Deposition and Enhanced Electrical Stability for Single-Layer MoS₂ MOSFET with an AlN Interfacial Layer. *Sci. Rep.* **2016**, *6*, 27676. <https://doi.org/10.1038/srep27676>.
- (41) Liu, H.; Xu, K.; Zhang, X.; Ye, P. D. The Integration of High-k Dielectric on Two-Dimensional Crystals by Atomic Layer Deposition. *Appl. Phys. Lett.* **2012**, *100* (15), 152115. <https://doi.org/10.1063/1.3703595>.
- (42) Yang, J.; Kim, S.; Choi, W.; Park, S. H.; Jung, Y.; Cho, M.-H.; Kim, H. Improved Growth Behavior of Atomic-Layer-Deposited High-k Dielectrics on Multilayer MoS₂ by Oxygen Plasma Pretreatment. *ACS Appl. Mater. Interfaces* **2013**, *5* (11), 4739–4744. <https://doi.org/10.1021/am303261c>.
- (43) Cheng, L.; Qin, X.; Lucero, A. T.; Azcatl, A.; Huang, J.; Wallace, R. M.; Cho, K.; Kim, J. Atomic Layer Deposition of a High-k Dielectric on MoS₂ Using Trimethylaluminum and Ozone. *ACS Appl. Mater. Interfaces* **2014**, *6* (15), 11834–11838. <https://doi.org/10.1021/am5032105>.
- (44) Son, S.; Yu, S.; Choi, M.; Kim, D.; Choi, C. Improved High Temperature Integration of Al₂O₃ on MoS₂ by Using a Metal Oxide Buffer Layer. *Appl. Phys. Lett.* **2015**, *106* (2), 021601. <https://doi.org/10.1063/1.4905634>.
- (45) Henegar, Dr. A. J.; Gougousi, Prof. T. Comparison of the Reactivity of Alkyl and Alkyl Amine Precursors with Native Oxide GaAs(100) and InAs(100) Surfaces. *Appl. Surf. Sci.* **2016**, *390*, 870–881. <https://doi.org/10.1016/j.apsusc.2016.08.144>.
- (46) Hausmann, D. M.; Gordon, R. G. Surface Morphology and Crystallinity Control in the Atomic Layer Deposition (ALD) of Hafnium and Zirconium Oxide Thin Films. *J. Cryst. Growth* **2003**, *249* (1–2), 251–261. [https://doi.org/10.1016/S0022-0248\(02\)02133-4](https://doi.org/10.1016/S0022-0248(02)02133-4).
- (47) Henegar, A. J. Surface Chemistry and Interface Evolution during the Atomic Layer Deposition of High-k Metal Oxides on InAs(100) and GaAs(100) Surfaces. Ph.D., University of Maryland, Baltimore County, United States -- Maryland, 2015.
- (48) Magda, G. Z.; Pető, J.; Dobrik, G.; Hwang, C.; Biró, L. P.; Tapasztó, L. Exfoliation of Large-Area Transition Metal Chalcogenide Single Layers. *Sci. Rep.* **2015**, *5*, 14714. <https://doi.org/10.1038/srep14714>.

- (49) Ayari, A.; Cobas, E.; Ogundadegbe, O.; Fuhrer, M. S. Realization and Electrical Characterization of Ultrathin Crystals of Layered Transition-Metal Dichalcogenides. *J. Appl. Phys.* **2007**, *101* (1), 014507. <https://doi.org/10.1063/1.2407388>.
- (50) Huang, Y.; Sutter, E.; Shi, N. N.; Zheng, J.; Yang, T.; Englund, D.; Gao, H.-J.; Sutter, P. Reliable Exfoliation of Large-Area High-Quality Flakes of Graphene and Other Two-Dimensional Materials. *ACS Nano* **2015**, *9* (11), 10612–10620. <https://doi.org/10.1021/acsnano.5b04258>.
- (51) Late, D. J.; Liu, B.; Matte, H. S. S. R.; Rao, C. N. R.; Dravid, V. P. Rapid Characterization of Ultrathin Layers of Chalcogenides on SiO₂/Si Substrates. *Adv. Funct. Mater.* **2012**, *22* (9), 1894–1905. <https://doi.org/10.1002/adfm.201102913>.
- (52) Li, H.; Wu, J.; Huang, X.; Lu, G.; Yang, J.; Lu, X.; Xiong, Q.; Zhang, H. Rapid and Reliable Thickness Identification of Two-Dimensional Nanosheets Using Optical Microscopy. *ACS Nano* **2013**, *7* (11), 10344–10353. <https://doi.org/10.1021/nn4047474>.
- (53) Binnig, G.; Quate, C. F.; Gerber, Ch. Atomic Force Microscope. *Phys. Rev. Lett.* **1986**, *56* (9), 930–933. <https://doi.org/10.1103/PhysRevLett.56.930>.
- (54) Vickerman, J. C. *Surface Analysis: The Principal Techniques*; John Wiley, 1997.
- (55) Haugstad, G. *Atomic Force Microscopy: Understanding Basic Modes and Advanced Applications*; John Wiley & Sons, 2012.
- (56) Barr, T. L.; Seal, S. Nature of the Use of Adventitious Carbon as a Binding Energy Standard. *J. Vac. Sci. Technol. A* **1995**, *13* (3), 1239–1246. <https://doi.org/10.1116/1.579868>.
- (57) Heide, P. van der. *X-Ray Photoelectron Spectroscopy: An Introduction to Principles and Practices*; John Wiley & Sons, 2011.
- (58) Wiegenstein, C. G.; Schulz, K. H. Methanethiol Adsorption on Defective MoS₂(0001) Surfaces. *J. Phys. Chem. B* **1999**, *103* (33), 6913–6918. <https://doi.org/10.1021/jp990896y>.
- (59) Bertolazzi, S.; Bonacchi, S.; Nan, G.; Pershin, A.; Beljonne, D.; Samorì, P. Engineering Chemically Active Defects in Monolayer MoS₂ Transistors via Ion-Beam Irradiation and Their Healing via Vapor Deposition of Alkanethiols. *Adv. Mater.* **2017**, *29* (18), 1606760. <https://doi.org/10.1002/adma.201606760>.
- (60) Ma, Q.; Odenthal, P. M.; Mann, J.; Le, D.; Wang, C. S.; Zhu, Y.; Chen, T.; Sun, D.; Yamaguchi, K.; Tran, T.; Wurch, M.; McKinley, J. L.; Wyrick, J.; Magnone, K.; Heinz, T. F.; Rahman, T. S.; Kawakami, R.; Bartels, L. Controlled Argon Beam-Induced Desulfurization of Monolayer Molybdenum Disulfide. *J. Phys. Condens. Matter* **2013**, *25* (25), 252201. <https://doi.org/10.1088/0953-8984/25/25/252201>.
- (61) Sholl, D.; Steckel, J. A. *Density Functional Theory: A Practical Introduction*; Wiley, 2009.
- (62) Hohenberg, P.; Kohn, W. Inhomogeneous Electron Gas. *Phys. Rev.* **1964**, *136* (3B), B864–B871. <https://doi.org/10.1103/PhysRev.136.B864>.

- (63) Kohn, W.; Sham, L. J. Self-Consistent Equations Including Exchange and Correlation Effects. *Phys. Rev.* **1965**, *140* (4A), A1133–A1138. <https://doi.org/10.1103/PhysRev.140.A1133>.
- (64) Perdew, J. P.; Wang, Y. Accurate and Simple Analytic Representation of the Electron-Gas Correlation Energy. *Phys. Rev. B* **1992**, *45* (23), 13244–13249. <https://doi.org/10.1103/PhysRevB.45.13244>.
- (65) Perdew, J. P.; Chevary, J. A.; Vosko, S. H.; Jackson, K. A.; Pederson, M. R.; Singh, D. J.; Fiolhais, C. Atoms, Molecules, Solids, and Surfaces: Applications of the Generalized Gradient Approximation for Exchange and Correlation. *Phys. Rev. B* **1992**, *46* (11), 6671–6687. <https://doi.org/10.1103/PhysRevB.46.6671>.
- (66) Perdew, J. P.; Burke, K.; Ernzerhof, M. Generalized Gradient Approximation Made Simple. *Phys. Rev. Lett.* **1996**, *77* (18), 3865–3868. <https://doi.org/10.1103/PhysRevLett.77.3865>.
- (67) Ashcroft, N. W.; Mermin, N. D. *Solid State Physics*; Holt, Rinehart and Winston, 1976.
- (68) Monkhorst, H. J.; Pack, J. D. Special Points for Brillouin-Zone Integrations. *Phys. Rev. B* **1976**, *13* (12), 5188–5192. <https://doi.org/10.1103/PhysRevB.13.5188>.
- (69) Hamann, D. R.; Schlüter, M.; Chiang, C. Norm-Conserving Pseudopotentials. *Phys. Rev. Lett.* **1979**, *43* (20), 1494–1497. <https://doi.org/10.1103/PhysRevLett.43.1494>.
- (70) Vanderbilt, D. Soft Self-Consistent Pseudopotentials in a Generalized Eigenvalue Formalism. *Phys. Rev. B* **1990**, *41* (11), 7892–7895. <https://doi.org/10.1103/PhysRevB.41.7892>.
- (71) Kresse, G.; Joubert, D. From Ultrasoft Pseudopotentials to the Projector Augmented-Wave Method. *Phys. Rev. B* **1999**, *59* (3), 1758–1775. <https://doi.org/10.1103/PhysRevB.59.1758>.
- (72) Blöchl, P. E. Projector Augmented-Wave Method. *Phys. Rev. B* **1994**, *50* (24), 17953–17979. <https://doi.org/10.1103/PhysRevB.50.17953>.
- (73) Kresse, G.; Furthmüller, J. Efficient Iterative Schemes for Ab Initio Total-Energy Calculations Using a Plane-Wave Basis Set. *Phys. Rev. B* **1996**, *54* (16), 11169–11186. <https://doi.org/10.1103/PhysRevB.54.11169>.
- (74) Song, J.-G.; Kim, S. J.; Woo, W. J.; Kim, Y.; Oh, I.-K.; Ryu, G. H.; Lee, Z.; Lim, J. H.; Park, J.; Kim, H. Effect of Al₂O₃ Deposition on Performance of Top-Gated Monolayer MoS₂-Based Field Effect Transistor. *ACS Appl. Mater. Interfaces* **2016**, *8* (41), 28130–28135. <https://doi.org/10.1021/acsami.6b07271>.
- (75) Wang, Q. H.; Kalantar-Zadeh, K.; Kis, A.; Coleman, J. N.; Strano, M. S. Electronics and Optoelectronics of Two-Dimensional Transition Metal Dichalcogenides. *Nat. Nanotechnol.* **2012**, *7* (11), 699–712. <https://doi.org/10.1038/nnano.2012.193>.
- (76) Price, K. M.; Schauble, K. E.; McGuire, F. A.; Farmer, D. B.; Franklin, A. D. Uniform Growth of Sub-5-Nanometer High- κ Dielectrics on MoS₂ Using Plasma-Enhanced Atomic Layer Deposition. *ACS Appl. Mater. Interfaces* **2017**, *9* (27), 23072–23080. <https://doi.org/10.1021/acsami.7b00538>.

- (77) Park, W.; Min, J.-W.; Shaikh, S. F.; Hussain, M. M. Stable MoS₂ Field-Effect Transistors Using TiO₂ Interfacial Layer at Metal/MoS₂ Contact. *Phys. Status Solidi A* **2017**, *214* (12), 1700534. <https://doi.org/10.1002/pssa.201700534>.
- (78) Pak, Y.; Park, W.; Mitra, S.; Devi, A. A. S.; Loganathan, K.; Kumaresan, Y.; Kim, Y.; Cho, B.; Jung, G.-Y.; Hussain, M. M.; Roqan, I. S. Enhanced Performance of MoS₂ Photodetectors by Inserting an ALD-Processed TiO₂ Interlayer. *Small* **2018**, *14* (5), 1703176. <https://doi.org/10.1002/sml.201703176>.
- (79) Bolshakov, P.; Zhao, P.; Azcatl, A.; Hurley, P. K.; Wallace, R. M.; Young, C. D. Electrical Characterization of Top-Gated Molybdenum Disulfide Field-Effect-Transistors with High-k Dielectrics. *Microelectron. Eng.* **2017**, *178*, 190–193. <https://doi.org/10.1016/j.mee.2017.04.045>.
- (80) Wen, M.; Xu, J.; Liu, L.; Lai, P. T.; Tang, W. M. Improved Electrical Performance of Multilayer MoS₂ Transistor With NH₃-Annealed ALD HfTiO Gate Dielectric. *IEEE Trans. Electron Devices* **2017**, *64* (3), 1020–1025. <https://doi.org/10.1109/TED.2017.2650920>.
- (81) Park, T.; Kim, H.; Leem, M.; Ahn, W.; Choi, S.; Kim, J.; Uh, J.; Kwon, K.; Jeong, S.-J.; Park, S.; Kim, Y.; Kim, H. Atomic Layer Deposition of Al₂O₃ on MoS₂, WS₂, WSe₂, and h-BN: Surface Coverage and Adsorption Energy. *RSC Adv.* **2017**, *7* (2), 884–889. <https://doi.org/10.1039/C6RA24733D>.
- (82) Zhang, H.; Chiappe, D.; Meersschaut, J.; Conard, T.; Franquet, A.; Nuytten, T.; Mannarino, M.; Radu, I.; Vandervorst, W.; Delabie, A. Nucleation and Growth Mechanisms of Al₂O₃ Atomic Layer Deposition on Synthetic Polycrystalline MoS₂. *J. Chem. Phys.* **2016**, *146* (5), 052810. <https://doi.org/10.1063/1.4967406>.
- (83) Addou, R.; Colombo, L.; Wallace, R. M. Surface Defects on Natural MoS₂. *ACS Appl. Mater. Interfaces* **2015**, *7* (22), 11921–11929. <https://doi.org/10.1021/acsami.5b01778>.
- (84) Zhou, W.; Zou, X.; Najmaei, S.; Liu, Z.; Shi, Y.; Kong, J.; Lou, J.; Ajayan, P. M.; Yakobson, B. I.; Idrobo, J.-C. Intrinsic Structural Defects in Monolayer Molybdenum Disulfide. *Nano Lett.* **2013**, *13* (6), 2615–2622. <https://doi.org/10.1021/nl4007479>.
- (85) Zhou, S.; Wang, S.; Li, H.; Xu, W.; Gong, C.; Grossman, J. C.; Warner, J. H. Atomic Structure and Dynamics of Defects in 2D MoS₂ Bilayers. *ACS Omega* **2017**, *2* (7), 3315–3324. <https://doi.org/10.1021/acsomega.7b00734>.
- (86) Hong, J.; Hu, Z.; Probert, M.; Li, K.; Lv, D.; Yang, X.; Gu, L.; Mao, N.; Feng, Q.; Xie, L.; Zhang, J.; Wu, D.; Zhang, Z.; Jin, C.; Ji, W.; Zhang, X.; Yuan, J.; Zhang, Z. Exploring Atomic Defects in Molybdenum Disulfide Monolayers. *Nat. Commun.* **2015**, *6* (1), 1–8. <https://doi.org/10.1038/ncomms7293>.
- (87) Horcas, I.; Fernández, R.; Gómez-Rodríguez, J. M.; Colchero, J.; Gómez-Herrero, J.; Baro, A. M. WSXM: A Software for Scanning Probe Microscopy and a Tool for Nanotechnology. *Rev. Sci. Instrum.* **2007**, *78* (1), 013705. <https://doi.org/10.1063/1.2432410>.
- (88) ImageJ <https://imagej.nih.gov/ij/> (accessed Mar 10, 2017).

- (89) Sauvola, J.; Pietikäinen, M. Adaptive Document Image Binarization. *Pattern Recognit.* **2000**, *33* (2), 225–236. [https://doi.org/10.1016/S0031-3203\(99\)00055-2](https://doi.org/10.1016/S0031-3203(99)00055-2).
- (90) Lee, C.; Yan, H.; Brus, L. E.; Heinz, T. F.; Hone, J.; Ryu, S. Anomalous Lattice Vibrations of Single- and Few-Layer MoS₂. *ACS Nano* **2010**, *4* (5), 2695–2700. <https://doi.org/10.1021/nn1003937>.
- (91) Placidi, M.; Dimitrievska, M.; Izquierdo-Roca, V.; Fontané, X.; Andres Castellanos-Gomez; Pérez-Tomás, A.; Mestres, N.; Espindola-Rodriguez, M.; Simon López-Marino; Neuschitzer, M.; Bermudez, V.; Yaremko, A.; Pérez-Rodríguez, A. Multiwavelength Excitation Raman Scattering Analysis of Bulk and Two-Dimensional MoS₂: Vibrational Properties of Atomically Thin MoS₂ Layers. *2D Mater.* **2015**, *2* (3), 035006. <https://doi.org/10.1088/2053-1583/2/3/035006>.
- (92) Henegar, A. J.; Gougousi, T. Stability and Surface Reactivity of Anatase TiO₂ Films. *ECS J. Solid State Sci. Technol.* **2015**, *4* (8), P298–P304. <https://doi.org/10.1149/2.0041508jss>.
- (93) Kc, S.; Longo, R. C.; Wallace, R. M.; Cho, K. Surface Oxidation Energetics and Kinetics on MoS₂ Monolayer. *J. Appl. Phys.* **2015**, *117* (13), 135301. <https://doi.org/10.1063/1.4916536>.
- (94) Hackley, J. C.; Demaree, J. D.; Gougousi, T. Growth and Interface of HfO₂ Films on H-Terminated Si from a TDMAH and H₂O Atomic Layer Deposition Process. *J. Vac. Sci. Technol. A* **2008**, *26* (5), 1235–1240. <https://doi.org/10.1116/1.2965813>.
- (95) Mak, K. F.; Shan, J. Photonics and Optoelectronics of 2D Semiconductor Transition Metal Dichalcogenides. *Nat. Photonics* **2016**, *10* (4), 216–226. <https://doi.org/10.1038/nphoton.2015.282>.
- (96) Azcatl, A.; KC, S.; Peng, X.; Lu, N.; McDonnell, S.; Qin, X.; Dios, F. de; Addou, R.; Kim, J.; Kim, M. J.; Cho, K.; Wallace, R. M. HfO₂ on UV–O₃ exposed Transition Metal Dichalcogenides: Interfacial Reactions Study. *2D Mater.* **2015**, *2* (1), 014004. <https://doi.org/10.1088/2053-1583/2/1/014004>.
- (97) Wirtz, C.; Hallam, T.; Cullen, C. P.; Berner, N. C.; O’Brien, M.; Marcia, M.; Hirsch, A.; Duesberg, G. S. Atomic Layer Deposition on 2D Transition Metal Chalcogenides: Layer Dependent Reactivity and Seeding with Organic Ad-Layers. *Chem. Commun.* **2015**, *51* (92), 16553–16556. <https://doi.org/10.1039/C5CC05726D>.
- (98) Zhang, H.; Arutchelvan, G.; Meersschaut, J.; Gaur, A.; Conard, T.; Bender, H.; Lin, D.; Asselberghs, I.; Heyns, M.; Radu, I.; Vandervorst, W.; Delabie, A. MoS₂ Functionalization with a Sub-Nm Thin SiO₂ Layer for Atomic Layer Deposition of High-κ Dielectrics. *Chem. Mater.* **2017**, *29* (16), 6772–6780. <https://doi.org/10.1021/acs.chemmater.7b01695>.
- (99) Kropp, J. A.; Cai, Y.; Yao, Z.; Zhu, W.; Gougousi, T. Atomic Layer Deposition of Al₂O₃ and TiO₂ on MoS₂ Surfaces. *J. Vac. Sci. Technol. A* **2018**, *36* (6), 06A101. <https://doi.org/10.1116/1.5043621>.
- (100) Makarova, M.; Okawa, Y.; Aono, M. Selective Adsorption of Thiol Molecules at Sulfur Vacancies on MoS₂(0001), Followed by Vacancy Repair

- via S–C Dissociation. *J. Phys. Chem. C* **2012**, *116* (42), 22411–22416. <https://doi.org/10.1021/jp307267h>.
- (101) Kim, J.-S.; Yoo, H.-W.; Choi, H. O.; Jung, H.-T. Tunable Volatile Organic Compounds Sensor by Using Thiolated Ligand Conjugation on MoS₂. *Nano Lett.* **2014**, *14* (10), 5941–5947. <https://doi.org/10.1021/nl502906a>.
- (102) Nguyen, E. P.; Carey, B. J.; Ou, J. Z.; van Embden, J.; Gaspera, E. D.; Chrimes, A. F.; Spencer, M. J. S.; Zhuiykov, S.; Kalantar-zadeh, K.; Daeneke, T. Electronic Tuning of 2D MoS₂ through Surface Functionalization. *Adv. Mater.* **2015**, *27* (40), 6225–6229. <https://doi.org/10.1002/adma.201503163>.
- (103) Sim, D. M.; Kim, M.; Yim, S.; Choi, M.-J.; Choi, J.; Yoo, S.; Jung, Y. S. Controlled Doping of Vacancy-Containing Few-Layer MoS₂ via Highly Stable Thiol-Based Molecular Chemisorption. *ACS Nano* **2015**, *9* (12), 12115–12123. <https://doi.org/10.1021/acsnano.5b05173>.
- (104) Cho, K.; Min, M.; Kim, T.-Y.; Jeong, H.; Pak, J.; Kim, J.-K.; Jang, J.; Yun, S. J.; Lee, Y. H.; Hong, W.-K.; Lee, T. Electrical and Optical Characterization of MoS₂ with Sulfur Vacancy Passivation by Treatment with Alkanethiol Molecules. *ACS Nano* **2015**, *9* (8), 8044–8053. <https://doi.org/10.1021/acsnano.5b04400>.
- (105) Chen, X.; Berner, N. C.; Backes, C.; Duesberg, G. S.; McDonald, A. R. Functionalization of Two-Dimensional MoS₂: On the Reaction Between MoS₂ and Organic Thiols. *Angew. Chem. Int. Ed.* **2016**, *55* (19), 5803–5808. <https://doi.org/10.1002/anie.201510219>.
- (106) Li, Q.; Zhao, Y.; Ling, C.; Yuan, S.; Chen, Q.; Wang, J. Towards a Comprehensive Understanding of the Reaction Mechanisms Between Defective MoS₂ and Thiol Molecules. *Angew. Chem. Int. Ed.* **2017**, *56* (35), 10501–10505. <https://doi.org/10.1002/anie.201706038>.
- (107) Förster, A.; Gemming, S.; Seifert, G.; Tománek, D. Chemical and Electronic Repair Mechanism of Defects in MoS₂ Monolayers. *ACS Nano* **2017**, *11* (10), 9989–9996. <https://doi.org/10.1021/acsnano.7b04162>.
- (108) Förster, A.; Gemming, S.; Seifert, G. Functional Thiols as Repair and Doping Agents of Defective MoS₂ Monolayers. *J. Phys. Condens. Matter* **2018**, *30* (23), 235302. <https://doi.org/10.1088/1361-648X/aac0ad>.
- (109) Gul, A.; Bacaksiz, C.; Unsal, E.; Akbali, B.; Tomak, A.; Zareie, H. M.; Sahin, H. Theoretical and Experimental Investigation of Conjugation of 1,6-Hexanedithiol on MoS₂. *Mater. Res. Express* **2018**, *5* (3), 036415. <https://doi.org/10.1088/2053-1591/aab4a6>.
- (110) Chen, X.; McGlynn, C.; McDonald, A. R. Two-Dimensional MoS₂ Catalyzed Oxidation of Organic Thiols. *Chem. Mater.* **2018**, *30* (20), 6978–6982. <https://doi.org/10.1021/acs.chemmater.8b01454>.
- (111) Cho, K.; Pak, J.; Kim, J.-K.; Kang, K.; Kim, T.-Y.; Shin, J.; Choi, B. Y.; Chung, S.; Lee, T. Contact-Engineered Electrical Properties of MoS₂ Field-Effect Transistors via Selectively Deposited Thiol-Molecules. *Adv. Mater.* **2018**, *30* (18), 1705540. <https://doi.org/10.1002/adma.201705540>.
- (112) Chen, Y.; Huang, S.; Ji, X.; Adepalli, K.; Yin, K.; Ling, X.; Wang, X.; Xue, J.; Dresselhaus, M.; Kong, J.; Yildiz, B. Tuning Electronic Structure of Single

- Layer MoS₂ through Defect and Interface Engineering. *ACS Nano* **2018**, *12* (3), 2569–2579. <https://doi.org/10.1021/acsnano.7b08418>.
- (113) van de Walle, A.; Asta, M.; Ceder, G. The Alloy Theoretic Automated Toolkit: A User Guide. *Calphad* **2002**, *26* (4), 539–553. [https://doi.org/10.1016/S0364-5916\(02\)80006-2](https://doi.org/10.1016/S0364-5916(02)80006-2).
- (114) Zhu, J.; Wang, Z.; Yu, H.; Li, N.; Zhang, J.; Meng, J.; Liao, M.; Zhao, J.; Lu, X.; Du, L.; Yang, R.; Shi, D.; Jiang, Y.; Zhang, G. Argon Plasma Induced Phase Transition in Monolayer MoS₂. *J. Am. Chem. Soc.* **2017**, *139* (30), 10216–10219. <https://doi.org/10.1021/jacs.7b05765>.
- (115) Szychalski, W. L.; Pisarek, M.; Szoszkiewicz, R. Microscale Insight into Oxidation of Single MoS₂ Crystals in Air. *J. Phys. Chem. C* **2017**, *121* (46), 26027–26033. <https://doi.org/10.1021/acs.jpcc.7b05405>.
- (116) Provine, J.; Schindler, P.; Torgersen, J.; Kim, H. J.; Karnthaler, H.-P.; Prinz, F. B. Atomic Layer Deposition by Reaction of Molecular Oxygen with Tetrakisdimethylamido-Metal Precursors. *J. Vac. Sci. Technol. A* **2015**, *34* (1), 01A138. <https://doi.org/10.1116/1.4937991>.
- (117) Xie, Q.; Jiang, Y.-L.; Detavernier, C.; Deduytsche, D.; Van Meirhaeghe, R. L.; Ru, G.-P.; Li, B.-Z.; Qu, X.-P. Atomic Layer Deposition of TiO₂ from Tetrakis-Dimethyl-Amido Titanium or Ti Isopropoxide Precursors and H₂O. *J. Appl. Phys.* **2007**, *102* (8), 083521. <https://doi.org/10.1063/1.2798384>.
- (118) Liu, Y.; Stradins, P.; Wei, S.-H. Air Passivation of Chalcogen Vacancies in Two-Dimensional Semiconductors. *Angew. Chem. Int. Ed.* **2016**, *55* (3), 965–968. <https://doi.org/10.1002/anie.201508828>.
- (119) Li, H.; Huang, M.; Cao, G. Markedly Different Adsorption Behaviors of Gas Molecules on Defective Monolayer MoS₂: A First-Principles Study. *Phys. Chem. Chem. Phys.* **2016**, *18* (22), 15110–15117. <https://doi.org/10.1039/C6CP01362G>.
- (120) Lin, X.; Ni, J. Charge and Magnetic States of Mn-, Fe-, and Co-Doped Monolayer MoS₂. *J. Appl. Phys.* **2014**, *116* (4), 044311. <https://doi.org/10.1063/1.4891495>.
- (121) Wu, M.; Yao, X.; Hao, Y.; Dong, H.; Cheng, Y.; Liu, H.; Lu, F.; Wang, W.; Cho, K.; Wang, W.-H. Electronic Structures, Magnetic Properties and Band Alignments of 3d Transition Metal Atoms Doped Monolayer MoS₂. *Phys. Lett. A* **2018**, *382* (2), 111–115. <https://doi.org/10.1016/j.physleta.2017.10.024>.
- (122) Tongay, S.; Suh, J.; Ataca, C.; Fan, W.; Luce, A.; Kang, J. S.; Liu, J.; Ko, C.; Raghunathan, R.; Zhou, J.; Ogletree, F.; Li, J.; Grossman, J. C.; Wu, J. Defects Activated Photoluminescence in Two-Dimensional Semiconductors: Interplay between Bound, Charged, and Free Excitons. *Sci. Rep.* **2013**, *3*, 2657. <https://doi.org/10.1038/srep02657>.
- (123) Wei, X.; Yu, Z.; Hu, F.; Cheng, Y.; Yu, L.; Wang, X.; Xiao, M.; Wang, J.; Wang, X.; Shi, Y. Mo-O Bond Doping and Related-Defect Assisted Enhancement of Photoluminescence in Monolayer MoS₂. *AIP Adv.* **2014**, *4* (12), 123004. <https://doi.org/10.1063/1.4897522>.

- (124) Liu, H.; Han, N.; Zhao, J. Atomistic Insight into the Oxidation of Monolayer Transition Metal Dichalcogenides: From Structures to Electronic Properties. *RSC Adv.* **2015**, *5* (23), 17572–17581. <https://doi.org/10.1039/C4RA17320A>.
- (125) Qi, L.; Wang, Y.; Shen, L.; Wu, Y. Chemisorption-Induced n-Doping of MoS₂ by Oxygen. *Appl. Phys. Lett.* **2016**, *108* (6), 063103. <https://doi.org/10.1063/1.4941551>.
- (126) Lu, H.; Kummel, A.; Robertson, J. Passivating the Sulfur Vacancy in Monolayer MoS₂. *APL Mater.* **2018**, *6* (6), 066104. <https://doi.org/10.1063/1.5030737>.
- (127) González, C.; Biel, B.; Dappe, Y. J. Adsorption of Small Inorganic Molecules on a Defective MoS₂ Monolayer. *Phys. Chem. Chem. Phys.* **2017**, *19* (14), 9485–9499. <https://doi.org/10.1039/C7CP00544J>.
- (128) Akdim, B.; Pachter, R.; Mou, S. Theoretical Analysis of the Combined Effects of Sulfur Vacancies and Analyte Adsorption on the Electronic Properties of Single-Layer MoS₂. *Nanotechnology* **2016**, *27* (18), 185701. <https://doi.org/10.1088/0957-4484/27/18/185701>.
- (129) Rao, R.; Islam, A. E.; Campbell, P. M.; Vogel, E. M.; Maruyama, B. In Situthermal Oxidation Kinetics in Few Layer MoS₂. *2D Mater.* **2017**, *4* (2), 025058. <https://doi.org/10.1088/2053-1583/aa6532>.
- (130) Huo, N.; Yang, Y.; Wu, Y.-N.; Zhang, X.-G.; Pantelides, S. T.; Konstantatos, G. High Carrier Mobility in Monolayer CVD-Grown MoS₂ through Phonon Suppression. *Nanoscale* **2018**, *10* (31), 15071–15077. <https://doi.org/10.1039/C8NR04416C>.
- (131) Singh, A. K.; Hennig, R. G.; Davydov, A. V.; Tavazza, F. Al₂O₃ as a Suitable Substrate and a Dielectric Layer for N-Layer MoS₂. *Appl. Phys. Lett.* **2015**, *107* (5), 053106. <https://doi.org/10.1063/1.4928179>.
- (132) Kufer, D.; Konstantatos, G. Highly Sensitive, Encapsulated MoS₂ Photodetector with Gate Controllable Gain and Speed. *Nano Lett.* **2015**, *15* (11), 7307–7313. <https://doi.org/10.1021/acs.nanolett.5b02559>.
- (133) Price, K. M.; Najmaei, S.; Ekuma, C. E.; Burke, R. A.; Dubey, M.; Franklin, A. D. Plasma-Enhanced Atomic Layer Deposition of HfO₂ on Monolayer, Bilayer, and Trilayer MoS₂ for the Integration of High-κ Dielectrics in Two-Dimensional Devices. *ACS Appl. Nano Mater.* **2019**, *2* (7), 4085–4094. <https://doi.org/10.1021/acsanm.9b00505>.
- (134) Zhang, J.; Jia, S.; Kholmanov, I.; Dong, L.; Er, D.; Chen, W.; Guo, H.; Jin, Z.; Shenoy, V. B.; Shi, L.; Lou, J. Janus Monolayer Transition-Metal Dichalcogenides. *ACS Nano* **2017**, *11* (8), 8192–8198. <https://doi.org/10.1021/acs.nano.7b03186>.
- (135) Lu, A.-Y.; Zhu, H.; Xiao, J.; Chuu, C.-P.; Han, Y.; Chiu, M.-H.; Cheng, C.-C.; Yang, C.-W.; Wei, K.-H.; Yang, Y.; Wang, Y.; Sokaras, D.; Nordlund, D.; Yang, P.; Muller, D. A.; Chou, M.-Y.; Zhang, X.; Li, L.-J. Janus Monolayers of Transition Metal Dichalcogenides. *Nat. Nanotechnol.* **2017**, *12* (8), 744–749. <https://doi.org/10.1038/nnano.2017.100>.
- (136) Chaurasiya, R.; Dixit, A.; Pandey, R. Strain-Mediated Stability and Electronic Properties of WS₂, Janus WSSe and WSe₂ Monolayers. *Superlattices Microstruct.* **2018**, *122*, 268–279. <https://doi.org/10.1016/j.spmi.2018.07.039>.

- (137) Wang, J.; Shu, H.; Zhao, T.; Liang, P.; Wang, N.; Cao, D.; Chen, X. Intriguing Electronic and Optical Properties of Two-Dimensional Janus Transition Metal Dichalcogenides. *Phys. Chem. Chem. Phys.* **2018**, *20* (27), 18571–18578. <https://doi.org/10.1039/C8CP02612B>.
- (138) Tang, X.; Li, S.; Ma, Y.; Du, A.; Liao, T.; Gu, Y.; Kou, L. Distorted Janus Transition Metal Dichalcogenides: Stable Two-Dimensional Materials with Sizable Band Gap and Ultrahigh Carrier Mobility. *J. Phys. Chem. C* **2018**, *122* (33), 19153–19160. <https://doi.org/10.1021/acs.jpcc.8b04161>.
- (139) Shang, C.; Xu, B.; Lei, X.; Yu, S.; Chen, D.; Wu, M.; Sun, B.; Liu, G.; Ouyang, C. Bandgap Tuning in MoSSe Bilayers: Synergistic Effects of Dipole Moment and Interlayer Distance. *Phys. Chem. Chem. Phys.* **2018**, *20* (32), 20919–20926. <https://doi.org/10.1039/C8CP04208J>.
- (140) Kandemir, A.; Sahin, H. Bilayers of Janus WSSe: Monitoring the Stacking Type via the Vibrational Spectrum. *Phys. Chem. Chem. Phys.* **2018**, *20* (25), 17380–17386. <https://doi.org/10.1039/C8CP02802H>.
- (141) Luo, Y. F.; Pang, Y.; Tang, M.; Song, Q.; Wang, M. Electronic Properties of Janus MoSSe Nanotubes. *Comput. Mater. Sci.* **2019**, *156*, 315–320. <https://doi.org/10.1016/j.commatsci.2018.10.012>.
- (142) Tang, Z.-K.; Wen, B.; Chen, M.; Liu, L.-M. Janus MoSSe Nanotubes: Tunable Band Gap and Excellent Optical Properties for Surface Photocatalysis. *Adv. Theory Simul.* **2018**, *1* (10), 1800082. <https://doi.org/10.1002/adts.201800082>.
- (143) Wu, H.-H.; Meng, Q.; Huang, H.; Liu, C. T.; Wang, X.-L. Tuning the Indirect–Direct Band Gap Transition in the MoS₂-xSex Armchair Nanotube by Diameter Modulation. *Phys. Chem. Chem. Phys.* **2018**, *20* (5), 3608–3613. <https://doi.org/10.1039/C7CP08034D>.
- (144) Jin, H.; Wang, T.; Gong, Z.-R.; Long, C.; Dai, Y. Prediction of an Extremely Long Exciton Lifetime in a Janus-MoSTe Monolayer. *Nanoscale* **2018**, *10* (41), 19310–19315. <https://doi.org/10.1039/C8NR04568B>.
- (145) Ma, X.; Wu, X.; Wang, H.; Wang, Y. A Janus MoSSe Monolayer: A Potential Wide Solar-Spectrum Water-Splitting Photocatalyst with a Low Carrier Recombination Rate. *J. Mater. Chem. A* **2018**, *6* (5), 2295–2301. <https://doi.org/10.1039/C7TA10015A>.
- (146) Son, Y.-W.; Cohen, M. L.; Louie, S. G. Energy Gaps in Graphene Nanoribbons. *Phys. Rev. Lett.* **2006**, *97* (21), 216803. <https://doi.org/10.1103/PhysRevLett.97.216803>.
- (147) Barone, V.; Hod, O.; Scuseria, G. E. Electronic Structure and Stability of Semiconducting Graphene Nanoribbons. *Nano Lett.* **2006**, *6* (12), 2748–2754. <https://doi.org/10.1021/nl0617033>.
- (148) Yang, L.; Park, C.-H.; Son, Y.-W.; Cohen, M. L.; Louie, S. G. Quasiparticle Energies and Band Gaps in Graphene Nanoribbons. *Phys. Rev. Lett.* **2007**, *99* (18), 186801. <https://doi.org/10.1103/PhysRevLett.99.186801>.
- (149) Li, Y.; Zhou, Z.; Zhang, S.; Chen, Z. MoS₂ Nanoribbons: High Stability and Unusual Electronic and Magnetic Properties. *J. Am. Chem. Soc.* **2008**, *130* (49), 16739–16744. <https://doi.org/10.1021/ja805545x>.

- (150) Ataca, C.; Şahin, H.; Aktürk, E.; Ciraci, S. Mechanical and Electronic Properties of MoS₂ Nanoribbons and Their Defects. *J. Phys. Chem. C* **2011**, *115* (10), 3934–3941. <https://doi.org/10.1021/jp1115146>.
- (151) Botello-Méndez, A. R.; López-Urías, F.; Terrones, M.; Terrones, H. Metallic and Ferromagnetic Edges in Molybdenum Disulfide Nanoribbons. *Nanotechnology* **2009**, *20* (32), 325703. <https://doi.org/10.1088/0957-4484/20/32/325703>.
- (152) Pan, H.; Zhang, Y.-W. Edge-Dependent Structural, Electronic and Magnetic Properties of MoS₂ Nanoribbons. *J. Mater. Chem.* **2012**, *22* (15), 7280–7290. <https://doi.org/10.1039/C2JM15906F>.
- (153) Kim, J.; Yun, W. S.; Lee, J. D. Optical Absorption of Armchair MoS₂ Nanoribbons: Enhanced Correlation Effects in the Reduced Dimension. *J. Phys. Chem. C* **2015**, *119* (24), 13901–13906. <https://doi.org/10.1021/acs.jpcc.5b02232>.
- (154) Chen, S.; Kim, S.; Chen, W.; Yuan, J.; Bashir, R.; Lou, J.; van der Zande, A. M.; King, W. P. Monolayer MoS₂ Nanoribbon Transistors Fabricated by Scanning Probe Lithography. *Nano Lett.* **2019**, *19* (3), 2092–2098. <https://doi.org/10.1021/acs.nanolett.9b00271>.
- (155) Yang, S.; Li, D.; Zhang, T.; Tao, Z.; Chen, J. First-Principles Study of Zigzag MoS₂ Nanoribbon As a Promising Cathode Material for Rechargeable Mg Batteries. *J. Phys. Chem. C* **2012**, *116* (1), 1307–1312. <https://doi.org/10.1021/jp2097026>.
- (156) Hong, S.; Yoon, Y.; Guo, J. Metal-Semiconductor Junction of Graphene Nanoribbons. *Appl. Phys. Lett.* **2008**, *92* (8), 083107. <https://doi.org/10.1063/1.2885095>.
- (157) Zhang, J.; Sun, Y.; Zhu, J.; Gao, Z.; Li, S.; Mu, S.; Huang, Y. Ultranarrow Graphene Nanoribbons toward Oxygen Reduction and Evolution Reactions. *Adv. Sci.* **2018**, *5* (12), 1801375. <https://doi.org/10.1002/advs.201801375>.
- (158) Heyd, J.; Scuseria, G. E.; Ernzerhof, M. Hybrid Functionals Based on a Screened Coulomb Potential. *J. Chem. Phys.* **2003**, *118* (18), 8207–8215. <https://doi.org/10.1063/1.1564060>.
- (159) Kou, L.; Tang, C.; Zhang, Y.; Heine, T.; Chen, C.; Frauenheim, T. Tuning Magnetism and Electronic Phase Transitions by Strain and Electric Field in Zigzag MoS₂ Nanoribbons. *J. Phys. Chem. Lett.* **2012**, *3* (20), 2934–2941. <https://doi.org/10.1021/jz301339e>.
- (160) Xiong, Q.; Zhou, J.; Zhang, J.; Kitamura, T.; Li, Z. Spontaneous Curling of Freestanding Janus Monolayer Transition-Metal Dichalcogenides. *Phys. Chem. Chem. Phys.* **2018**, *20* (32), 20988–20995. <https://doi.org/10.1039/C8CP02011F>.
- (161) Zhang, H.; Li, X.-B.; Liu, L.-M. Tunable Electronic and Magnetic Properties of WS₂ Nanoribbons. *J. Appl. Phys.* **2013**, *114* (9), 093710. <https://doi.org/10.1063/1.4820470>.
- (162) Wang, M.; Pang, Y.; Liu, D. Y.; Zheng, S. H.; Song, Q. L. Tuning Magnetism by Strain and External Electric Field in Zigzag Janus MoSSe Nanoribbons. *Comput. Mater. Sci.* **2018**, *146*, 240–247. <https://doi.org/10.1016/j.commatsci.2018.01.044>.

- (163) Wines, D.; Kropp, J. A.; Chaney, G.; Ersan, F.; Ataca, C. Electronic Properties of Bare and Functionalized Two-Dimensional Tellurene Structures. *Phys. Chem. Chem. Phys.* **2020**, *22*, 6727. <https://doi.org/10.1039/D0CP00357C>.
- (164) Zhang, S.; Yan, Z.; Li, Y.; Chen, Z.; Zeng, H. Atomically Thin Arsenene and Antimonene: Semimetal–Semiconductor and Indirect–Direct Band-Gap Transitions. *Angew. Chem. Int. Ed.* **2015**, *54* (10), 3112–3115. <https://doi.org/10.1002/anie.201411246>.
- (165) Ersan, F.; Aktürk, E.; Ciraci, S. Stable Single-Layer Structure of Group-V Elements. *Phys. Rev. B* **2016**, *94* (24), 245417. <https://doi.org/10.1103/PhysRevB.94.245417>.
- (166) Cahangirov, S.; Topsakal, M.; Aktürk, E.; Şahin, H.; Ciraci, S. Two- and One-Dimensional Honeycomb Structures of Silicon and Germanium. *Phys. Rev. Lett.* **2009**, *102* (23), 236804. <https://doi.org/10.1103/PhysRevLett.102.236804>.
- (167) Zhu, Z.; Cai, X.; Yi, S.; Chen, J.; Dai, Y.; Niu, C.; Guo, Z.; Xie, M.; Liu, F.; Cho, J.-H.; Jia, Y.; Zhang, Z. Multivalency-Driven Formation of Te-Based Monolayer Materials: A Combined First-Principles and Experimental Study. *Phys. Rev. Lett.* **2017**, *119* (10), 106101. <https://doi.org/10.1103/PhysRevLett.119.106101>.
- (168) Huang, X.; Guan, J.; Lin, Z.; Liu, B.; Xing, S.; Wang, W.; Guo, J. Epitaxial Growth and Band Structure of Te Film on Graphene. *Nano Lett.* **2017**, *17* (8), 4619–4623. <https://doi.org/10.1021/acs.nanolett.7b01029>.
- (169) Du, Y.; Qiu, G.; Wang, Y.; Si, M.; Xu, X.; Wu, W.; Ye, P. D. One-Dimensional van Der Waals Material Tellurium: Raman Spectroscopy under Strain and Magneto-Transport. *Nano Lett.* **2017**, *17* (6), 3965–3973. <https://doi.org/10.1021/acs.nanolett.7b01717>.
- (170) Wang, Y.; Qiu, G.; Wang, R.; Huang, S.; Wang, Q.; Liu, Y.; Du, Y.; Goddard, W. A.; Kim, M. J.; Xu, X.; Ye, P. D.; Wu, W. Field-Effect Transistors Made from Solution-Grown Two-Dimensional Tellurene. *Nat. Electron.* **2018**, *1* (4), 228–236. <https://doi.org/10.1038/s41928-018-0058-4>.
- (171) Xian, L.; Paz, A. P.; Bianco, E.; Ajayan, P. M.; Rubio, A. Square Selenene and Tellurene: Novel Group VI Elemental 2D Materials with Nontrivial Topological Properties. *2D Mater.* **2017**, *4* (4), 041003. <https://doi.org/10.1088/2053-1583/aa8418>.
- (172) Khatun, S.; Banerjee, A.; Pal, A. J. Nonlayered Tellurene as an Elemental 2D Topological Insulator: Experimental Evidence from Scanning Tunneling Spectroscopy. *Nanoscale* **2019**, *11* (8), 3591–3598. <https://doi.org/10.1039/C8NR09760G>.
- (173) Sharma, S.; Singh, N.; Schwingenschlögl, U. Two-Dimensional Tellurene as Excellent Thermoelectric Material. *ACS Appl. Energy Mater.* **2018**, *1* (5), 1950–1954. <https://doi.org/10.1021/acsaem.8b00032>.
- (174) Qiu, G.; Wang, Y.; Nie, Y.; Zheng, Y.; Cho, K.; Wu, W.; Ye, P. D. Quantum Transport and Band Structure Evolution under High Magnetic Field in Few-Layer Tellurene. *Nano Lett.* **2018**, *18* (9), 5760–5767. <https://doi.org/10.1021/acs.nanolett.8b02368>.

- (175) Amani, M.; Tan, C.; Zhang, G.; Zhao, C.; Bullock, J.; Song, X.; Kim, H.; Shrestha, V. R.; Gao, Y.; Crozier, K. B.; Scott, M.; Javey, A. Solution-Synthesized High-Mobility Tellurium Nanoflakes for Short-Wave Infrared Photodetectors. *ACS Nano* **2018**, *12* (7), 7253–7263. <https://doi.org/10.1021/acsnano.8b03424>.
- (176) Dong, Y.; Zeng, B.; Zhang, X.; Li, D.; He, J.; Long, M. Study on the Strain-Induced Mechanical Property Modulations in Monolayer Tellurene. *J. Appl. Phys.* **2019**, *125* (6), 064304. <https://doi.org/10.1063/1.5079934>.
- (177) Xiang, Y.; Gao, S.; Xu, R.-G.; Wu, W.; Leng, Y. Phase Transition in Two-Dimensional Tellurene under Mechanical Strain Modulation. *Nano Energy* **2019**, *58*, 202–210. <https://doi.org/10.1016/j.nanoen.2019.01.040>.
- (178) Wang, X. H.; Wang, D. W.; Yang, A. J.; Koratkar, N.; Chu, J. F.; Lv, P. L.; Rong, M. Z. Effects of Adatom and Gas Molecule Adsorption on the Physical Properties of Tellurene: A First Principles Investigation. *Phys. Chem. Chem. Phys.* **2018**, *20* (6), 4058–4066. <https://doi.org/10.1039/C7CP07906K>.
- (179) Zhang, S.; Zhou, W.; Ma, Y.; Ji, J.; Cai, B.; Yang, S. A.; Zhu, Z.; Chen, Z.; Zeng, H. Antimonene Oxides: Emerging Tunable Direct Bandgap Semiconductor and Novel Topological Insulator. *Nano Lett.* **2017**, *17* (6), 3434–3440. <https://doi.org/10.1021/acs.nanolett.7b00297>.
- (180) Song, Z.; Liu, C.-C.; Yang, J.; Han, J.; Ye, M.; Fu, B.; Yang, Y.; Niu, Q.; Lu, J.; Yao, Y. Quantum Spin Hall Insulators and Quantum Valley Hall Insulators of BiX/SbX (X=H, F, Cl and Br) Monolayers with a Record Bulk Band Gap. *NPG Asia Mater.* **2014**, *6* (12), e147–e147. <https://doi.org/10.1038/am.2014.113>.
- (181) Li, Y.; Chen, X. Dirac Fermions in Blue-Phosphorus. *2D Mater.* **2014**, *1* (3), 031002. <https://doi.org/10.1088/2053-1583/1/3/031002>.
- (182) Wang, Y.; Ji, W.; Zhang, C.; Li, P.; Li, F.; Ren, M.; Chen, X.-L.; Yuan, M.; Wang, P. Controllable Band Structure and Topological Phase Transition in Two-Dimensional Hydrogenated Arsenene. *Sci. Rep.* **2016**, *6* (1), 1–8. <https://doi.org/10.1038/srep20342>.
- (183) Boukhalov, D. W.; Rudenko, A. N.; Prishchenko, D. A.; Mazurenko, V. G.; Katsnelson, M. I. Chemical Modifications and Stability of Phosphorene with Impurities: A First Principles Study. *Phys. Chem. Chem. Phys.* **2015**, *17* (23), 15209–15217. <https://doi.org/10.1039/C5CP01901J>.
- (184) Liu, M.-Y.; Li, Z.-Y.; Chen, Q.-Y.; Huang, Y.; Cao, C.; He, Y. Emerging Novel Electronic Structure in Hydrogen-Arsenene-Halogen Nanosheets: A Computational Study. *Sci. Rep.* **2017**, *7* (1), 1–9. <https://doi.org/10.1038/s41598-017-05233-z>.
- (185) Zhou, S.; Liu, C.-C.; Zhao, J.; Yao, Y. Monolayer Group-III Monochalcogenides by Oxygen Functionalization: A Promising Class of Two-Dimensional Topological Insulators. *Npj Quantum Mater.* **2018**, *3* (1), 1–7. <https://doi.org/10.1038/s41535-018-0089-0>.
- (186) Grimme, S. Semiempirical GGA-type density functional constructed with a long-range dispersion correction. *J. Comput. Chem.* **2006**, *27* (15), 1787–1799. <https://doi.org/10.1002/jcc.20495>.

- (187) Togo, A.; Tanaka, I. First Principles Phonon Calculations in Materials Science. *Scr. Mater.* **2015**, *108*, 1–5.
<https://doi.org/10.1016/j.scriptamat.2015.07.021>.
- (188) Bader, R. F. W. Atoms in Molecules. *Acc. Chem. Res.* **1985**, *18* (1), 9–15.
<https://doi.org/10.1021/ar00109a003>.
- (189) Henkelman, G.; Arnaldsson, A.; Jónsson, H. A Fast and Robust Algorithm for Bader Decomposition of Charge Density. *Comput. Mater. Sci.* **2006**, *36* (3), 354–360. <https://doi.org/10.1016/j.commatsci.2005.04.010>.
- (190) Momma, K.; Izumi, F. VESTA 3 for Three-Dimensional Visualization of Crystal, Volumetric and Morphology Data. *J. Appl. Crystallogr.* **2011**, *44* (6), 1272–1276. <https://doi.org/10.1107/S0021889811038970>.
- (191) Cheung, C.-H.; Fuh, H.-R.; Hsu, M.-C.; Lin, Y.-C.; Chang, C.-R. Spin Orbit Coupling Gap and Indirect Gap in Strain-Tuned Topological Insulator-Antimonene. *Nanoscale Res. Lett.* **2016**, *11* (1), 459.
<https://doi.org/10.1186/s11671-016-1666-4>.
- (192) Chen, Y.; Liu, J.; Yu, J.; Guo, Y.; Sun, Q. Symmetry-Breaking Induced Large Piezoelectricity in Janus Tellurene Materials. *Phys. Chem. Chem. Phys.* **2019**, *21* (3), 1207–1216. <https://doi.org/10.1039/C8CP04669G>.
- (193) Sang, D. K.; Wen, B.; Gao, S.; Zeng, Y.; Meng, F.; Guo, Z.; Zhang, H. Electronic and Optical Properties of Two-Dimensional Tellurene: From First-Principles Calculations. *Nanomaterials* **2019**, *9* (8), 1075.
<https://doi.org/10.3390/nano9081075>.
- (194) Lin, C.; Cheng, W.; Chai, G.; Zhang, H. Thermoelectric Properties of Two-Dimensional Selenene and Tellurene from Group-VI Elements. *Phys. Chem. Chem. Phys.* **2018**, *20* (37), 24250–24256.
<https://doi.org/10.1039/C8CP04069A>.
- (195) Yi, S.; Zhu, Z.; Cai, X.; Jia, Y.; Cho, J.-H. The Nature of Bonding in Bulk Tellurium Composed of One-Dimensional Helical Chains. *Inorg. Chem.* **2018**, *57* (9), 5083–5088. <https://doi.org/10.1021/acs.inorgchem.7b03244>.
- (196) Malyi, O. I.; Sopiha, K. V.; Persson, C. Energy, Phonon, and Dynamic Stability Criteria of Two-Dimensional Materials. *ACS Appl. Mater. Interfaces* **2019**, *11* (28), 24876–24884. <https://doi.org/10.1021/acsami.9b01261>.
- (197) Yan, J.; Zhang, X.; Pan, Y.; Li, J.; Shi, B.; Liu, S.; Yang, J.; Song, Z.; Zhang, H.; Ye, M.; Quhe, R.; Wang, Y.; Yang, J.; Pan, F.; Lu, J. Monolayer Tellurene–Metal Contacts. *J. Mater. Chem. C* **2018**, *6* (23), 6153–6163.
<https://doi.org/10.1039/C8TC01421C>.
- (198) Yang, S.; Chen, B.; Qin, Y.; Zhou, Y.; Liu, L.; Durso, M.; Zhuang, H.; Shen, Y.; Tongay, S. Highly Crystalline Synthesis of Tellurene Sheets on Two-Dimensional Surfaces: Control over Helical Chain Direction of Tellurene. *Phys. Rev. Mater.* **2018**, *2* (10), 104002.
<https://doi.org/10.1103/PhysRevMaterials.2.104002>.
- (199) Paulauskas, T.; Sen, F. G.; Sun, C.; Longo, P.; Zhang, Y.; Hla, S. W.; Chan, M. K. Y.; Kim, M. J.; Klie, R. F. Stabilization of a Monolayer Tellurene Phase at CdTe Interfaces. *Nanoscale* **2019**, *11* (31), 14698–14706.
<https://doi.org/10.1039/C9NR02342A>.

